AD_____

Award Number: DAMD17-96-1-6187

TITLE: High Resolution and Sensitivity Digital X-Ray Imager for Mammography

PRINCIPAL INVESTIGATOR: Darold Wobschall, Ph.D.

CONTRACTING ORGANIZATION: Sensor Plus, Incorporated
Amherst, New York 14226

REPORT DATE: August 2000

TYPE OF REPORT: Final

PREPARED FOR: US Army Medical Research & Materiel Command
Fort Detrick, Maryland 21702-5012

20010122 116

REPORT DOCUMENTATION PAGE		Form Approved OMB No. 074-0188

Public reporting burden for this collection of information is estimated to average 1 hour per response, including the time for reviewing instructions, searching existing data sources, gathering and maintaining the data needed, and completing and reviewing this collection of information. Send comments regarding this burden estimate or any other aspect of this collection of information, including suggestions for reducing this burden to Washington Headquarters Services, Directorate for Information Operations and Reports, 1215 Jefferson Davis Highway, Suite 1204, Arlington, VA 22202-4302, and to the Office of Management and Budget, Paperwork Reduction Project (0704-0188), Washington, DC 20503

1. AGENCY USE ONLY (Leave blank)	2. REPORT DATE August 2000	3. REPORT TYPE AND DATES COVERED Final (1 Jul 96 - 30 Jun 00)	
4. TITLE AND SUBTITLE High Resolution and Sensitivity Digital X-Ray Imager for Mammography			5. FUNDING NUMBERS DAMD17-96-1-6187
6. AUTHOR(S) Darold Wobschall, Ph.D.			
7. PERFORMING ORGANIZATION NAME(S) AND ADDRESS(ES) Sensor Plus, Incorporated Amherst, New York 14226 E-MAIL: designer@eesensors.com			8. PERFORMING ORGANIZATION REPORT NUMBER
9. SPONSORING / MONITORING AGENCY NAME(S) AND ADDRESS(ES) U.S. Army Medical Research and Materiel Command Fort Detrick, Maryland 21702-5012			10. SPONSORING / MONITORING AGENCY REPORT NUMBER

11. SUPPLEMENTARY NOTES

12a. DISTRIBUTION / AVAILABILITY STATEMENT Approved for public release; distribution unlimited	12b. DISTRIBUTION CODE

13. ABSTRACT (Maximum 200 Words)
A digital x-ray imager with full-field screen and high resolution (40 um) was developed. By using commercial, off-the-shelf components to the maximum extent, the production cost of the imager was minimized. A 3x3 array of lens/optical detector modules was fabricated and tested. It is one of the four quarters which make up the full size imager. CMOS detectors were adapted to this purpose and found to have sufficiently low noise. Electronics, including analog, a/d, DSP, and IEEE1394 drivers were developed and tested.
Software was developed to allow reconstruction of the full image (5400x3900 pixel) from the segments. Distortion correction and image segment stitching utilized a calibration pattern.
Development of the x-ray light valve continued.
A resolution of 10 lp/mm was demonstrated on x-ray images.

14. SUBJECT TERMS Mammography, x-ray, digital, high-resolution, mosaic, CMOS detector			15. NUMBER OF PAGES 97
			16. PRICE CODE
17. SECURITY CLASSIFICATION OF REPORT Unclassified	18. SECURITY CLASSIFICATION OF THIS PAGE Unclassified	19. SECURITY CLASSIFICATION OF ABSTRACT Unclassified	20. LIMITATION OF ABSTRACT Unlimited

NSN 7540-01-280-5500

Standard Form 298 (Rev. 2-89)
Prescribed by ANSI Std. Z39-18
298-102

FOREWORD

Opinions, interpretations, conclusions and recommendations are those of the author and are not necessarily endorsed by the U.S. Army.

✓ Where copyrighted material is quoted, permission has been obtained to use such material.

✓ Where material from documents designated for limited distribution is quoted, permission has been obtained to use the material.

✓ Citations of commercial organizations and trade names in this report do not constitute an official Department of Army endorsement or approval of the products or services of these organizations.

N/A In conducting research using animals, the investigator(s) adhered to the "Guide for the Care and Use of Laboratory Animals," prepared by the Committee on Care and use of Laboratory Animals of the Institute of Laboratory Resources, national Research Council (NIH Publication No. 86-23, Revised 1985).

N/A For the protection of human subjects, the investigator(s) adhered to policies of applicable Federal Law 45 CFR 46.

N/A In conducting research utilizing recombinant DNA technology, the investigator(s) adhered to current guidelines promulgated by the National Institutes of Health.

N/A In the conduct of research utilizing recombinant DNA, the investigator(s) adhered to the NIH Guidelines for Research Involving Recombinant DNA Molecules.

N/A In the conduct of research involving hazardous organisms, the investigator(s) adhered to the CDC-NIH Guide for Biosafety in Microbiological and Biomedical Laboratories.
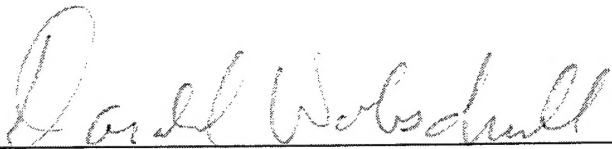
_____ 7/21/00

PI - Signature   Date

3

TABLE OF CONTENTS

INTRODUCTION

The aim of this project is to develop a low-cost, full-size digital x-ray imager for mammography, which is comparable to film/screen in quality (spacial resolution, contrast, and sensitivity). Advantages of digital imaging (ease of storage, transmission to distant locations, image enhancement, and computer-aided diagnosis) are widely recognized.

Our mosaic approach is to break the image into segments or tiles which are individually imaged by lenses onto relatively small CCDs and then to combine the small images, by software, into the larger full size image (8"x10"). Except for the preliminary development of the XLV screen described below, this project is basically an engineering development which optimizes both performance and low production cost.

Many experts expect that eventually flat panel imagers (e.g. thin film transistors) will be the technology of choice. However it seems likely that the production costs of flat panel imagers will be very high for some years, as indicated by the projected prices of full-scale imagers which are being introduced by several major medical imaging companies. Rather than aim our imager development solely at better performance (e.g. higher resolution or sensitivity) than competitive commercial imagers, we have concluded that a good use of the grant resources is to develop a moderate performance, but much lower cost, digital imager to serve groups or markets which would not otherwise be able to afford a digital imager. The introduction of new, lower cost CMOS detectors and other electronic devices have made this plan practical. Accordingly we have redesigned, and have fabricating the data acquisition electronics with the new cost/performance criteria. Our aim is to design a functional, pre-production, full-size digital imager.

As the project progressed a decision was made to focus on the low cost market and to base the first generation design on the CMOS (rather than CCD) sensors. One reason was the successful efforts of the first-tier medical imaging companies to enter the digital mammography market with high performance, (but high cost) imagers. Another is the continuous technical improvements of commercially available CMOS sensors, which now equal the performance of the more expensive CCD sensors.

We had planned a second-generation imager which would use an x-ray light value (XLV). If the XLV could be successfully developed and manufactured at a low-cost, it would improve mammographic sensitivity (DQE), which could aid in the acceptance of the low cost imager.

5

BODY

Significance

The benefits relative to the risks of x-ray mammography for the detection of breast cancer has been thoroughly documented. For each 1% increase in mammographic use in the USA, 10000 to 30,000 malignant breast tumors would be detected and corresponding number of lives saved. Barriers to increase in mammogram uses are:

- Cost and Convenience. A decrease in cost and increase in convenience would attract more women to screening programs.

- Deficiencies in Image Quality and Interpretation. Image enhancements by digital methods would decrease false negative and positive rates.

- Radiation risk. A reduction in the x-ray dose per mammogram would improve the risk-benefit ratio and allow more frequent tests or testing at earlier ages.

Digital x-ray images as a replacement for film are widely regarded as having excellent potential for reducing these barriers as evidenced by extensive research, development and commercial efforts underway. While regarded as the technology of the future, x-ray digital imagers do not fully live up to this potential because, while they offer excellent performance, they are costly.

By using a mosaic-image, respectively with the possible addition of crystal light valve technologies, a digital x-ray imager. A low-cost digital x-ray imager with acceptable performance can be produced. The cost of the imager itself, including computer, is much higher than film, the system cost (cost per mammogram) is expected to be less when staff time and image storage/retrieval/transmission factors are taken into account. There we believe that we can achieve:

Advantages of digital x-ray technology are:
- Rapid, reproducible image acquisition
- Computer Aided Diagnosis (or Analysis)
- Teleradiography
- Image Enhancement Options
- Convenient Archiving

Specific targets for a low-cost digital imager for mammography are:
- Rural Hospitals
  Trained personnel for taking high quality mammogram and experienced radiologist for reading them are not likely to be available
- Developing Countries
  The cost of a standard digital imager is too high, as well as the lack of experienced personnel.

6

Specific Aims

The general aim of this project was to develop a low-cost, full-size x-ray imager for mammography which is comparable to film/screen in quality (special resolution, contrast, and sensitivity). Advantages of digital imaging (ease of storage, ease of transmission to distance locations, image enhancement capabilities, and computer-aided diagnosis) are widely recognized.

Specific aims are given by the following statement of work:
    Design and fabricate a mammographic imager with the following charteristics:

- Active area of 8x10 inchs
- Pixel size of 50 microns or less
- Dynamic range of 12-bits
- Border on one side under 3mm
- Workstation with capacity of 500x5000 pixel display (internal resolution)
- Operation on standard mammographic x-ray sources

Task Schedule

The final task schedule follows:

Task 1. Build Prototype (low resolution)
Design, build and test a single segment of the imager.
        This was done in the first year.

Task 2. System Design
The complete system was designed in the first year, redesigned in the second, and further modified in the third.

Task 3A,B..   Fabricate and Evaluate Small Area, XLV Prototype
    Fabricate Hi-Resolution X-ray Light Valve (XLV)
    An improved XLV will be made by Kent State with the help of new facilities at Sunnybrook. It will have a resolution over 15 lp/mm in an area of 80x80 mm or larger.
        The high resolution XLV will be characterized by Sunnybrook..
These subtasks were not completed but prototypes of portions were made and tested

Task 3C.
        Fabricate Optical System
        Fabricate and Test Electronics Section
        Fabrication and Test of Workstation Interface
All these tasks were completed.

7

Task 4.Fabricate and Test Full Size Imager
A. Fabricate Full Size, CCD Array and Circuit Boards
B. Fabricate and Test Electronics Section
C. Refinement of Image Processing Software
All these tasks were completed.

Task 5.System Performance Test
A.   Test of Imager
The imager will be tested at SUNY (ECMC) using phantoms, and also specimens from Roswell Park Cancer Institute (RPCI) if appropriate. In addition to resolution and noise, image distortion and discontinuities between segments will be examined. Not completed.

B.   Comparison with Film/screen
Standard x-ray film/screens images will be compared (at ECMC) with those obtained by the imager under development. Not done.

C.   Clinical Trial Planning
Planning for future clinical trials will be made primarily by SUNY (ECMC) and the consultants. Not done.

Task 6.Preparation, Radiographic Workstation Software
A.   Implementation of Standard Viewing Software
       Most of this subtask was done.

B.   Verification of Image Quality Robustness
Tests will be made at SUNY (ECMC) to verify that the image quality is not effected by improper software sequences. Not done.

C.   Image Compression
A method of image compression and storage will be selected and implemented at InfiMed. Not done.

D.   Display Tests
The quality of the display will be evaluated at InfiMed, SUNY (ECMC and RPCI). Not done.

Accomplishments (by Task)

Task 1 Build Prototype (low resolution)

Task 1 was a preliminary task done during the first year. It consisted of one, then several, sections of the array constructed with off-the shelf lenses, Kodak CCDs, custom a/d electronics for the acquisition/transfer of the image to a PC where signal processing and analysis was done. The prototype worked satisfactorily but since it was superceed by prototypes designed and constructed in subsequent tasks, it will not be described here.

Task 2 System Design

The basic design was completed before the end of the second year. The design process actually consisted of designing, fabricating, testing several prototypes, with successive improvements. In the early stages CCD image detectors were used but in later stages these were replaced by CMOS detectors. Only the final design is described here and the intermediate stages omitted.

A. Imager Hardware

General

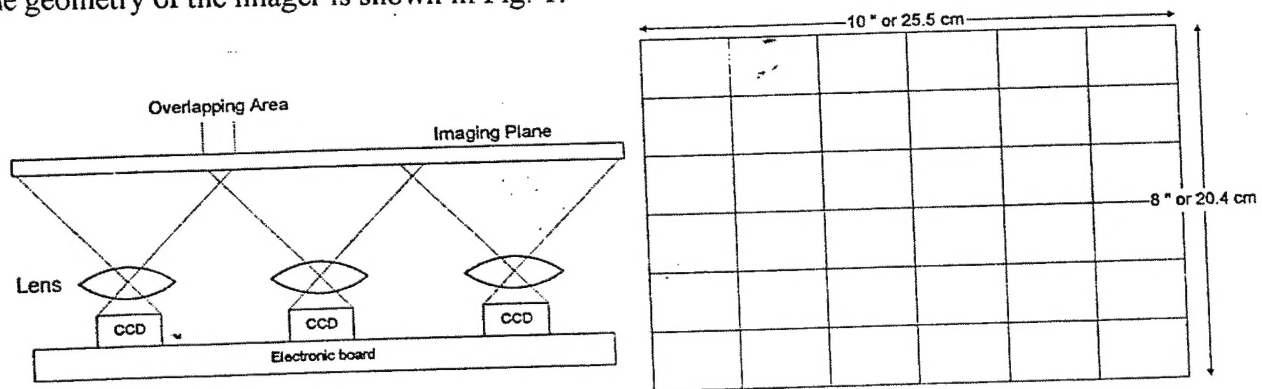The geometry of the imager is shown in Fig. 1.

Fig. 1 Geometry of Low-Cost X-ray Imager for Mammography

This interface used a bi-directional PC printer port interface. Logic circuits, buffers and resistors convert logic control levels driven from the printer port into DSP commmport control signals. Signals driven from the DSP are converted into status signals, which can be polled in software by the PC. In addition, the PC printer port provides the byte-wide data path into and out of the PC.

With this printer port application, one can use this I/O interface for host-data communication, boot loading (code), and debug operations. With proper buffering and software control, it is also possible to build long and reliable links. The speed is primarily dependent on the speed of the host. When using a PC as the host, the speed is limited by the PC I/O channel speed.

DSP and Memory

Digital x-ray mammography imager acquires image data by 18 MHz clock. In order not to miss any pixel data, DSP should read and save it faster than acquiring speed. Static RAM is fast enough but cost is too high for a large memory system. Conventional Dynamic RAM is cheap but access time is not appropriate to our system. DSP will use synchronized dynamic random access memory (SDRAM) for system main memory. Functionally, an SDRAM resembles a conventional DRAM. It is dynamic and must be refreshed. However, the SDRAM architecture has improvements over standard DRAMs such as internal pipe-lining to improve throughput and on-chip interleaving to eliminate gaps in output data. The addition of a clock signal allows fully synchronous operation with the system clock which is 30 MHz in our x-ray imager. This SDRAM enables image data acquiring successful without losing any pixel. Figure 1 shows block diagram for DSP and SDRAM.
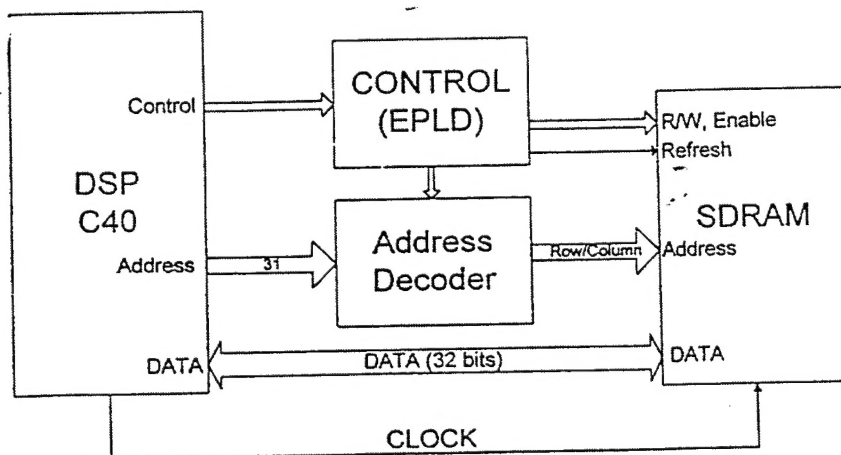
Figure 2. Block diagram for DSP and SDRAM

Mammography Machine Interface Circuitry

To synchronize the X-ray exposure with the image capturing time, an interface circuit is being be developed. Signals originating at the bucky plate of an existing ECMC mammography machine is used for this synchronization. The bucky begins movement before the X-rays begin and will therefore signal the imager electronics to get ready to capture an image. An X-ray detector will also be used to signal the imager to capture an image when the X-rays are on.

10

The mammographic unit was tested at SUNY/Buffalo for testing of the new imager. The most easily accessible were those leads controlling the Bucky grid assembly. We tested and recorded using a storage oscilloscope the electrical outputs available from the Contour unit and found the temporal relationship between those from pins #3 and #9 of the Bucky connector and the measured times of radiation emission from the unit. We tested the temporal relationship for all modes of radiography, i.e. various mA settings for both the large and small grid operation. We found consistent and reproducible relationships based upon which can be designed trigger pulses for clearing and beginning the CCD readout after termination of x-ray exposure. For pin #3 the x-rays are initiated 40 ms for the small grid and 25 ms for the large grid after the beginning of the rise of the signals at this pin. For pin #9 the delay is longer: 375 ms to 420 ms depending on the specific parameters set. Synchronization will be crucial to reduce dark current, fading, drift, and noise.

B. Image Reconstruction

Reconstruction Algorithms for imager

The image quality of a digital mosaic imager relies upon schemes for distortion correction and stitching. The distortion correction is critical to obtain a high quality of image. Several schemes were developed for distortion correction.

Correction schemes for image distortion

Several approaches have been developed to correct distortions introduced by optical components of an imaging system. All the approaches are based on the use of a calibration pattern containing fiducial markers. The schemes we have developed include piece-wise linear interpolation, bilinear interpolation, bicubic spline interpolation, Bezier composite surface interpolation, bicubic B-spline surface interpolation, and polynomial modeling approach. All schemes are based on the relation of corresponding control points between the reference image and the acquired image of a calibration pattern. It should be noted that the bilinear interpolation, bicubic spline interpolation, and polynomial modeling approach are global correction schemes, while the piece-wise linear interpolation, Bezier composite surface interpolation, bicubic B-spline surface interpolation are local correction ones. Note that to reconstruct a full image without losses of detailed information such as micro-calcifications, it is desirable to employ a localized scheme. A comparison between a localized scheme and global schemes will be presented in the evaluation section. To calculate the correction coefficients, we have developed a new calibration pattern shown in Figure 3 which is acquired using a prototype 2x2 imager. The intersections of grid are used as control points. We have developed this calibration pattern by assuming that the distortion in an acquired image will be dominated in the edge area. Figure 4 shows a stitched image with distortion correction using cubic spline surface interpolation.

Stitching Technique

Stitching is based on the extracted information from a calibration pattern. The basic idea is that it uses the extracted information from a calibration pattern as an initial estimation for stitching

information which it is fairly accurate in the range of one pixel. However, this accuracy is variable depending on the detection accuracy of control points. Using the initially estimated information, it adopts one additional step such as cross-correlation, to find the most accurate location for stitching. Test results for this technique are described in Task 4.
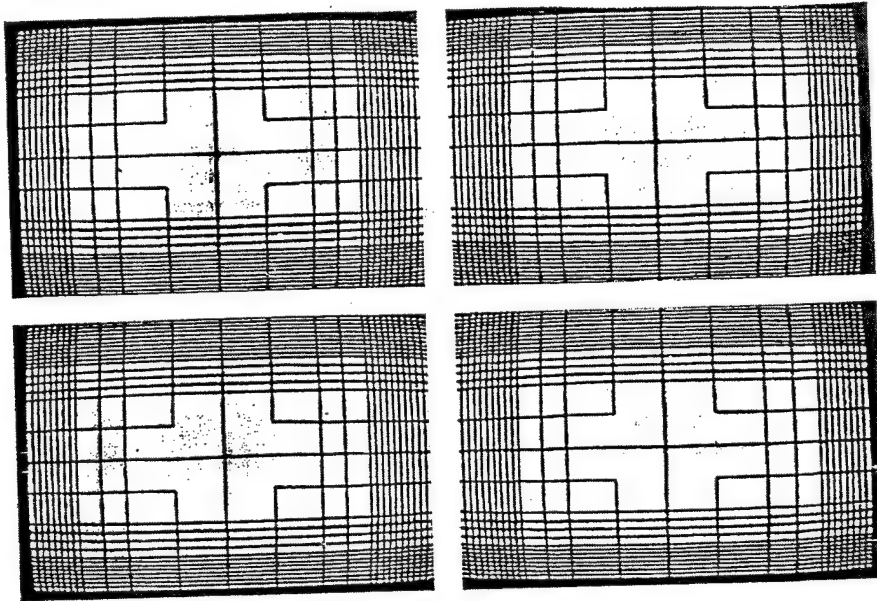
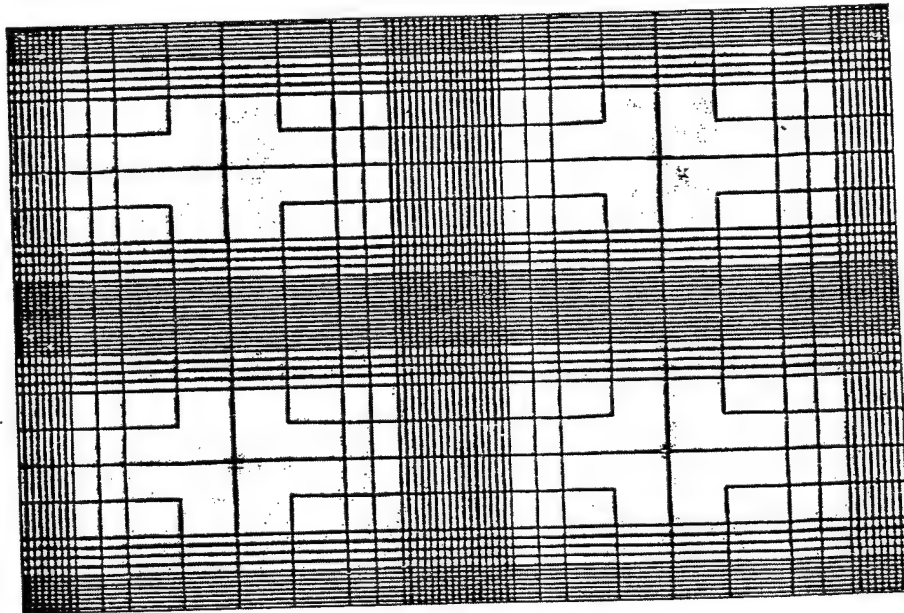Figure 3. Images of the calibration pattern as acquired by each CCD sensor.

Figure 4. Mosaic image reconstructed using the spline interpolation algorithm.

Resolution Consierations

The input pixel size is 42 µm. By comparison, the GE mammographic digital imager is 100 µm. Studies of the effect of pixel size on the interpretation of mammograms indicate that 100 µm is adequate for screening and detection of microcalcifications but 50 µm (or maybe smaller) may be needed diagnosis for (shape determination). We consider this resolution adequate for mammography and perhaps better than expected for a low cost imager. It should be noted that cost minimization, while maintaining adequate performance, requires the consideration of multiple, partly conflicting factors such as array size lens/CCD costs, and signal acquisition complexity/costs. A number of designs were considered before deciding upon the one described here.

To reduce production costs, a single DSP processes the signal from a set of 9 imagers. A block diagram is shown in Fig. 5. Data could instead have been transmitted via the printer port to the main computer (Pentium PC) for most of the image correction and reconstruction. Further information is given in the Task 4 description. The main disadvantage is that the process would be much slower.

Like the Trex imager, one drawback to the imager we are developing is size. It is thicker (4-6") than some other digital imagers which are generally closer to a film/screen cassette in size. There is room underneath (opposite the x-ray source) in standard mammographic x-ray machine for the imager, with modest modifications.
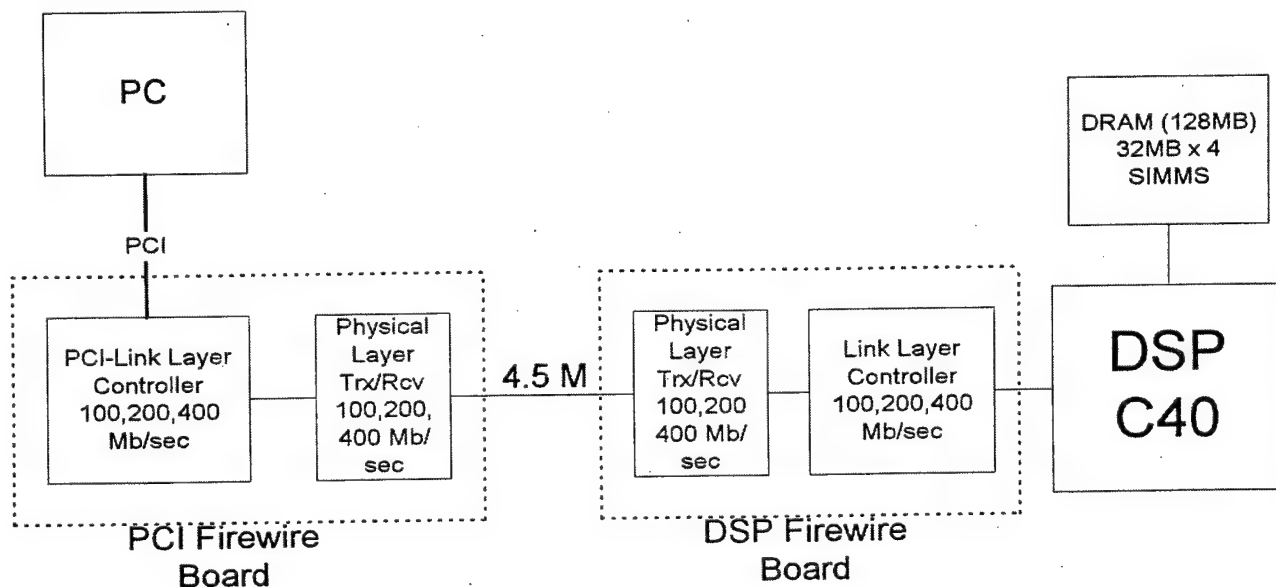

Figure 5 The PC and DSP connection through FireWire™

Lens Design and Fabrication

A single lens was custom designed as discussed, previous reports. An additional element was added to this lens to further reduce defocusing at the edges of the images. Although this lens proves to achieve the desired imaging constraints, the cost is very high ($890/lens for 8 lenses). If these lenses will be used in the final imager, even though the cost exceeds that of the CMOS detector and analog electronics costs combined.

The light collection efficiency of the lens is an important fact in determining the image quality, specifically the image background noise. A drawback of lens coupling in several is that the light transfer from the x-ray conversion screen has a relatively poor efficiency. The two main factors which increase efficiency are (1) use of a small demagnification (we have chosen 4.4) and (2) use of a fast, low f# lens (e.g. 1.1). A small demagnification is important. As discussed in previous reports, the mosaic approach allows a relatively small demagnification per lens. Once the array size is chosen (6x6), the input screen size is established (8"x10"), and the imaging sensor size (8.4x10mm) is selected, then the demagnification (4.4) is fixed.

The other factor is the lens f#. A large aperture with short focal length, that is a low f-number lens combined with a wide angular field of view is desired. However it is difficult to make a lens with a low f# which still provides high resolution over the full field. The image at the sensor must have a resolution of better than 8µm even at the edges. Also it must be physically small so that the lens can be placed close together. No satisfactory commercial lens was found, even after an extensive search. The closest available lens was a f1.3, 1-inch format CCTV type, but it could not focus over the full field unless stopped down excessively (and it was too large). Thus custom design was necessary.

Sensitivity and Resolution Requirements

To meet our goals that the digital imager have an image quality at least as good as film, it is necessary that both the resolution and sensitivity be sufficiently high. Studies of resolution requirements indicate that a resolution of 50µm (10 lp/mm) is desirable but that diagnostic accuracy is not effected if the resolution is reduced to 100µm or 150µm (the GE mammographic digital imager is 100µm). The x-ray resolution tests described above indicate that the resolution of our images approximately 10lp/mm, which is consistent with the 43µm screen pixel size. This easily meets our goal but we plan further, more quantitative, tests (modulation transfer function) with the new lens to verify the results.

Sensitivity for our generation I imager is more of a concern. Lens coupling of the light is inefficient (only 1.5% with the high performance lens). Since we estimate the red conversion screen to produce about 1000 light photons per x-ray photon, there will be about 15 light photons hitting the CMOS sensor. With the current sensor, the noise level is somewhat higher than the signal (from one x-ray phantom), a sub-optional condition. With the improved sensors, available this fall, we expect that the signal will be slightly higher than the noise, which is just adequate.

Imager noise is expressed quantitatively by the detective quantum efficiency (DQE). The DQE of film is about 0.5 (low spacial frequencies) and the best digital imagers are about 0.7 (1 is maximum).

There is no DQE specification on commercial mammographic equipment, but rather the requirement that specific set of features on a mammographic phantom can be discerned (see Fig. 6) with the radiation dose under a given limit. Preliminary tests indicate that this requirement is met, or close to being met, but much more testing is needed. Film mammograms have a DQE in the range of 0.3 to 0.5 (at 0 lp/mm) while the newest digital imagers are in the range of 0.5 to 0.8. Higher quality, lower noise images can always be obtained by increasing the radiation dose. For many medical applications, such as emergency medicine, the higher dose is acceptable. However it is not acceptable, or at least undesirable, for mammographic screening. This is why the emphasis is placed on high sensitivity.

Task 3 Fabricate Small Screen Prototype
The main part of Task 3, that of the low-cost imager fabrication, is an intermediate step to Task 4 (full size imager). Several intermediate sizes were constructed and tested but they will not be described here since they have no features of interest which are not described in the Task 4 imager.
A auxiliary part of the imager design was to built and test an x-ray light valve (XLV). This was done by Sunnybrook (Toronto). It was originally intended that the XLV be a part of the first prototype. However, it was not developed in time and therefore the low-cost design described in Tasks 4 and 5 were developed. These use commercial, off-the-shelf components except for the circuit boards, lenses, and mechanical (optical) mounts. The XLV was not finished because funding was exhausted, but significant progress was made, as described here.

Several x-ray light valve (XLV) designs have been investigated. The key design parameters are liquid crystal type, which controls the characteristic curve of the XLV, and the illumination method.

Figure 6 shows the cross-section of the first prototype XLV. It was a sandwich structure composed of the following layers from the top down: a glass substrate with a transparent, conductive, Indium Tin Oxide (ITO) coating; a ~ 100-500 µm thick a-Se layer; a 1000-5000 µ thick polyamide (PI) alignment layer; a ~5-15 µm thick LC cell formed by spacers for uniform separation between the substrates and doped nematic LC; and a bottom glass
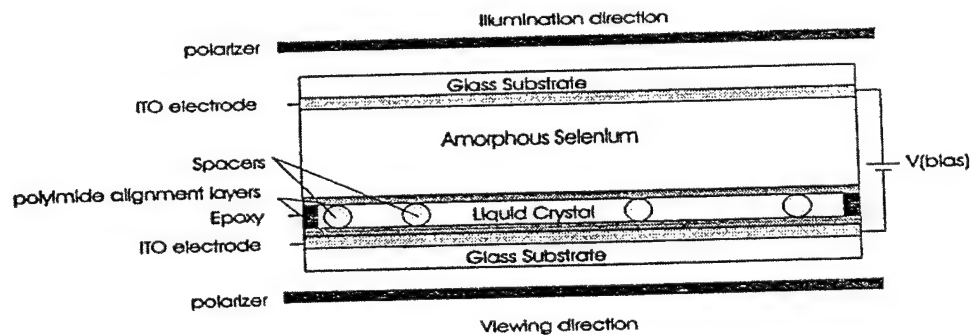
Figure 6 Cross section of twisted nematic x-ray light valve built on a transparent substrate substrate with a conductive ITO coating and PI alignment layer. The two main steps in the manufacturing of the prototype XLV are the a-Se evaporation and the construction of an LC cell.

This approach has demonstrated high resolution images (see for example the line pair phantom showing 9 lp/mm, Figure 7) but does have several problems including fixed pattern noise associated with inadequate production methods. However, this the most fundamental problem is the difficulty in illumination and readout as this approach requires access to both sides, the first side to introduce illumination and the second side to view the complete image.

In order to address this problem we investigate two other methods both of which permit readout and illumination from the same direction. A design for an XLV built on an opaque substrate is shown in Figure 8.
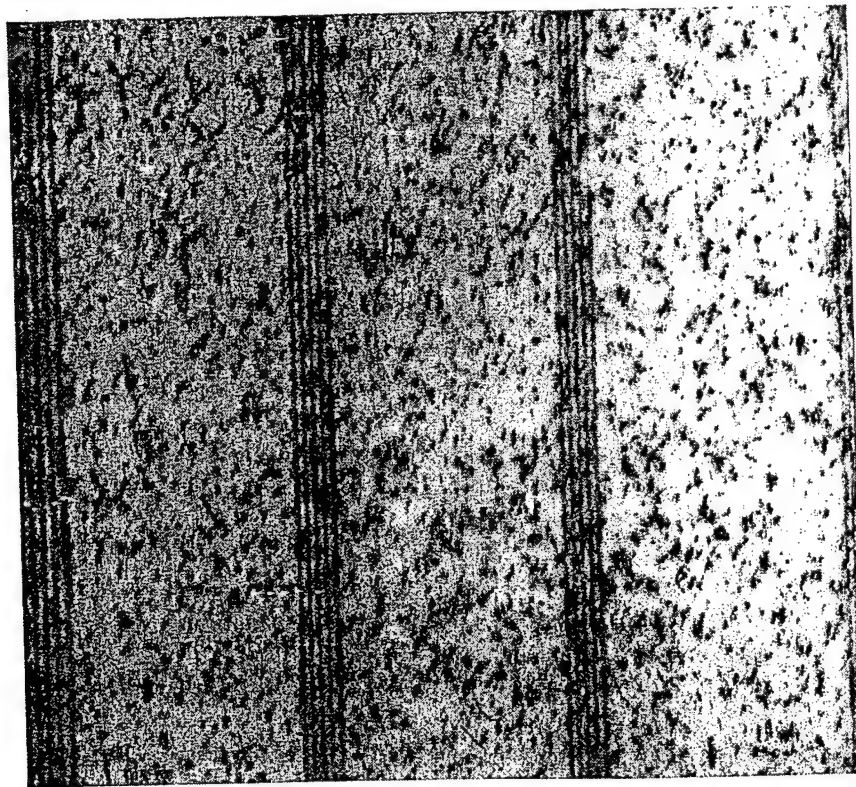
16

Figure 7 Image of lead bar pattern (9 lp/mm on left, 6.3 Ip/mm on right) using a twisted nematic liquid crystal light valve built on a transparent substrate
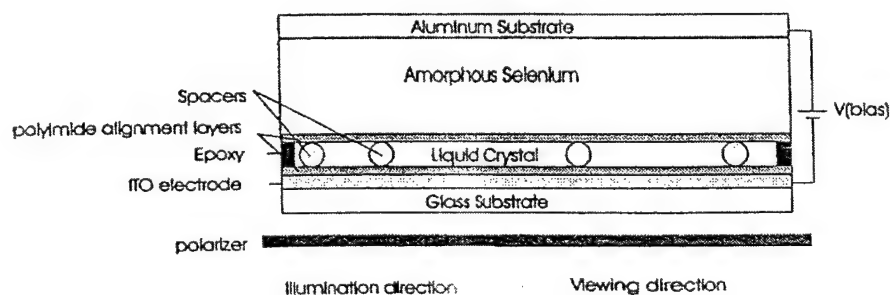

Figure 8 Cross section of aluminum substrate twisted nematic x-ray light valve

Light from the illumination source passes through the polarizer and liquid crystal layer and is reflected by the selenium surface. It is then passed back through the liquid crystal layer and the same polarizer.

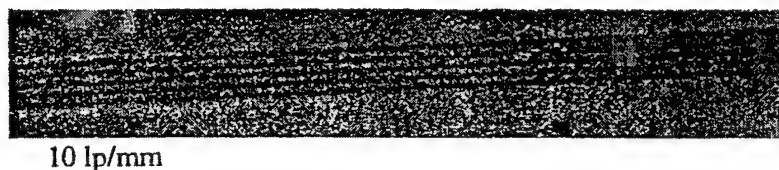Images were created using this procedure and an example is shown in Figure 9.

10 lp/mm

Figure 9 Image obtained using a twisted noematic x-ray light valve with an opaque (aluminum) substrate

Finally, a theoretical investigation of the feasibility of a polymer dispersed x-ray light valve was performed. The potential advantage for this approach is the simplicity of the illumination methods which does not require the use of polarizers and since a mirror surface is not used there is no need to have a high quality diffuse source. There have been several important papers on polymer dispersed optical light valves, although they have not been used as x-ray light valves previously.
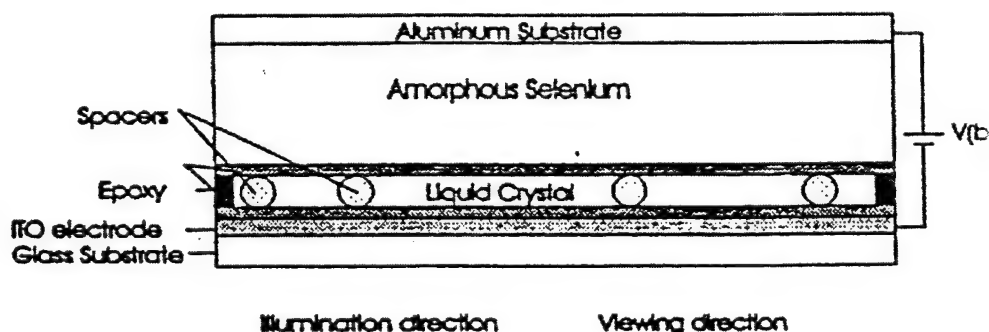

Figure 10 Cross section of polymer dispersed liquid crystal x-ray light valve

The practical implementations of the liquid crystal light valve (XLV) has previously been shown to have visible contrast (see Fig. 11), good resolution (~11 lp/mm), but still had problems associated with limited dynamic range, imperfections in the image and poor sensitivity to radiation. It was found that it could only operate at very small applied potentials (~50-100 V) compared to the design potential of 1500 V, due to the high potential causing the liquid crystal to modulate the readout light prior to exposure.

Figure 11: Image of Finger Phantom

XLV image of a finger phantom at ~100 V bias.

Figure 11 Image of Finger Phantom

Our program was to identify the causes of these problems and propose methods to overcome them. We have previously modeled the operation of the XLV and had checked the proper operating conditions and design parameters of the components. Thus when the device was constructed and did not operate as expected there was obviously some problem, but the cause was unclear. Either the component values had shifted during manufacture or the model was not correct. Once the device is completed then the test procedures we used on components are no longer useful. Instead, system level testing is needed to identify problems.

The major problems related to both image imperfections and inadequate sensitivity were both deemed to be the low operating potential. Thus the problem is to identify the reasons for limiting the bias potential were a primary focus. It was considered that there could be two possible reasons for the need to operate at very low biases, the first was that the dark current had been inadvertently increased in the process of making the XLV and the second was that the resistance of the LC layer was higher than expected. Given that the observed effect seemed to indicate that a potential in excess of prediction was present across the LC layer, the second of the two possibilities seemed the most likely.

Testing this theory involved the development of a tool that would indicate potential division across the layers of the XLV, using the liquid crystal itself as a probe. The operation of the tool utilizes the fact that a cell operated in reflective mode shows a peak in light intensity at some voltage characteristic of the given liquid crystal material, and the intensity rapidly diminishes to low levels after the bias potential is increased past this key value. The test procedure is illustrated in Fig. 12.

Figure 12: XLV Evaluation Arrangement

Light source (laser or white incandescent light with coloured filter) passes through polarizer and reflects off mirror surface of XLV. Reflected light passes through analyzer (optical axis at 90° to polarizer) to the microscope and CCD camera. The blue LEDs are used to clear the image charge and are not illuminated during x-ray exposure and read-out.
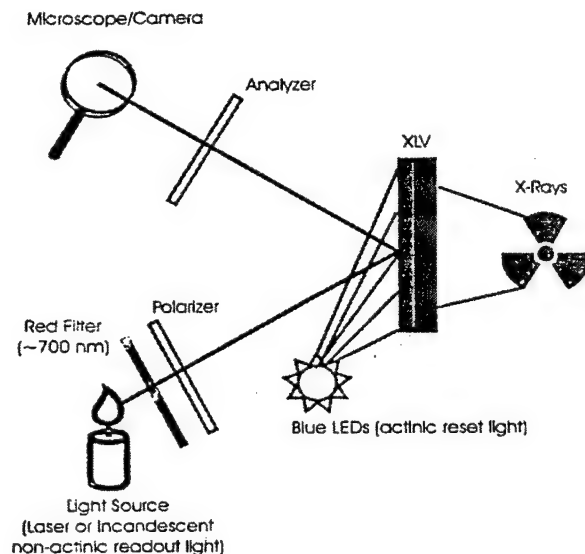
Therefore, by observing the transmission of the XLV over a range of applied voltage values, the transmission intensity peak can be used as an indicator of when the XLV corresponds to this characteristic voltage across the liquid crystal. The image on the front surface of the XLV is viewed by a CCD camera attached to a frame grabber computer system. The XLV itself is connected to a function generator which can produce linear voltage ramps at user defined values of peak voltage value and frequency. The frame grabber acquires data during the application of the ramp, and transmission characteristics can be plotted for individual pixels or small sub-groups of pixels.

Based on these results we propose a solution to our low operating potential problem that should permit high quality images to be produced. It is an approach that eliminates the effect of the biasing field simply by removing the biasing field before readout is attempted. This entails applying a short pulse of high voltage to the XLV, exposing to x-rays while the selenium is properly biased, and then reducing the voltage below the characteristic voltage of the liquid crystal and then capturing the image by reading out the CCD camera. A timing diagram for this approach is shown in Fig. 13.

Figure 13: Schematic of pulsed mode operation

X-rays will be applied during the high voltage (Vstep) pulse, and the image will be at V peak. Blue light clears the image after read-out to prepare XLV for next exposure.

20
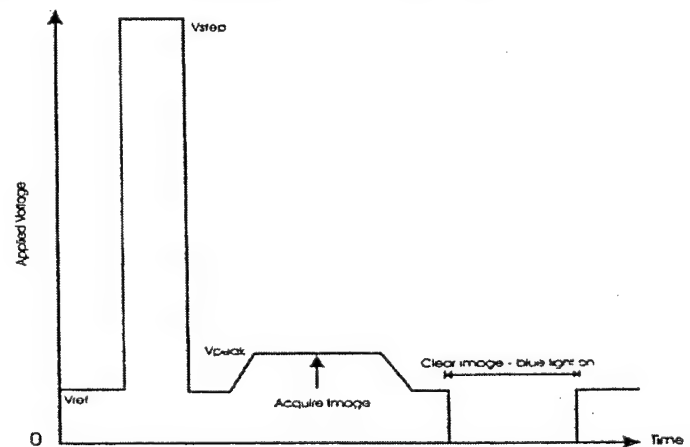
The second major problem was limited dynamic range when operating in the hybrid field mode to permit front side illumination and readout. This was addressed by investigating a novel readout scheme that uses the time at which a given pixel has a maximum intensity. Namely, since the x-ray signal produces an extra bias across the liquid crystal, an exposed area will peak sooner than a shielded area since it will require less applied bias to reach its characteristic voltage. A timing diagram for this approach is illustrated in Fig. 14.

Figure 14: Time-dependent Image Acquisition

Image data is acquired during the ramp to Vpeak. For each pixel in the region of interest over the ramp time the frame number at which intensity is maximal is found and used to construct the image.
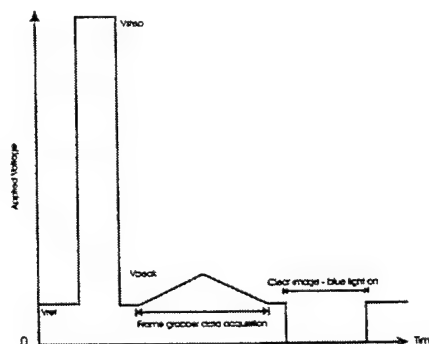
This discovery indicated that an alternate way of obtaining images might be useful. For a given region of interest, obtaining the location in frame numbers of the intensity peak for each pixel to create the image. Since the frame number is a direct correspondence to the time at which that frame was taken and therefore to the applied voltage at that time, the frame number will vary depending on how much signal charge was deposited on the area of the XLV corresponding to that pixel.

This idea was tested using a lead block covering half the region of interest, thereby providing a shielded area and exposed area for comparison. A computer program was written which located the peak value for each pixel and constructed the image. An example of an image obtained using this procedure is shown in Figure 15.

Remaining tasks involve determining the final material parameters (type of liquid crystal material, thickness of liquid crystal layer) of the prototype XLV.

Figure 15: Sample Constructed Image of Edge

The following equalized image (approximate area 0.4 mm^2) was taken using a 650 nm laser as a light source. Blotches in the image are due to the interference pattern made by the laser on the surface.

21

Task 4 Fabricate and Test Full Size Imager

The full size imager was designed so that both the mechanical/optical and electrical sections consisted of four identical parts, or quarter imagers. The four parts can be built and tested separately, then assembled into the full size imager (except for the scintillation screen which is full size). However, due to funding limitations, only a quarter section was actually built and tested.

A. DSP Design and Tests

The electronics block diagram of the 3x3 imager is shown in (Fig. 16). The photographs in Fig. 3B show the 3x3 sensor module and lens mounting plate.

The 3x3 block is a quarter of the full imager. Each block is identical and they are placed next to each other, and fit, to form the full size imager. Each of the 9 image sensor channels contains a CMOS sensor, analog support circuitry, 12-bit A/D converter, and a 16-bit buffer for digital data output. The output buffers are connected to two parallel digital channels, which enter the DSP. The M4 programmable logic devices controls the timing generation and multiplexing of the image data from each sensor. The chosen pixel rate was 1.25MHz for each sensor, requiring the DSP to acquire 25MB/s (2 bytes per pixel, 5 image sensor channels). All the image data was demultiplexed in the DSP and read out through the IEEE1394 interface to the PC for viewing and storage. The reconstruction of the images was done using PC software.

The high-speed DSP circuits with the 128 Mbyte RAM, analog circuits, CMOS timing circuits, were redesigned (custom designed) for this imager. Because of the large amount of data handling capacity and the low noise requirement, this was a difficult and time-consuming task. The result, however, was high quality (production quality) printed circuit boards.

Along with the board development was the migration of software previously done on the PC to processing on the DSP. Now the image processing, as well as the image acquisition, is done on the DSP.

A single CMOS sensor imager was also constructed and used for all the tests shown in Fig. 1 and to obtain x-ray images to test feasibility. The photograph on Fig. 3A shows this imager: Note a reflective mirror was used along with the imager electronics mounted with the lens horizontal to the object plane. This was done to create a thinner imager case and to test the concept for possible use in a production version. The x-ray scintillating screen was placed on the top of the imager case with the lens focused at the object plane.

Firewire ™ Serial Bus

The PC and DSP connection through IEEE 1394 (FireWire™)

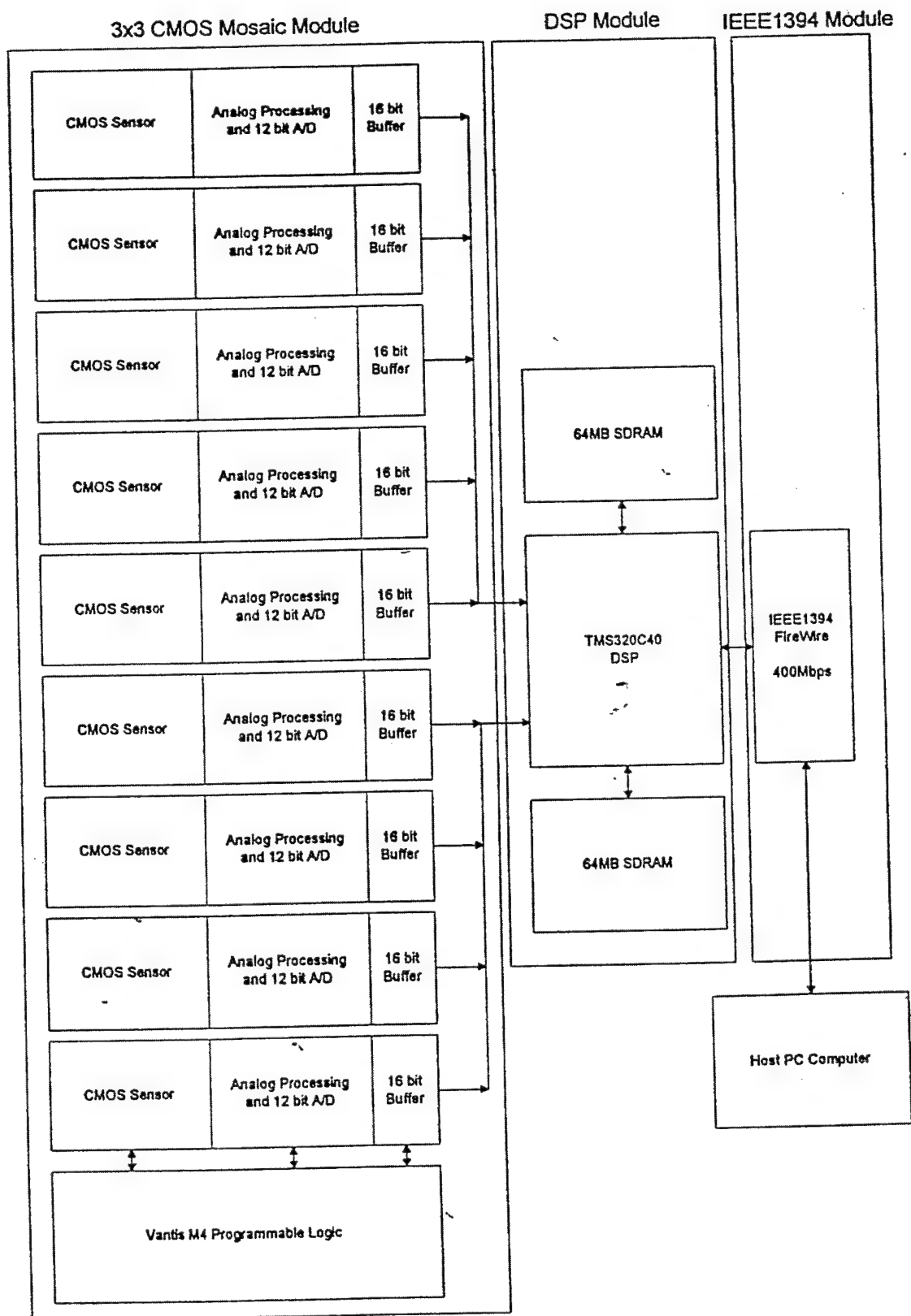This mammography system processes a huge amount image data for a single shot (about 40

Figure 16 Block diagram of 3x3 mosaic imager including DSP and IEEE 1394 electronics
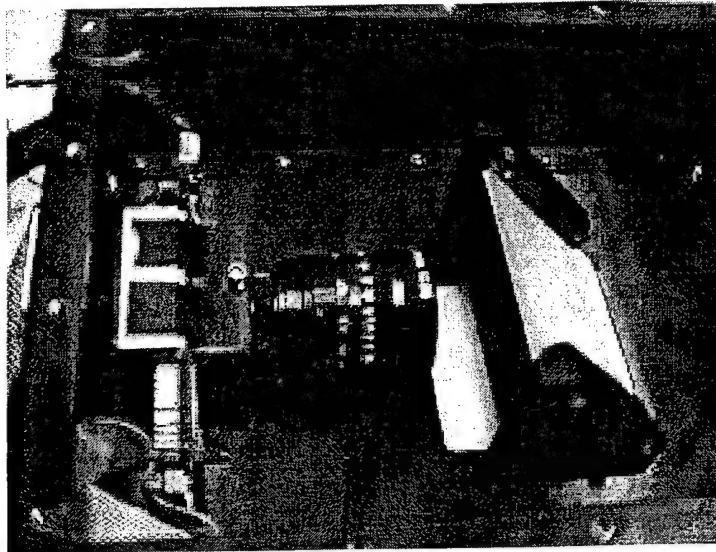
Figure 17A Photograph of mirror reflective prototype imager used to acquire x-ray images.
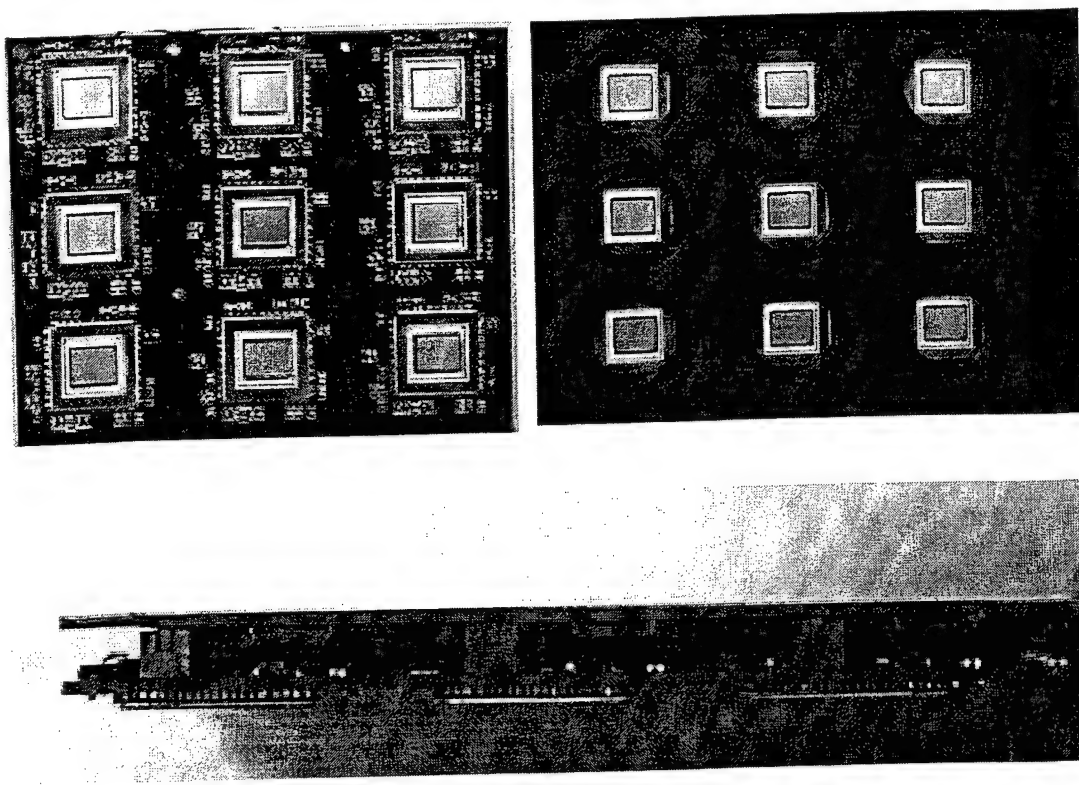

Figure 17B: Photographs of the 3x3 CMOS imager hardware module (top left), 3x3 CMOS mosaic with lens mounting plate attached (top right), and side view of 3x3 imager hardware module (bottom).

MB/image when using 6x6 imager). Therefore, a fast data transfer scheme is necessary. If the PC's parallel port were used, it would take over 40 seconds. We chose the faster serial data transfer method called IEEE 1394 or FireWire™. A current transfer speed for Firewire™ is 400 Mbits/sec. It takes one second to transfer a whole image under ideal situation. Figure 4 shows a block diagram of the FireWire connection between the PC and DSP using two FireWire™ boards. One FireWire™ plug-in board for PC is the off-the-shelve product that can be purchased by a vendor such as Texas Instuments. The other Firewire™ board was designed and fabricated by Sensor Plus. The board is a production quality printed circuit board (5"x7"). The board supports IEEE 1394 standards capable of transmitting/receiving data at 100, 200 and 400 Mbits/sec. It was fully tested and shown to operate at the required rate.

A custom lens design and manufacture was subcontracted to J.A. Optics (Utica, NY). They designed a 7-element lens, which, by simulation, had the required properties (f#1.1, 7μm spot size over full field at demagnification of 4.4 with an object area of 35 x 25 mm). Unfortunately, It took a long time to manufacture and the testing with this lens was not completed (due to the financial problems at Sensor Plus).

The lens apparently met specifications, and it is unlikely that significant improvement in performance (e.g. f# reduction) can be obtained with further development, at least in a lens of this size. We have reached this conclusion by discussion with lens designers and manufacturers.

The optical throughput of the system with this lens is about 1.5%. A higher throughput (lower f#) might be obtained with a much smaller lens, and with a much smaller image size, but then the number of lenses and sensors would have to be increased significantly (e.g. to 100 or 400) which we consider undesirable. Therefore we consider this lens to being close to the best available for this approach (generation I low cost imager).

Task 5 System Performance Tests

System performance tests were made on the digital imager quarter section and also on various intermediate prototypes.

A. Evaluation of correction schemes

To evaluate the quality of each correction scheme, we have carried out the quantitative analysis and visual analysis using three types of features:

- ☐ Circumscribed mass
- ☐ Spiculated mass
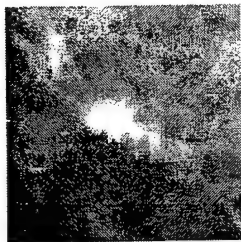- ☐ Micro-calcification.

Some of results in the visual analysis is presented. Refer to [spie '98 mi] for details. Note that we evaluated one of localized schemes - piece-wise linear interpolation and two of global schemes - cubic spline interpolation and bilinear interpolation. The evaluation of other schemes is underway. Results presented here simulate a system where four CCD sensors are used to create the digital mosaic. The method is identical for larger arrays (e.g. 6x6). By simulation it is meant that a mathematical model of the individual imaging components was employed instead of building the system. The overlap area of four tiles is where the most severe distortions are expected to occur. In order to evaluate the quality of the reconstructed features, each mammogram was translated and placed in a larger image such that the feature of interest falls on the overlap region of all four tiles. The mammograms are centered in a larger image using the center coordinates of the feature of interest as the center point of the larger image. The size of the large image is 1497x969 pixels and it is the same as that of the calibration pattern. Next four overlapping subsections of size 768x512 are extracted from the large image. Note that the resolution of the CCD's used in the imager is also 768x512 pixels. This will enable the application of the imager's distortion function to the mammogram images. It should be noted that each sub-image undergoes a slightly different transformation. The distortion function used was based upon a Barrel Distortion model. As it can be observed from the images in Figures 3 and 4 (previous task) this function is suitable to approximate the imager optics. Once each sub-image is distorted using the distortion function the three correction schemes, Piece-wise linear approximation, Bilinear interpolation and Spline interpolation were applied to correct each sub-image. Sections from the corrected sub-images that do not belong to the overlap area are extracted and then placed together to form the reconstructed mosaic. The sections that do not fall in the overlap area were of size 729x485 pixels. Consequently the reconstructed image is the same size as the initial large mammogram image.

In Figure 18, a series of images of the areas with features of interest are shown. These images were enhanced using the un-sharp filtering operation. As it can be observed the differences between each reconstruction scheme are better viewed under such a transformation. However, this operation is usually applied to images prior to using a computerized analysis algorithm. Therefore the effects of these differences will reflect in the performance of the computer algorithm. A simple edge enhancement and detection routine is applied to the filtered images. Results from this operation are shown in Figures 19-A,B, and C.
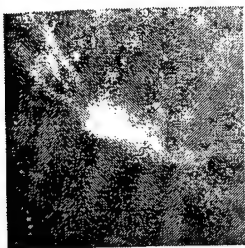
26

Original *Piece-wise Linear* *Bilinear* *Spline*

A Circumscribed Mass.

Original *Piece-wise Linear* *Bilinear* *Spline*

B Spiculated mass

Original *Piece-wise Linear* *Bilinear* *Spline*
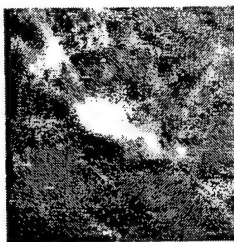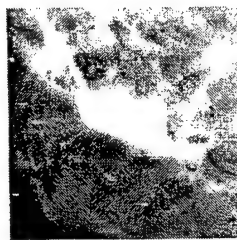
C Micro-calcification A.

Fig. 18 Original Image

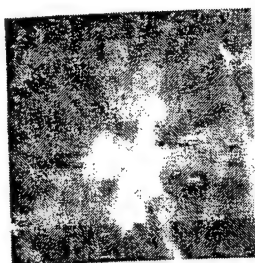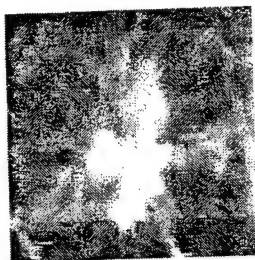Original   Piece-wise Linear   Bilinear   Spline
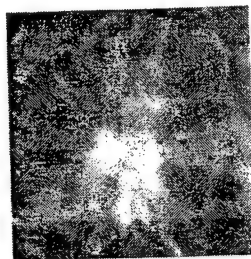
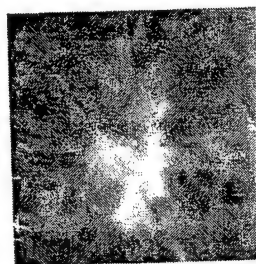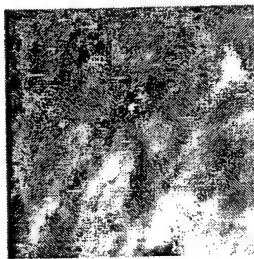A Circumscribed Mass.

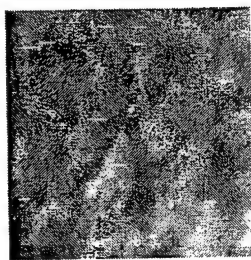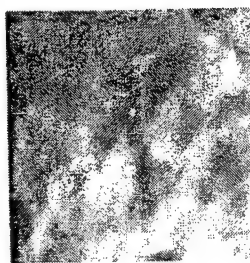Original   Piece-wise Linear   Bilinear   Spline

B Spiculated mass
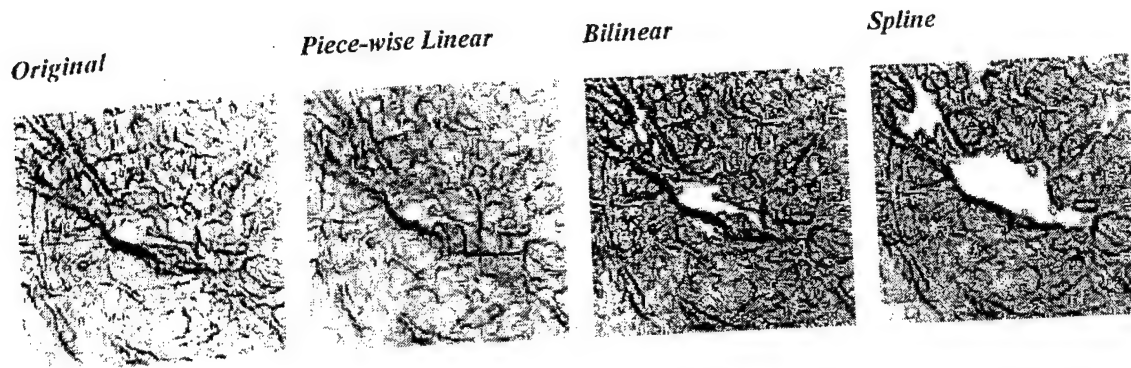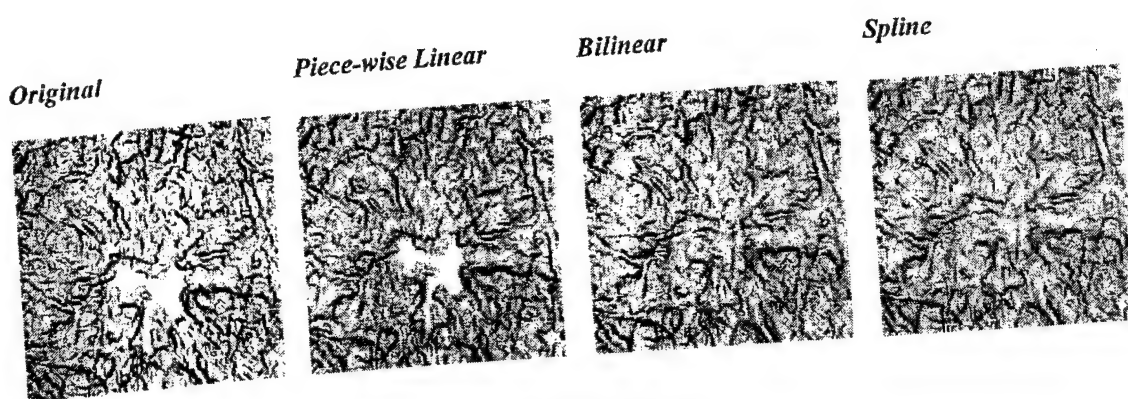
Original   Piece-wise Linear   Bilinear   Spline

C Micro-calcification A.
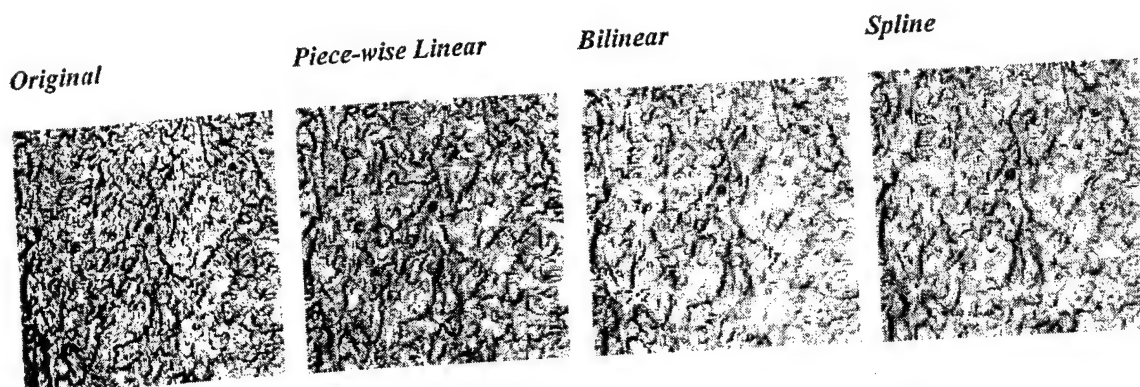
Fig. 19 Filtered Images

It is clear the computer algorithm's performance differs significantly for each of the images analyzed. When observing the smaller feature visually images, it can be argued that the piece-wise linear interpolation approach provided better results relatively even if some artifacts can be noticed as shown in Figures 18 and 19. However, when observing the calibration pattern, the cubic spline interpolation provided the best results as shown in Figure 4. The edge enhancement algorithm was least influenced when the images were reconstructed using the piece-wise linear scheme. It also can be assumed that the artifacts introduced are related to the calibration pattern employed. A different calibration pattern will introduce different types of artifacts. In Figures 19 and 18, we can observe the difference between the localized scheme and the global schemes. It is observed that the global schemes result in a difference from the original as compared with the localized scheme.

B. CMOS Sensor Image Quality Optimization

An evaluation of the VV5850 CMOS image was performed to demonstrate its feasibility for x-ray imaging. The evaluation included determination of both fixed pattern and random noise levels of the sensor, determination of noise levels for various exposure lengths, characteristics of dark current vs. exposure time, sensor linearity, and overall sensor signal-to-noise ratio, SNR. Figures 20.1 thru 20.8 show the results of these noise measurements:

Figures 20.1 and 20.2 show the noise performance for both fixed patterned and random sources with respect to the pixel readout frequency. From our measurements, the prototype imager exhibited better performance with readout rates in the range of 2-3MHz. This occurs since the overall leakage current at each pixel increases as the pixel rate decreases, hence increasing the fixed patterned noise. At 5MHz the on-chip high frequency clocking noise increased the overall noise.

Figures 20.3 and 20.4 show the fixed patterned noise and random noise with respect to exposure time. As expected, the noise levels rise with increasing exposure time, however at exposures of 2-3 seconds the overall noise only decreases approximately 4-5dB from the sensor's maximum SNR, as shown in figure 20.8. After subtracting the fixed patterned noise from the image, the overall noise present is significantly reduced and allows SNR's in the range of 60dB for longer exposures (2-3 seconds) and high pixel readout rates (2-3MHz).

Figure 20.5 shows the overall average dark current level with respect to exposure time. With a maximum signal range of 2400 ADU's, this CMOS sensor exhibited a range reduction by a factor of 2 (1200 ADU's) at an exposure time of approximately 26 seconds. At exposure times of 2 seconds as used to acquire test images, the reduction of the available signal range was only 5 percent. Thus, the dark current level did not inhibit the image SNR much.

All noise measurements during this period were conducted at approximately 25 degrees C temperature. However, the CMOS sensor was also tested at 4.4 degrees C to evaluate the overall SNR increase with temperature decrease. The following results were obtained:

29
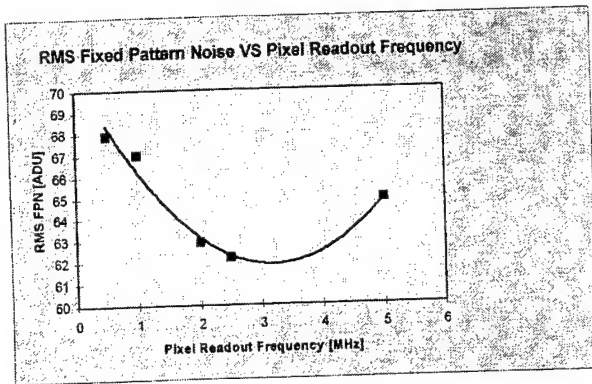
Fig 20.1 - S_{FPN} vs. f, N_{avg}=16, t_e=2 s.
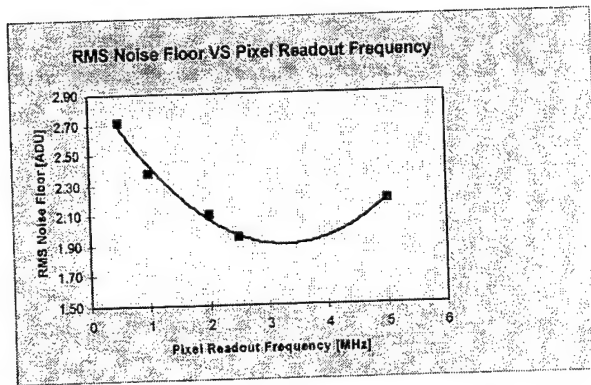
Fig 20.2 S_{FLOOR} vs. f, N_{avg}=16, t_e=2 s.
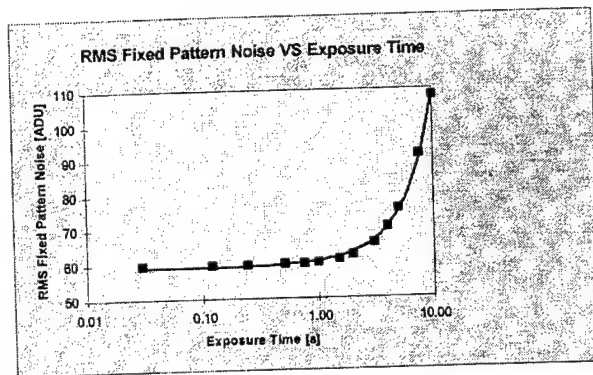
Fig 20.3 - S_{FPN} vs. t_e, N_{avg}=16, f=2.5MHz
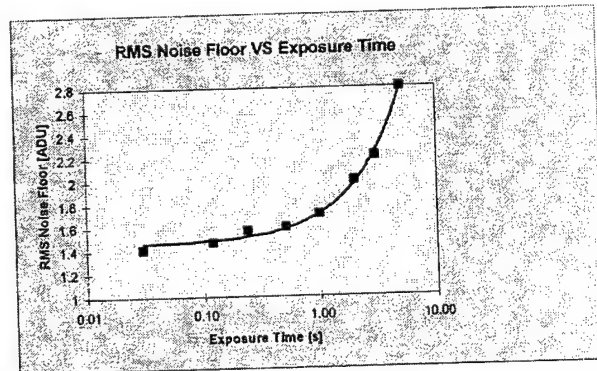
Fig 20.4 - S_{FLOOR} vs. t_e, N_{avg}=16, f=2.5MHz
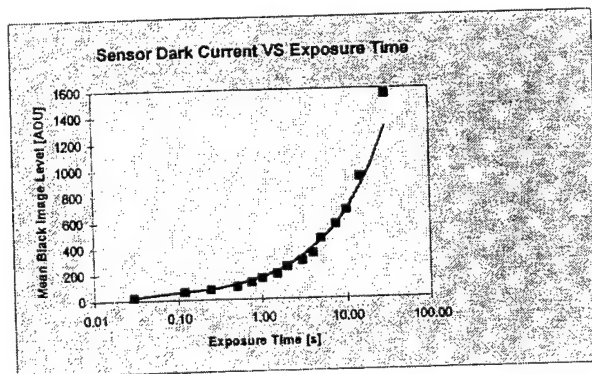
Fig 20.5 - S_{DARK} vs. t_e, N_{avg}=16, f=2.5MHz
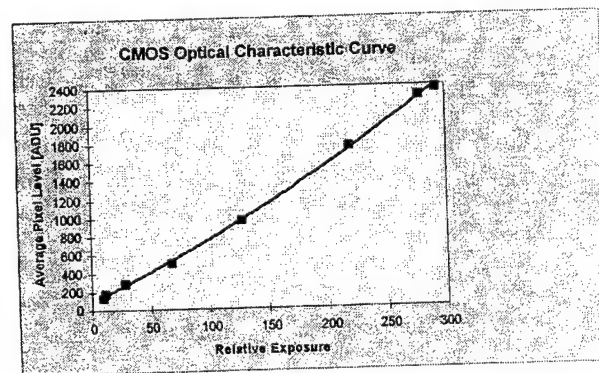
Fig 20.6 - R_{exp}, N_{avg}=16, f=2.5MHz
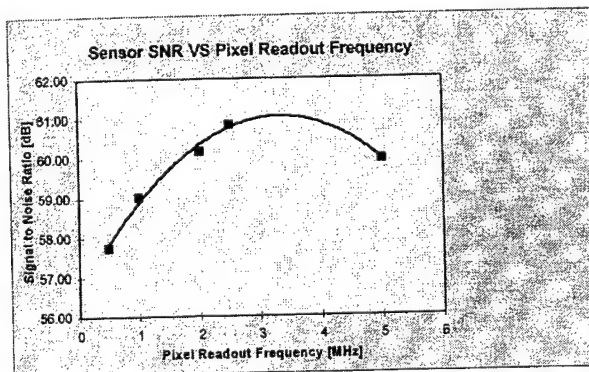
Fig 20.7 - SNR vs. f, N_{avg}=16, t_e=2 s, the noise value used was calculated after subtraction of SFPN from the acquired image.
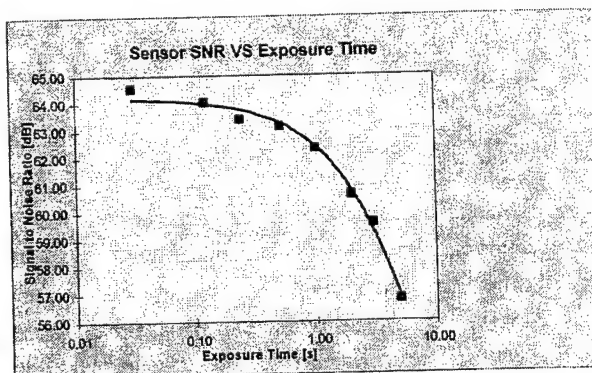
Fig 20.8 SNR vs. t_e, N_{avg}=16, f=2.5MHz, the noise value used was calculated after subtraction of SFPN from the acquired image.

30

Temperature [degrees C]	RMS Noise Floor [ADU's]	SNR [dB]251.7634.41.266
25	1.7	63
4.4	1.2	66

The minimum temperature for operation of the VV5850 sensor is 0 degrees C as specified by the manufacturer. Operation of the sensor would need to be close to 0 degrees C for optimal SNR performance.

C. X-Ray Testing at SUNY/Buffalo

Initially a small imager was built capable of 12-14 lp/mm using phosphor technology and a fiber taper coupled to a CCD. With this camera we were able to image fine specks of about 100 µm size as well as features of various phantoms, both high and low contrast. We are proceeding to use these images to further develop evaluational software. To provide a basis for comparative studies we have developed methods to extract digital images from a Fischer Mammotest Stereoscopic unit available to us on the U/B Main St. Campus in the Women=s Health Initiative. The 1024x1024x12bit images are transferred to a PC for evaluation at this point with a removable hard drive and as compressed files on floppy media. The proprietary file structure has been determined and we have begun to evaluate this 5x5 cm limited field of view imager using objective as well as anthropomoric phantoms in order be able to get quantitative comparisons with any imagers developed during this project.

Phantom development

We have found the commercial phantoms not to be completely satisfactory in evaluating digital mammographic equipment and have begun to develop our own proprietary phantoms using specks and very small diameter micro tubes. We expect some of these phantoms to be useful in any high resolution digital imaging application.

Light Intensity vs Gray Level (12/97)

$I = GL - 14.165$
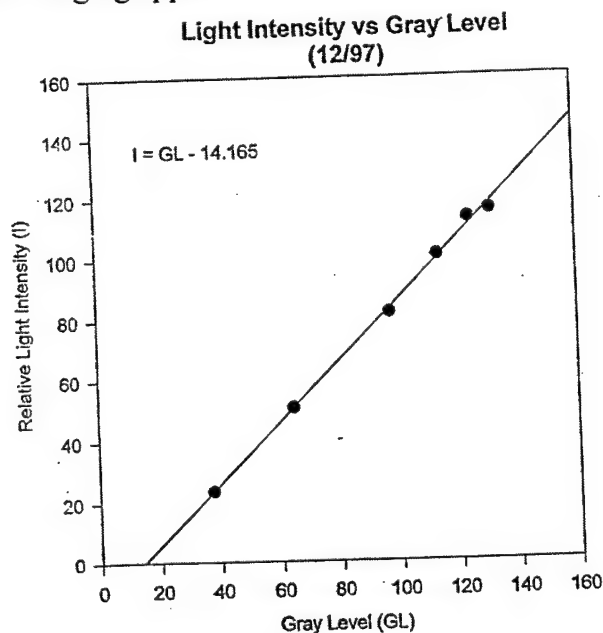
Fig. 21 Measured relation between gray level provided by the CCD detector and the light intensity which produced that level. This curve is used to linearize the CCD signal for various quantitative functional analyses.

31

H Line 176 - Vert lsf
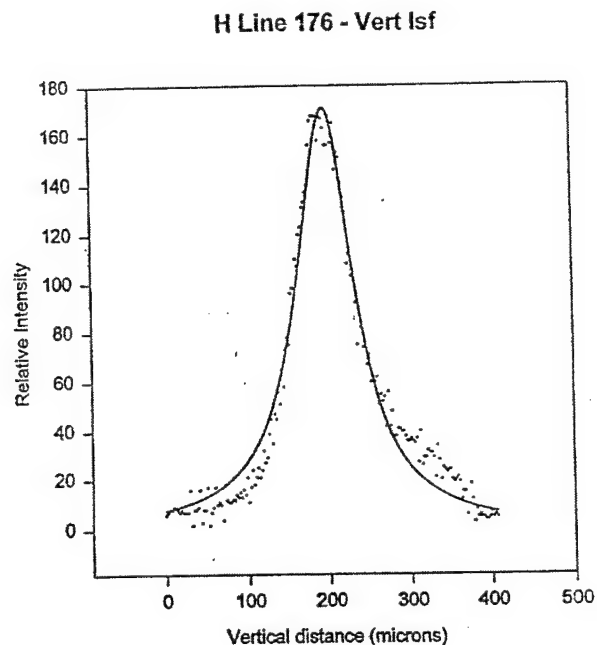
Fig. 22 Sample line spread function data obtained with a slit angled at approximately 1.5 degrees with respect to the CCD array. A curve fit to the data is also shown.

Preliminary CCD MTF

Legend:
- Presampled Horizontal $\{\exp(-\pi^*nu/23.4)\}$
- Presampled Vertical $\{\exp(-\pi^*nu/28.9)\}$
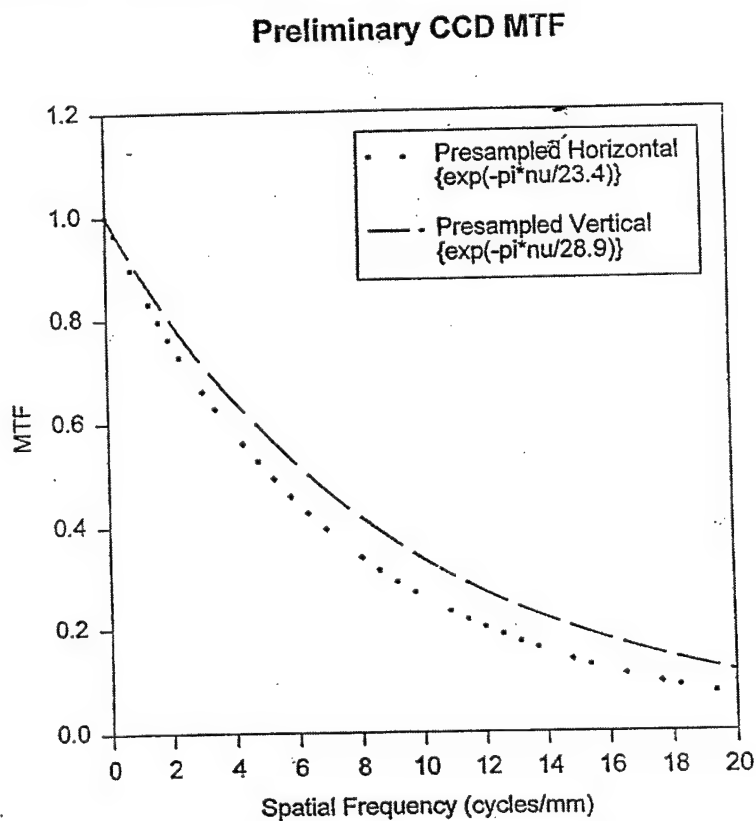
Fig. 23   Presampled MTF's obtained in the vertical and horizontal directions of the CCD array.

32

Channel #1 - X-ray Exposure

Channel #2 - Pin #3 from Bucky Connection

Exposure Factors: 40 mA 100 nsec

Small Grid
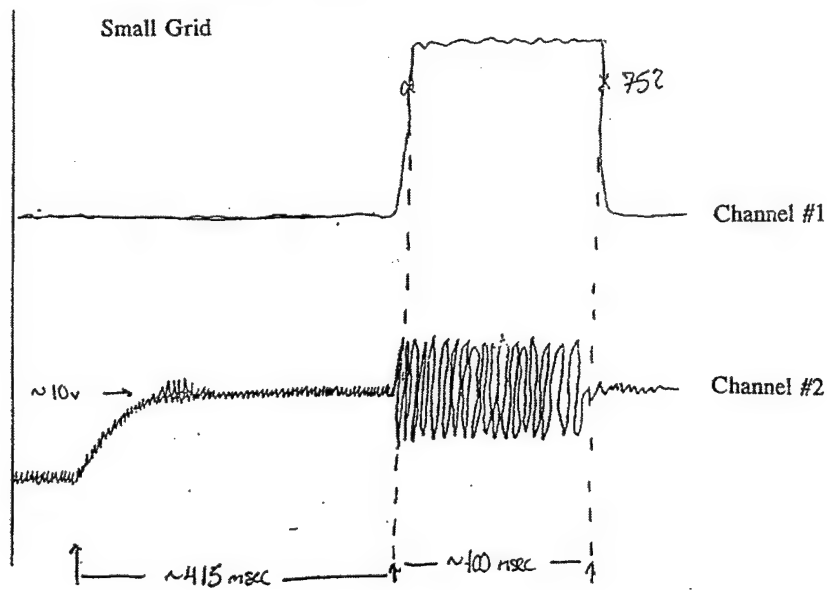
Fig. 24 Schematic of oscilloscope output showing x-ray exposure waveform in channel #1 and corresponding signal measured at pin #3 of the Bucky connector in channel #2.

Channel #1 X-ray Exposure

Channel #2 Pin #9 from Bucky Connector

Exposure Factors: 40 mA 100 ms

Small Grid

Note: Voltages are relative to 0.4v above ground.
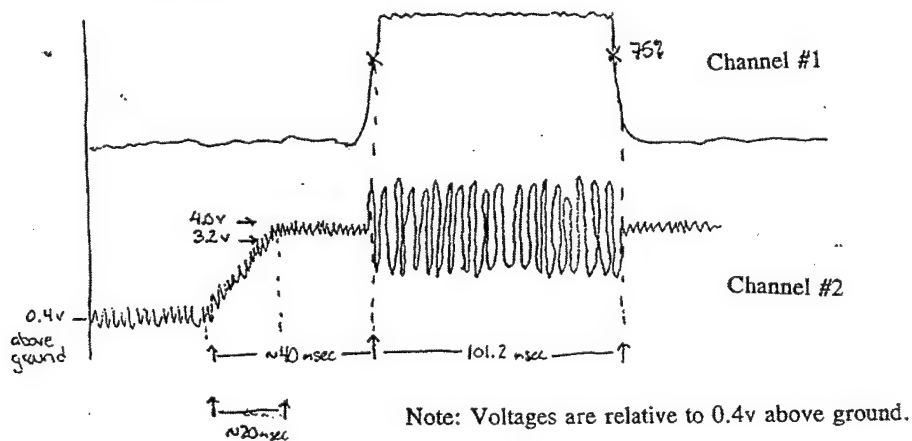
Fig. 25 Schematic of oscilloscope output showing x-ray exposure waveform in channel #1 and corresponding signal measured at pin #9 of the Bucky connector in channel #2.

33

D. Acquired X-ray Images

The first x-ray images were acquired using the single CMOS detector, lens, and standard Agfa MR detail phosphor screen (green). The system setup included a Bennett Contour mammography unit, the prototype CMOS imager, and a Pentium 166MHz computer with an internal TMS320C40 digital signal processor board for acquisition and image processing. A digital mammography phantom from Nuclear Associates was used as well as a standard resolution pattern to observe the characteristics of the imager. Each image was taken with a fixed exposure of 30kVp and exposure time of 2 seconds. The lens was an off-the-shelf f1.3, 12.5mm focal length CCTV lens. The x-ray images are shown in Figure 18 and 19 (following pages).

A red Eu doped Y2O2S phosphor screen was fabricated to improve the light collection efficiency of the x-ray system. The screen consists of a phosphor coating with a particle size of 30-40mg/cm2 and a TiO2 reflector layer all mounted to 1mm thick bakelite. This screen was tested during this year and produced approximately 25% greater intensity as compared with a Kodak standard high resolution gadolinium oxysulfide (Agfa MR Detail). The measured resolution using an off-the-shelf f/0.95 imaging lens was approximately 8 lp/mm and approaches the projected 10 lp/mm specified in the screen design. Figures 20 and 21 show the x-ray images obtained with this new screen:
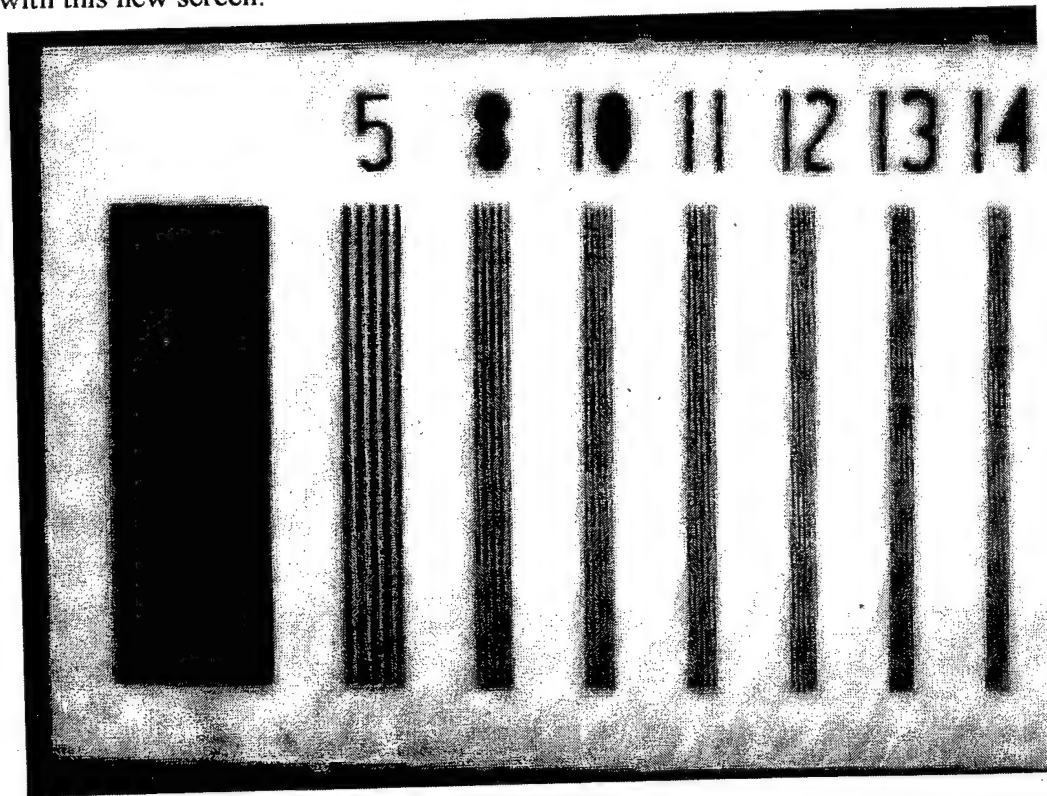
Figure 26 - This image shows the resolution obtained with a standard X-ray resolution bar pattern. The numbers at the top represent resolution in line-pairs per mm. The resolution approaches the limit of the detector at 12 lp/mm (0.0415 mm line width) since the pixel size at the image plane is 0.043 mm.
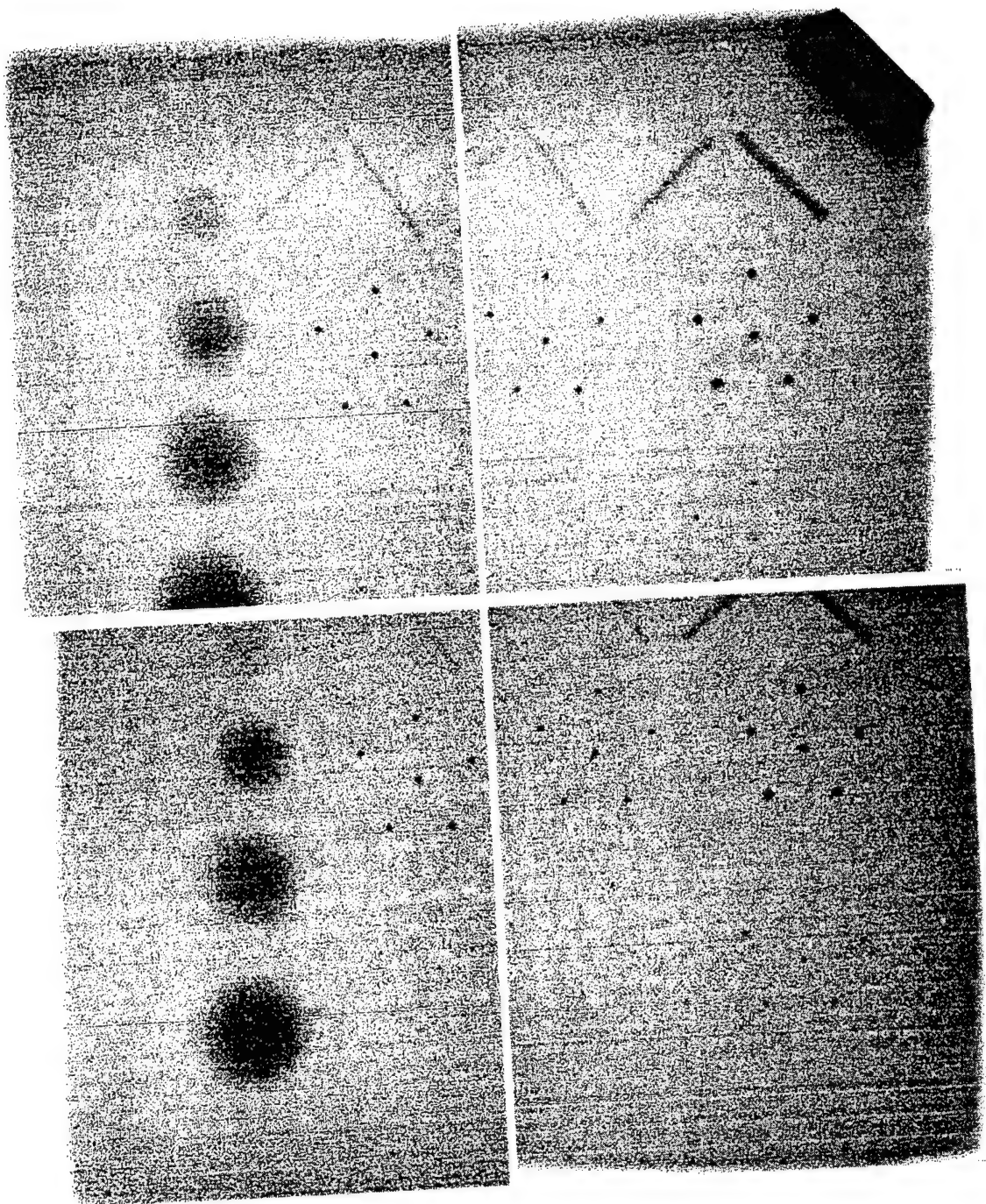
Figure 27 - 4 separate images acquired of a digital mammography phantom. The position of the phantom was translated to cover its full area. There are 4 large circular masses with varying sizes (left side of phantom), 4 clusters of structures representing microcalcifications, each cluster contains 6 structures in a star pattern, and 4 bar structures (top of phantom) at alternating 45 degree angles. The microcalcification structures range in size as: 540, 320, 240, and 200 microns. Note that it is difficult to extract visual information for the 200 micron structures.
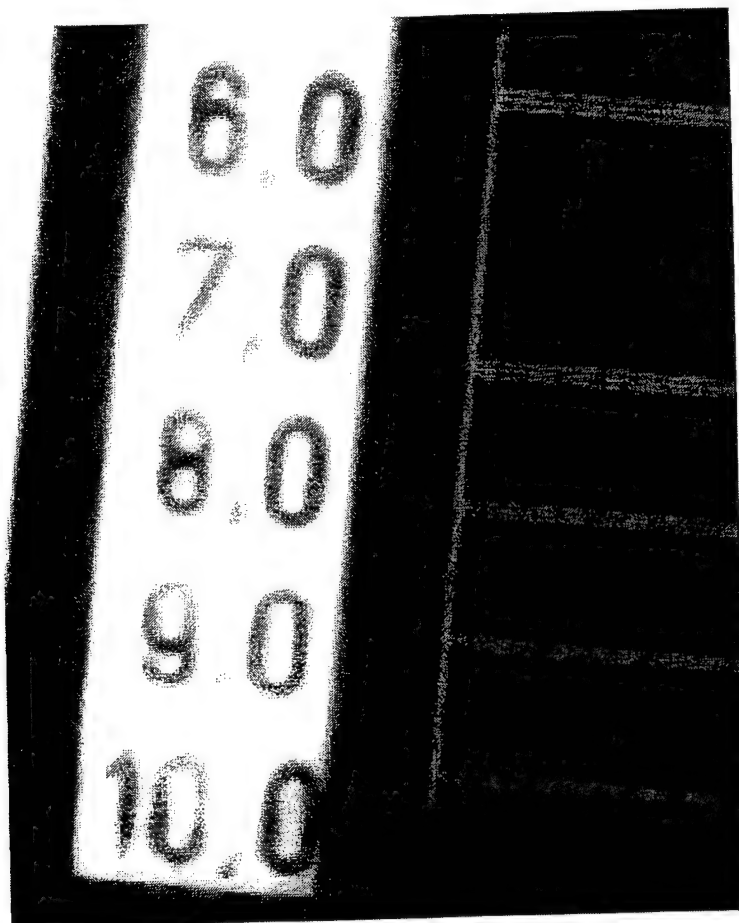
Figure 28: X-ray of resolution pattern using Eu doped Y2O2S phosphor screen (red). Numbers represent resolution in line pairs/mm. Note that 8 lp/mm is visible.
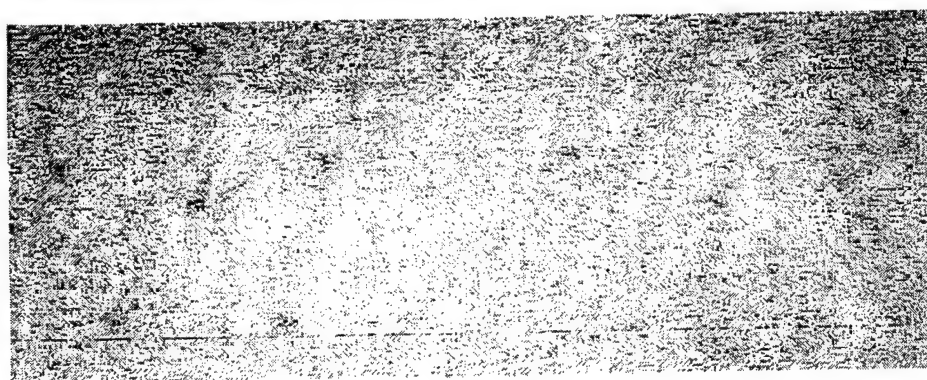
Figure 29: X-ray image of mammography phantom with 2 inch thick lucite. There should be two five point star patterns each containing 6 microcalcification structures.

2x2 Mosaic Image Reconstruction Tests

As a test of the image reconstruction, four optical images were acquired using a 2x2 section of the 3x3 imager. A single lens was used and four separate exposures were taken with the lens moved to adjacent sensors to cover a 2x2 area. A single lens was used since the custom lens was not available.

First, the calibration patterns were acquired and then images of a standard bar resolution pattern. Each calibration image was corrected for lens and geometric distortions and then the stitching boundaries were located. All the reconstruction coefficients were then saved and applied to the real images of the resolution pattern. Figures 21 and 22 show the original four images acquired before corrections and the resulting 2x2 corrected image respectively:

Figure 30: Four optical images of a bar resolution pattern acquired using a 2x2 section of the 3x3 imager.
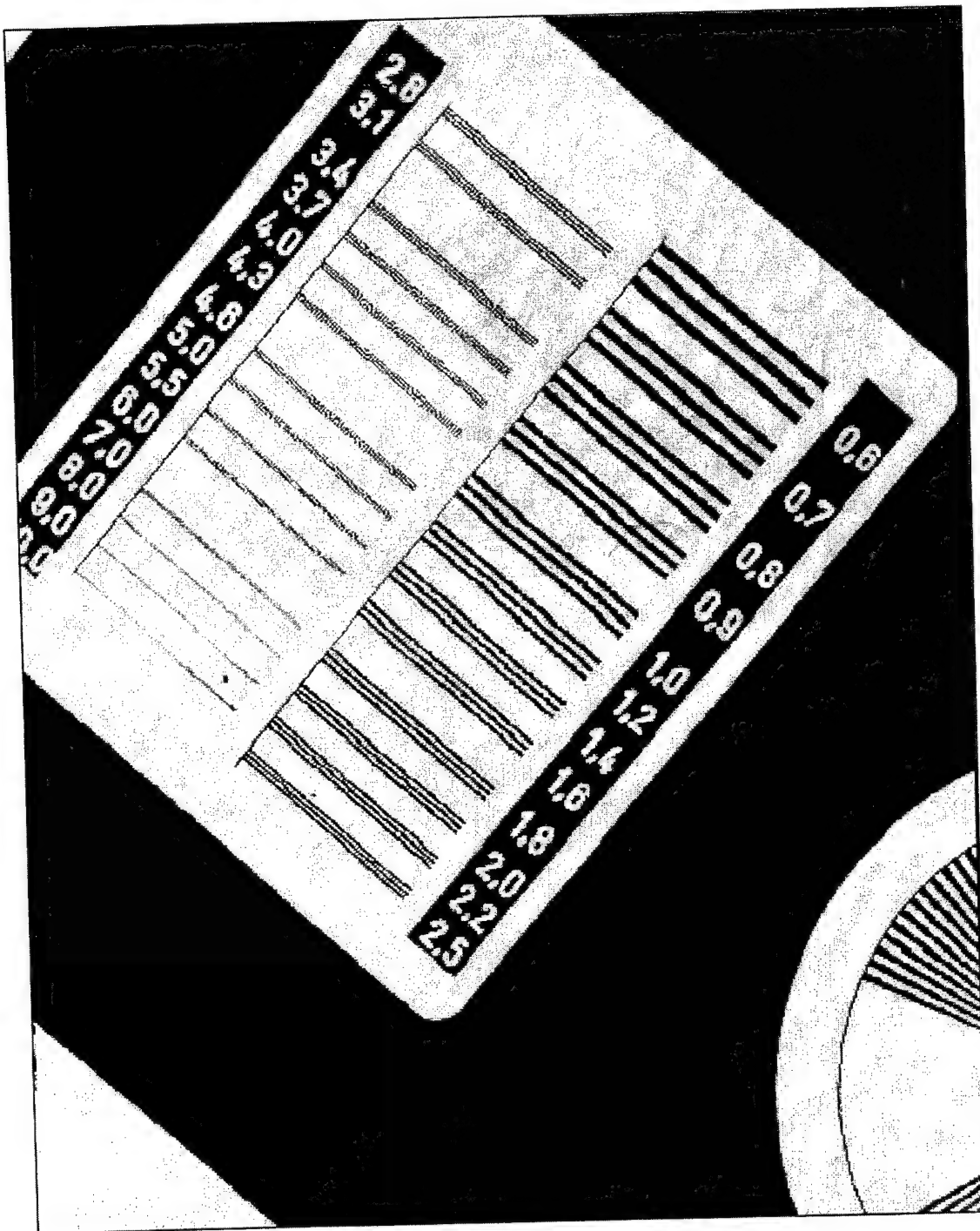
Figure 31: Reconstructed image of the four segments shown in figure30. The total image size is approximately 1800 x 1300 pixels.

Task 6 Prepare Radiographic Workstation Software

The software for viewing the complete image from the digital x-ray camera (Task 6A) was completed. It has standard features such as zooming, contrast/brightness enhansement, and file storage (save) capabilities. An example of an image is Fig. 31.

The remaining tasks (6A, 6B, and 6C) were not completed .

BUSINESS FAILURE OF SENSOR PLUS

Last fall Sensor Plus lost several key contracts and as a result failed as a business. All employees were dismissed in November 1999. Several employees remained in the area as independent contractors or associated with SUNY/Buffalo and therefore attempts were made to continue the mammographic imager research. However little work on the project was done since then because all funds were exhausted.

As indicated in this report, we believe that we have made advances in this area of digital imaging and wish the project to continue in some form. Attempts are being made to transfer the project (including all rights) to the State University of New York at Buffalo (SUNY/Buffalo), which is a subcontractor and has the resources to continue. Furthermore, the Principal Investigator of this project is a faculty member there. The SUNY/Buffalo administration has not, as yet, made the decision to accept the project but is negotiating. If it continues there, it will likely involve the modification of the imager to focus on the problems described below in "Suggestions for Future Work" (p. 45).

REVIEW OF COMMERCIAL DIGITAL MAMMOGRAPHIC IMAGE TECHNOLOGY

This project has the aim of developing a full-size, low-cost digital imager for mammography which is better than film/screen.   The advantages of digital imaging over film/screen (teleradiography, image quality/reproducibility, easy storage/availability, simple image enhancement, and computer-aided diagnosis) are well accepted. At the time the proposal for this project was written, it was unclear whether commercial x-ray imaging companies would develop a full-size digital imager in the near future. Several companies had tried but apparently had abandoned efforts.   Now, however, several commercial full-field imagers have now been developed and have received, or are close to, FDA approval. Technical information on these mammographic imagers were reported at the Fifth International Digital Mammography Conference at Toronto (June 2000) and also at the Fourth (Neymegan, June 1998).

- GE Medical Systems

The GE Senograhe 200D was the first full-field mammographic imager to be approved in the US by the FDA (Feb 2000). Images are also of high quality, better than film/screen. The image is 2000x2500 (100 μm) pixels and the screen size is 18x23 cm. The output is film, not computer or CRT display screen (apparently required for FDA approval). A computer-aided diagnosis developed by R2 (Image checkers) is an option. The selling price is in the $400k to $500k range.

- Fischer Medical Imaging

This device uses a slot scanner detector (24 x 3.2 mm). Fiber optic tapers to several CCD arrays are used. Data is stitched to form the final full size image. The image is 4000x5000 pixels (50 μm) and film output is also used. In this design the detector is smaller but the mechanical scanning system more complex. The x-ray tube current loading and curved receptors (compression plates) are a problem. It is nearing FDA approval. It is expected to cost more than the GE system.

- Trex Medical Imaging (Lorad and Bennet Divisions)

This unit is based on fiber optic taper coupling to a 3x4 CCD (19x25 cm) array or mosaic with 40 μm resolution (4800x6400 pixels). The DQE is 0.5 (DC) over a wide exposure range and is better than film/screen over the entire range. The output is a computer screen. Unfortunately the FDA has denied approval for this device.

- Cares-Built

The Cares-built Clarity 7000 is a general digital x-ray and not intended as a mammographic imager but it has an adequately high resolution (better than GE). It uses the same technology which is used for our imager (segmented image, multiple lenses/CMOS detectors) and as a consequence is low cost. It has not yet been approved by the FDA.

- Triexell (dpiX, Phillips, Siemens, Thomson, Varian, Xerox)

A consortium of companies are developing digital flat-panel detectors for digital x-ray imaging. A general radiography imager (ECR 2000) was announced in Feb 2000. It is likely that this group is also working on a mannographic imager.

There is some dispute as to whether the output should be on a computer display screen or as film (e.g. Kodak laser printer).

Other companies which are developing digital x-ray imagers are:

Fein Focus
A German company with a magnification feature 282x406mm, 127 µm pixels, 2:1 uses a thin film/screen transistor (amorphous se) technology. It will be introduced in Germany first.

Fuji Medical Systems
No information released but they are working on it.

Kodak
Uses xereographic method (laser scan) with film output.

Toshiba
Similar to Kodak

Comment

We conclude that these companies have developed a full scale x-ray imager which, The relatively high cost of these imagers ($250K to $500K) is likely to be acceptable to larger medical centers in US urban areas but may be unacceptable to smaller hospitals in rural areas or poorer countries. Yet it is the smaller hospitals that could benefit most by digital imaging, especially the teleradiology and computer aided diagnosis features.

Investigator List

A. Sensor Plus Inc. (Prime Contractor)
      Dr. Darold Wobschall, (Principal Investigator)
       Project Manager
       Overall System Design
       Design of Analog Electronics
      Scott Smith
       Design and testing of DSP hardware and CCD data acquisition
      H. Kim
       Design and testing of DSP parallel processor and image transmission system
      Myeoung Jeong
       Development of camera connection software, including distortion and alignment
      Tom Cordier
       Circuit assembly supervision
       Circuit board layout and EMI reduction
      Kevin Swindell
       DSP circuit testing and optical design

B. Sunnybrook (U. Toronto)
      Dr. John Rowlands
       Supervisor of XLV screen fabrication
       XLV design and testing

C. State University of New York at Buffalo
      Dr. Stephen Rudin
       Imager configuration and assuring compatibility with existing x-ray equipment
       Help with optical design
      Dr. Daniel Bednarek
      X-ray image testing
      William Granger
       Graduate student assisting Drs. Rudin and Bednarek

D. Consultants
      Dr. Thomas Vogelsong (VP) (left Infimed in June, 1999)
       Planning of workstation software
      Dr. Raj Acharya
       Software signal processing and image reconstruction
      J. Antonelli
       Design and fabrication of the lens.

KEY RESEARCH ACCOMPLISHMENTS

The overall achievement is that a low-cost digital x-ray imager was successfully designed and fabricated. The next stage in bringing the device to the production stage is to transfer the technology to a company with the capacity to manufacture, clinically test, and market the device.

Specific accomplishments are:

- o The mosaic or segmented imager method worked in that a large, high-resolution x-ray image was acquired by the use of an array of smaller, lower resolution detectors.
- o CMOS optical detectors were shown to be effective, lower-cost substitutes for the CCD detectors
- o The software distortion compensation methods developed were shown effective and allowed seamless images to be acquired.
- o A custom high-resolution, high light throughput lens was developed
- o The x-ray light valve technology was advanced.
- o Analog and digital electronics supporting the segmented imager were developed which was low-noise, high-speed, convenient, and low-cost.

REPORTABLE OUTCOMES

A. Meeting presentations (see appendix)

1.   Scott T. Smith, Daniel R. Bednarek, Darold C. Wobschall, Myoungki Jeong, Hyunkeun Kim, Stephen Rudin, Evaluation of a CMOS Image Detector For Low Cost and Power Medical X-ray Imaging Applications, SPIE Medical Imaging, vol. 3659, 1999.

2.   Vivek Swarnakar, Scott T. Smith, Myoungki Jeong, Hyunkeun Kim, and Darold C. Wobschall, Evaluation of A Digital Mosaic Mammographic Imager, 4th International Workshop on Digital Mammography, June 1998.

3.   Scott T. Smith, , Vivek Swarnakar, Myoungki Jeong, and Darold C. Wobschall, Parallel hardware architecture for CCD-mosaic digital mammography , SPIE Medical Imaging, vol. 3335, 1998.

4.   Vivek Swarnakar, Myoungki Jeong, Scott T. Smith, Hyunkeun Kim, and Darold C. Wobschall, Effect of the reconstruction technique on the quality of digital mosaic mammograms, SPIE Medical Imaging, vol. 3340, 1998.

5.   V. Swarnakar, M. Jeong, R. Wasserman, E. Andres, and D. Wobschall, An Integrated Distortion Correction and Reconstruction Technique For Digital Mosaic Mammography, SPIE Medical Imaging, vol. 3031, pp. 673, 1997.

B. Funding by NASA

A Phase I SBIR research contract "A Portable X-ray Imager for Teleradiology Applications", PI: S. Smith, was funded by NASA. It involved the development of a digital x-ray imager similar to that shown in Fig. 17. Unfortunately Phase II was not funded.

C. Support of Students

The following graduate students at SUNY at Buffalo were supported by this contract:

    Scott T. Smith
    Hyunkeun Kim
    Myoungki Jeong
    Thomas Cordier
    Richard Wasserman
    Vivek Swarnaker
    William Granger
    Eugene Andres
    Pia-Krista Reippo

D. Prototype Imager

The hardware (and software) for the prototype imager, as indicated by the photographs of Fig. 17, was fabricated with pre-production quality standards and are suitable for clinical testing. The prototype was transferred to SUNY/Buffalo with the expectation that it will be used there.

CONCLUSIONS

A digital x-ray imager of high resolution (40 um) and expandable to an arbitrarily large size hss been developed and tested. The characteristics have been described in detail in the body of this report. We have achieved our goal from the engineering point of view but it is unclear whether the imager can compete with others which are commercially available.

Five years ago, when the proposal for this project (digital mammographic imager by optical methods) was written, it was not clear if commercial full-field imagers would be developed in a reasonable time frame. As indicated by the above review of commercial imagers, they now have been developed and do produce a high quality image, although the cost of the equipment is high. Therefore there is little economic incentive for most U.S. companies to take the technology developed here into the production stage as a full-field mammographic digital imager.

In the opinion of the Principal Investigator, there still is a need for a low-cost, full-field imager for use in remote (rural) areas or in underdeveloped countries. Specifically the advantages of digital imaging in these areas include teleradiograpic capability and computer aided diagnosis. The technology developed here is close to fulfilling this need but would require that the most recently developed CMOS detectors (released Summer/Fall of 2000) be incorporated into the design for improved sensitivity, and then clinical testing be done. However we recognize that the Cares-built digital imager (Clarity 7000, see www.caresbuilt.com), which uses a similar optical technology to that developed here, is further along in the development. It has already in production for chest x-ray, already has the required high resolution, and is basically a low-cost technology. Therefore it is a better candidate for a commercial, low-cost mammographic imager.

Suggestions for Future Work

There are three related areas for which the technology developed here is well suited. The first is stereo (or tomographic) imaging of the breast for diagnostic purposes (in contrast to screening). The stereo technique has been tested by Maidment and Albert (A. Maidment and M. Albert, "A Clinical Study of Calcifications Imaged by 2-D and 3-D Digital Mammography" , Proceeding of Era of Hope Conference [Atlanta], June 2000) among others, and shown to allow the viewer to distinguish microcalcifications from the background structure and also to allow the structure of the microcalcifications to be seen. For this purpose, a high resolution (30 to 50 um) image is desirable. A low-noise, high resolution image also allows microcalcifications to be classified into probable benign/malignant on the basis of size (100 um threshold), as described by Fields (F. Fields, "Analysis of the Influence of Pixel Size to Diagnostic Accuracy" 5th Inter. Conf. on Digital Mammography [Toronto], June 2000). The somewhat higher x-ray dose needed to obtain

a clear stereo image is of little consequence since the purpose is to avoid biopsy rather than to screen the general population.

The digitized imager in its present form, or better with the updated CMOS detectors, is well suited for this purpose. The image size, resolution, digital processing capabilities, and moderate cost are close to ideal. The institute best suited to carry out research demonstrating this is SUNY/Buffalo. A digital mammographic image group is being established there with an affiliation by Roswell Park Cancer Institute (RPCI). Many breast cancers are diagnosed and treated at RPCI so that the addition of the stereoscopic imaging facility is considered highly desirable from the clinical and research perspectives.

Another related device for which this technology is suitable is a portable digital x-ray for emergency medicine or field hospital use. Here the specific characteristics of low-cost, light weight, and ability to combine (stitch) images are important, when combined with the general digital imaging advantages of fast image acquisition and telecommunication (preferably by satellite, or cellphone if necessary).

Still another related technology is a large display or workstation for viewing digital mammograms. The mosaic or stitching technology developed here can be used for display as well as image capture. Multiple projection elements may be combined to produce a bright, high resolution, seamless display similar to film mammogram viewing stations or lightboxes. This work also can be done at SUNY/Buffalo.

REFERENCES

1.   Feuer, E.J., Wun, L.M., Boring, C.C., Flanders, W.D., Timmel, M.J., Tong, T., "The lifetime risk of developing breast cancer," J. Nat'l. Cancer Instit, 1993, June 2;85(11):892-897.

2.   Jain, Anil K., Fundamentals of Image Processing, Prentice Hall, 1989.

3.   Mayer, R., "Direct imaging of x rays with a CCD using hardware processing", Review of Scientific Instrumentation 62(2), pp.360-363, February 1991.

4.   Karellas, A., Liu, H., Harris, A and D'Orsi, C., "Operational Characteristics and Potential of Scientific-Grach Charge Coupled Devices in x-ray Imaging Applications," SPIE Vol. 1655 (1992), p. 85.
5.   Kutlubay, E., "Real-Time, Light-Weight X-Ray Imager," Yearly report to U.S. Army (May 1995).

6.   Lefebvre, F., Gilles, R., Benali, H., Vanel, D. and DiPaolo, R., "Automatic detection of microcalcifications on digitized mammograms", Scientific Program, 79th Scientific Assembly and Annual Meeting, Radiological Society of North America, Nov, 1993.

7.   Yaffe, M.J., "Digital mammography", Syllabus: A Categorical Course in Physics Technical Aspects of Breast Imaging, Presented at 78th Scientific Assembly and Annual Meeting, Radiological Society of North America, Nov, 1992.

8.   Freedman, M., et al, "Digital Mammography: Tradeoffs between 50 and 100 Micron Pixel Size," 1995 SPIE Medical Imaging Conference, paper 2432-09.

9.   Kutlubay, M., R. Wasserman, D. Wobschall, R. Acharya, S. Rudin, and D. Bednarek, "Cost Effective, High-Resolution, Portable Digital X-ray Imager," SPIE Vol. 2432, (p 554), (San Diego, Feb. 1995).

10.   Henry, J.M., Yaffe, M.J., Pi, B., Venzon, J., Augustine, F., and Tumar, T.O., "Solid state x-ray detectors for digital mammography," Medical Imaging 1995: Physics of Medical Imaging, Ed. R.I. Van Metter and J. Beutel, Proc. SPIE 2432, 392-401 (1995).

11.   Que, W., and Rowlands, J.A., "X-ray imaging using amorphous selenium: Inherent spatial resolution," Med. Phys. 22, 365-374 (1995).

12.   Zhao, W., and Rowlands, J.A., "Digital radiology using self-scanned readout of amorphous selenium," Medical Imaging 1993: Physics of Medical Imaging Ed. by: R. Shaw, Proc. SPIE 1896, 114-120 (1993).

13.   Zhao, W., and Rowlands, J.A., "X-ray imaging using amorphous selenium: Feasibility of a flat panel self-scanned detector for digital radiology." Med. Phys. (in press).

14.   Schaffert, R.M., Electrophotography, (Focal Press, London, 1980), p. 284.

15.   Fahrig, R., Rowlands, J.W. and Yaffe, M.J., "X-ray imaging using amorphous selenium: Detective quantum efficiency of photoconductive image receptors for digital mammography, Med. Phys. 22, 153-160 (1995).

16.   Fahrig, R., Rowlands, J.A. and Yaffe, M.J., "X-ray imaging using amorphous selenium: Optimal spectra for digital mammography, Med. Phys. (submitted)

17.   Rieppo, P.M. and Rowlands, J.A., "Amorphous selenium liquid crystal light valve for x-ray imaging," Medical Imaging 1995: Physics of Medical Imaging, Ed. R.L. Van Metter and J. Beutel, Proc. SPIE 2432, 228-236, (1995).

18.   S. Hejazi and D. Trauernicht, "Potential image quality in scintillator CCD-based x-ray Imaging system for digital radiography and digital mammography, SPIE, Newport Beach, 1996.

Evaluation of a CMOS Image Detector For Low Cost and Power Medical X-ray Imaging Applications

Scott T. Smith, Daniel R. Bednarek, Darold C. Wobschall, Myoungki Jeong,
Hyunkeun Kim, Stephen Rudin

(SS, DW, MJ, HK, Sensor Plus Inc., 4250 Ridge Lea Rd., Amherst, NY 14226; DB, SR, Dept. of Radiology, SUNY at Buffalo, NY 14215)

ABSTRACT

Recent developments in CMOS image detectors are changing the way digital imaging is performed for many applications. The replacement of charge coupled devices (CCD's), with CMOS detectors is a desirable paradigm shift that will depend on the ability to match the high performance characteristics of CCD's. Digital X-ray imaging applications (chest X-ray, mammography) would benefit greatly from this shift because CMOS detectors have the following inherent characteristics:

- Low operating power (5-10 times lower than CCD/processing electronics)
- Standard CMOS manufacturing process (CCD requires special manufacturing)
- On-chip integration of analog/digital processing functions (difficult with CCD)
- Low Cost (5-10 times lower cost than CCD)

The achievement of both low cost and low power is highly desirable for portable applications as well as situations where large, expensive X-ray imaging machines are not feasible (small hospitals and clinics, emergency medical vehicles, remote sites). Achieving this goal using commercially available components would allow rapid development of such digital X-ray systems as compared with the development difficulties incurred through specialized direct detectors and systems. The focus of this paper is to evaluate a CMOS image detector for medical X-ray applications and to demonstrate the results obtained from a prototype CMOS digital X-ray camera. Results from the images collected from this optically-coupled camera are presented for a particular lens, X-ray conversion screen, and demagnification factor. Further, an overview of the overall power consumption and cost of a multi-sensor CMOS mosaic compared to its CCD counterpart are also reported.

Keywords: CMOS image sensor, digital X-ray imaging, digital mammography, digital imaging, medical imaging, low power imaging

1. INTRODUCTION

Complementary metal oxide semiconductor (CMOS) image detectors are increasingly replacing charge-coupled devices, (CCD's), for many applications requiring low power and low cost. Applications such as digital photography, machine vision, and video conferencing all benefit from CMOS technology by allowing a single CMOS device to replace the complex and expensive circuitry associated with CCD imaging. However, CMOS imaging technology has only begun to present itself to the scientific and medical imaging communities due to performance limitations. The discussion below explains the differences associated with CMOS and CCD detectors and why CMOS detectors have been limited to high-illumination applications.

CMOS detectors differ considerably from CCD's in terms of the readout electronics onboard the sensors. The pixel structure within an active pixel (AP) CMOS sensor leads to greater fixed pattern noise (FPN) than a typical CCD sensor. Also, the random noise floor of the pixel output circuitry in CMOS sensors is usually higher.
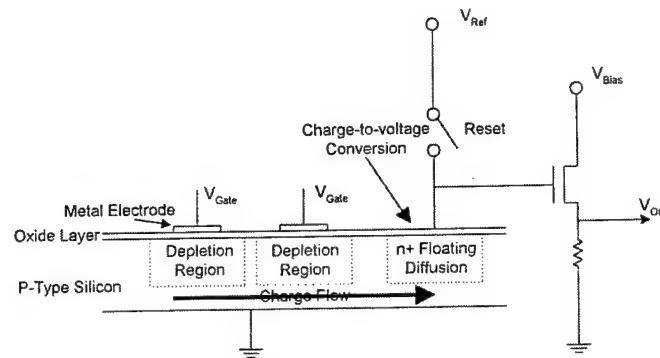
Figure 1.1 - Typical MOS capacitor structure of a CCD image sensor. Shown are two adjacent pixels, or charge wells and the output conversion circuitry. The pixels are read out by moving charges through adjacent pixels. Columns are read in parallel and each row is shifted down to an output buffer row. Finally each pixel charge packet is read out in serial through a charge-to-voltage converter and output amplifier.
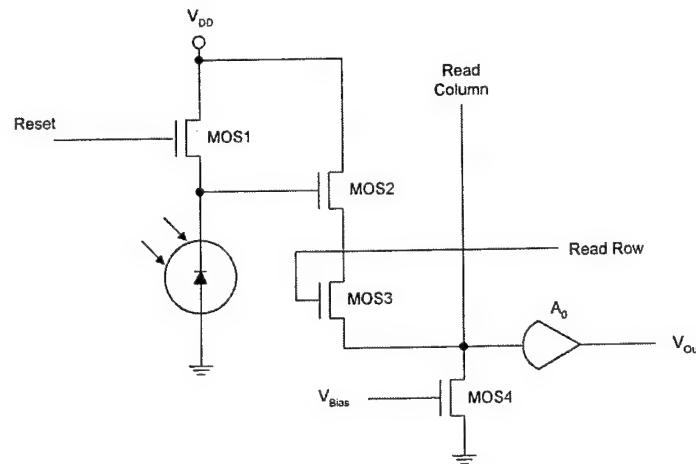

Figure 1.2 - Typical pixel circuitry for an active pixel CMOS sensor. Each pixel contains several CMOS transistors to transfer the analog voltage level to the output buffer. The voltage sensed at MOS2 holds until read_row is enabled, then it is transferred to the output through an output amplifier using read_column.

Figure 1.1 above shows the pixel readout structure for a typical CCD sensor while figure 1.2 shows the electronic pixel structure for an active pixel CMOS sensor. The main difference between the CMOS and CCD pixel structures is the use of amplifying transistors for each pixel in the CMOS structure. Since, several amplifiers are used to transfer the analog pixel voltage, variations due to inconsistencies in transistor characteristics leads to greater FPN. This noise will be present as variations in both individual pixel levels as well as entire columns (appears as stripes in image) [1,2]. Thus, to effectively use CMOS image detectors for applications requiring high SNR, a scheme of FPN cancellation must be employed. A cancellation technique is explained in a following section.

The production techniques of CCD's and CMOS sensors also varies such that the CMOS sensor may be fabricated using standard CMOS IC techniques whereas CCD's require special foundries. This leads to low cost CMOS sensors that may contain a mixture of on-chip processing circuitry minimizing external circuitry. Since CMOS sensors use standard circuitry they are inherently low power devices making portable imaging systems much more feasible. The remaining sections of this paper present the results of a particular CMOS sensor in terms of feasibility for low power and low cost X-ray imaging applications with discussions of FPN cancellation and sensor characteristics.

2. CMOS SENSOR CHARACTERISTICS

2.1 VV5850 CMOS Image Detector

Characteristics essential for high resolution, low-light imaging include large pixel size, high dynamic range, high quantum efficiency, and high pixel density. The combination of large pixel size and high pixel density on a CMOS sensor will allow more efficient light gathering since the demagnification factor from object to image plane will be reduced. Based on aforementioned criteria, the CMOS sensor chosen for evaluation was the VV5850 monochrome image sensor from VLSI Vision Lmtd. A brief list of specifications is shown in the table below[6]:

Table 1: VLSI Vision Lmtd. VV5850 Monochrome CMOS Image Sensor

Parameter	Value	Units
Resolution	800 x 1000	Pixels
Dynamic Range	66	dB
Max. Pixel Readout Frequency (for 66dB)	5	MHz
Pixel Output Buffer	1	
Pixel Dimensions	10.8 x 10.8	um^2
Quantum Efficiency (500-800nm)	40-50	%
Operating Power	125	mW
Pixel Fill Factor	25	%
Approximate Cost (US $)	100	$

2.2 Discussion of Noise and Dynamic Range

CMOS Detector Signal-to-Noise Ratio, SNR$_{CMOS}$ [5]

$$SNR_{CMOS} = \frac{S_{max} - S_{min}}{\sqrt{\left\langle S_{FPN}^2 \left(f, t_e \right) \right\rangle + \left\langle S_{FLOOR}^2 \left(f, t_e \right) \right\rangle}} \tag{1}$$

where SNR_{CMOS} is the signal-to-noise ratio of the CMOS detector, S_{max} is the maximum signal level a pixel may have and occurs when a charge well becomes saturated, S_{min} is the average pixel level caused by dark current leakage, $<S_{FLOOR}>$ is the noise floor of the CMOS detector as a function of the pixel readout frequency, f, and the exposure time, t_e. $<S_{FLOOR}>$ includes shot noise, reset noise, dark noise, and other on-chip random sources. $<S_{FPN}>$ is the fixed pattern noise generated for each pixel which also depends on f and t_e. Since the FPN of a CMOS sensor is considerably higher than a CCD, it is important to quantify this value, determine its overall contribution to the SNR, and determine the maximum SNR through cancellation of this noise. The measurement of $<S_{FPN}>$ is accomplished by performing the following operations:

Acquire N_{avg} dark field (no exposure) images and average over each pixel, i, j:

$$\overline{S_D}(i,j) = \frac{1}{N_{avg}} \sum_{n=1}^{N_{avg}} S_n(i,j) \qquad \begin{cases} i = 1,2,3,...,N \\ j = 1,2,3,...,M \end{cases} \tag{2}$$

This final average dark field image, S_D, represents an image with S_{FLOOR} significantly reduced leaving mostly FPN as the primary noise source. This allows measurement of the FPN as well as the remaining combined noise sources as follows:

FPN image is approximated as an average dark field image:

$$S_{FPN} \approx \overline{S_D} \tag{3}$$

$<S_{FLOOR}>$ is approximated as:

$$S_{FLOOR} \approx S - \overline{S_D} \tag{4}$$

3

where S is a single dark field image not part of the set of averaged dark field images in S_n. Equations 1-4 represent the method used to quantify the noise sources of the CMOS sensor for this paper.

3. EXPERIMENTAL RESULTS OF X-RAY CAMERA

3.1 X-ray Conversion and Optical System

The CMOS sensor was fitted with a standard 1" format CCTV lens with a focal length of 12.5 mm and f-number of 1.3. The lens was focused with a demagnification factor of approximately 4.0 and coupled with a standard high resolution gadolinium oxysulfide (Agfa MR Detail) phosphor screen for X-ray conversion. The pixel size at the screen was approximately $43um^2$ with an overall imaging area of 43 mm by 34.4 mm. This setup is common among similar CCD based imagers which use lens-coupling[3]. Since a standard lens was used, non-uniform illumination occurs across the sensor array primarily at the edges. To correct the flat field response of the optical system the following calculations were applied to each image:

Intensity Correction For Optical Non-uniform Illumination of Sensor[8]

$$\overline{S_c} = \frac{1}{n \cdot m} \sum_{i=1}^{n} \sum_{j=1}^{m} S_c(i,j) \tag{5}$$

$$Y_c(i,j) = \frac{\overline{S_c}}{S_c(i,j)} \qquad \begin{cases} i = 1,2,3,...,n \\ j = 1,2,3,...,m \end{cases} \tag{6}$$

$$S'(i,j) = S(i,j) \cdot Y_c(i,j) \qquad \begin{cases} i = 1,2,3,...,n \\ j = 1,2,3,...,m \end{cases} \tag{7}$$

where $\overline{S_c}$ is the mean pixel value in the image S_c, Y_c are the correction coefficients, S' is the final corrected image and S is the uncorrected image matrix. The image S_c is an average of 8 acquired images of the same uniform intensity field. Once the coefficients Y_c are calculated they are stored in the system for future application. Each image that is individually acquired is corrected for non-uniform intensity with these coefficients. Also, the FPN and dark current are subtracted from the images before the intensity corrections are calculated.

3.2 X-ray Imaging System Setup

The system setup included a Bennett Contour mammography unit, the prototype CMOS imager, and a Pentium 166MHz computer with an internal TMS320C40 digital signal processor board for acquisition and image processing. A digital mammography phantom from Nuclear Asssociates was used as well as a standard resolution pattern to observe the characteristics of the imager. Each image was taken with a fixed exposure of 30kVp and exposure time of 2 seconds.

3.3 Results of Noise Characteristics

Based on equations 1-4 the following noise measurements were obtained from the CMOS sensor:
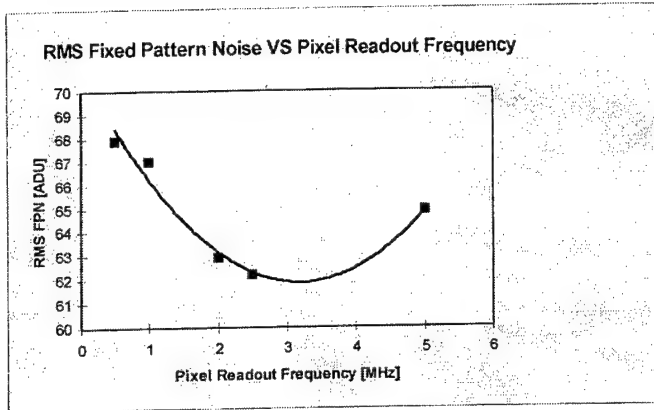
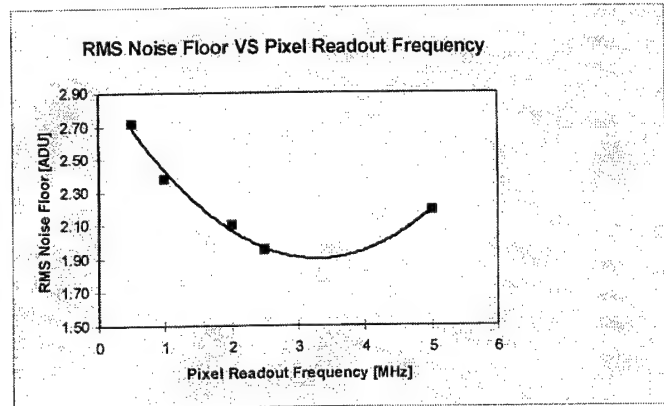**Figure 3.1** - S_{FPN} vs. f, N_{avg}=16, t_e=2 s.

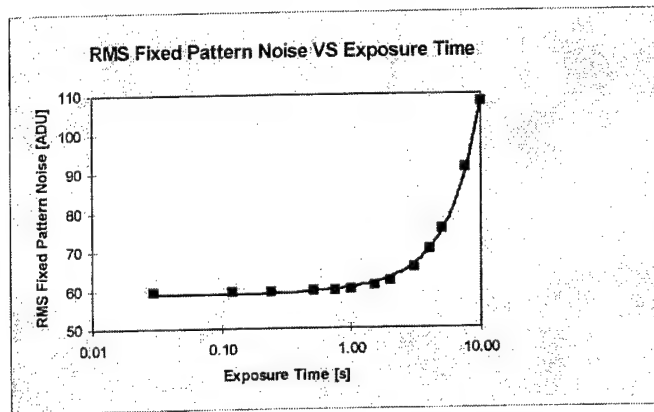**Figure 3.2** - S_{FLOOR} vs. f, N_{avg}=16, t_e=2 s.

Figure 3.3 - S_{FPN} vs. t_e, N_{avg}=16, f=2.5MHz
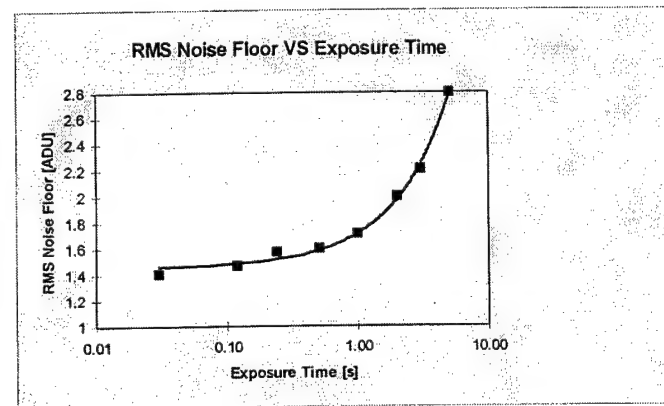

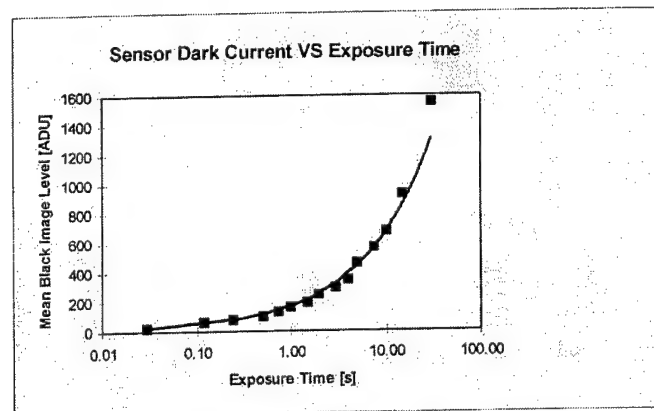**Figure 3.4** - S_{FLOOR} vs. t_e, N_{avg}=16, f=2.5MHz

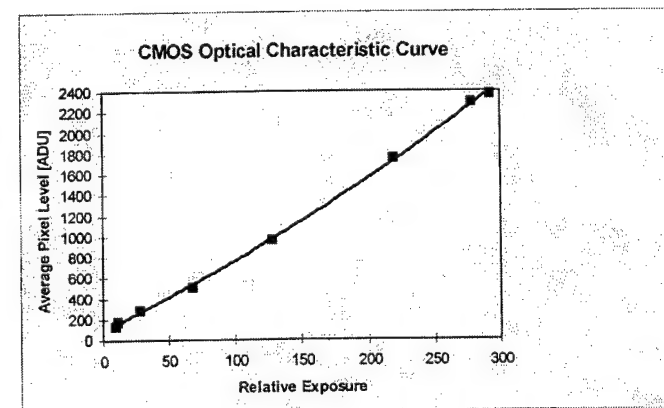**Figure 3.5** - S_{DARK} vs. t_e, N_{avg}=16, f=2.5MHz

Figure 3.6 - R_{exp}, N_{avg}=16, f=2.5MHz

Figure 3.7 - *SNR* vs. *f*, N_{avg}=16, t_e=2 s, the noise value used was calculated after subtraction of SFPN from the acquired image.

Figure 3.8 - *SNR* vs. t_e, N_{avg}=16, *f*=2.5MHz, the noise value used was calculated after subtraction of SFPN from the acquired image.
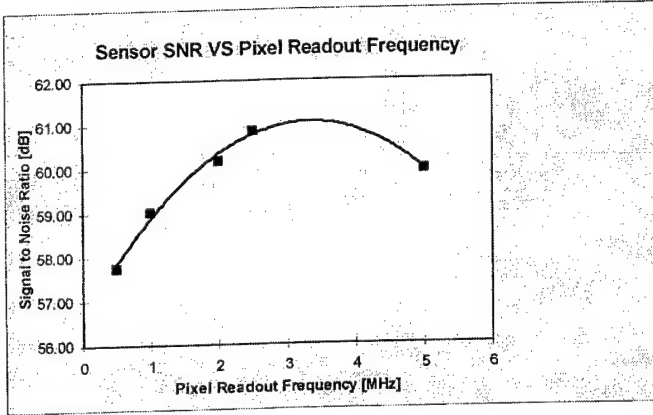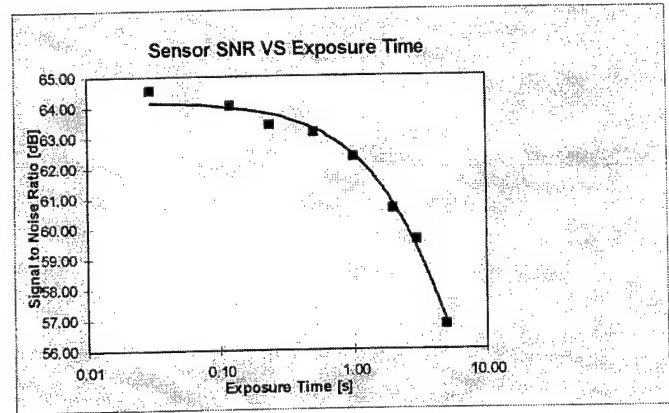
Figure 3.7 - *SNR* vs. *f*, N_{avg}=16, t_e=2 s, the noise value used was calculated after subtraction of SFPN from the acquired image. Figures 3.1 and 3.2 show the noise performance for both S_{FPN} and S_{FLOOR} with respect to the pixel readout frequency. From our measurements, the prototype imager exhibited better performance with readout frequencies in the range of 2-3MHz. This occurs since the overall leakage current at each pixel increases, hence increasing S_{FPN}, as the pixel waits to be read out. At 5MHz the on-chip high frequency clocking increased the overall noise. Note that S_{FLOOR} is considerably lower than S_{FPN} as expected from a CMOS image detector.

Figures 3.3 and 3.4 show S_{FPN} and S_{FLOOR} with respect to exposure time. As expected the noise levels rise with increasing exposure time, however at exposures of 2-3 seconds the overall noise only decreases approximately 4-5dB from the sensor's maximum SNR as shown in figure 3.8. After subtracting S_{FPN} from the image, the overall noise present is significantly reduced and allows SNR's in the range of 60dB for longer exposures (2-3 seconds) and high pixel readout rates (2-3MHz).

Figure 3.5 shows the overall average dark current level with respect to exposure time. With a maximum signal range of 2400 ADU's, this CMOS sensor exhibited a range reduction by a factor of 2 (1200 ADU's) at an exposure time of approximately 26 seconds. At exposure times of 2 seconds as used to acquire test images, the reduction of the available signal range was only 5 percent. Thus, the dark current level did not inhibit the image SNR considerably.

3.4 Acquired Images

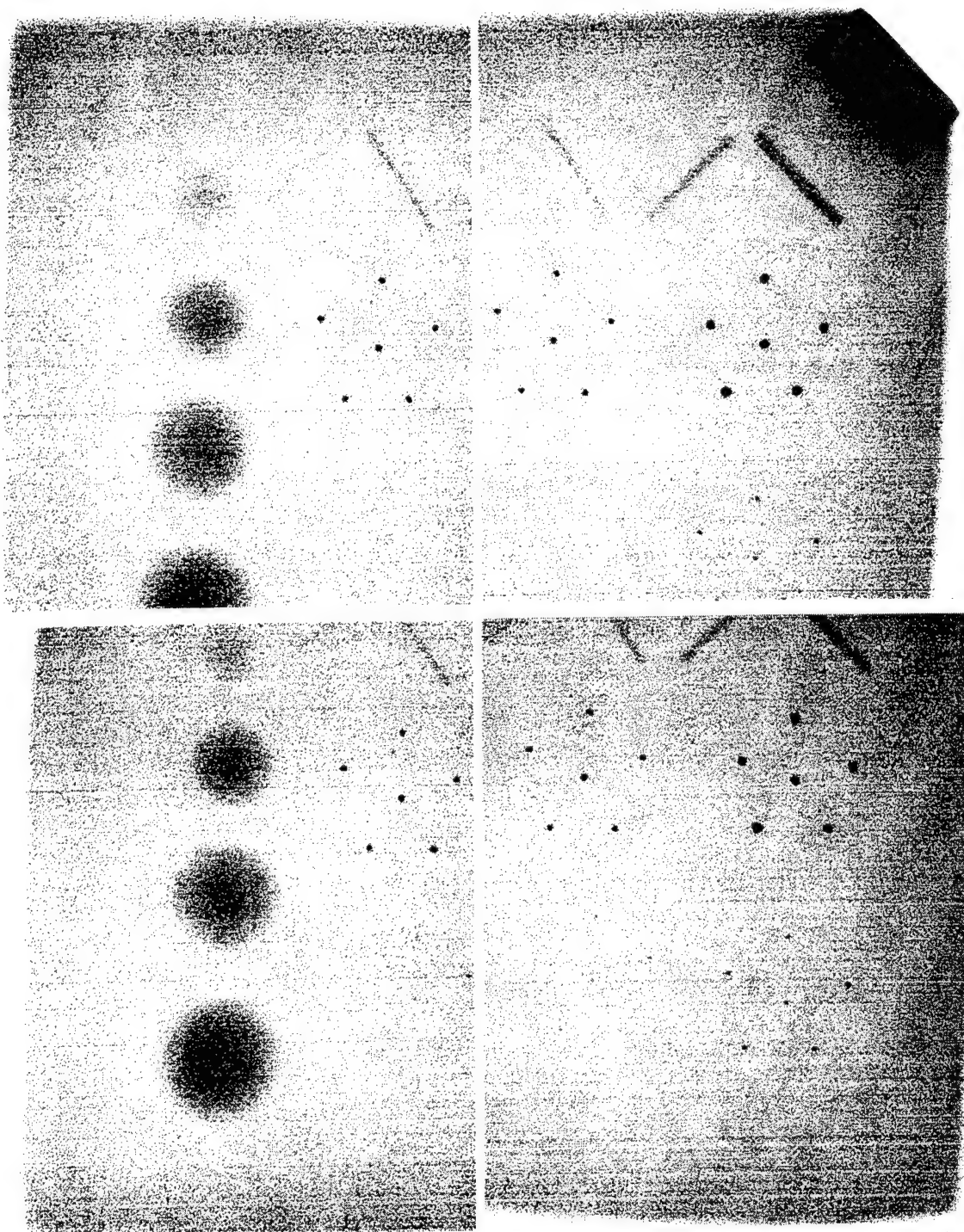Figure 3.9 - 4 separate images acquired of a digital mammography phantom. The position of the phantom was translated to cover its full area. There are 4 large circular masses with varying sizes (left side of phantom), 4 clusters of structures representing microcalcifications, each cluster contains 6 structures in a star pattern, and 4 bar structures (top of phantom) at alternating 45 degree angles.
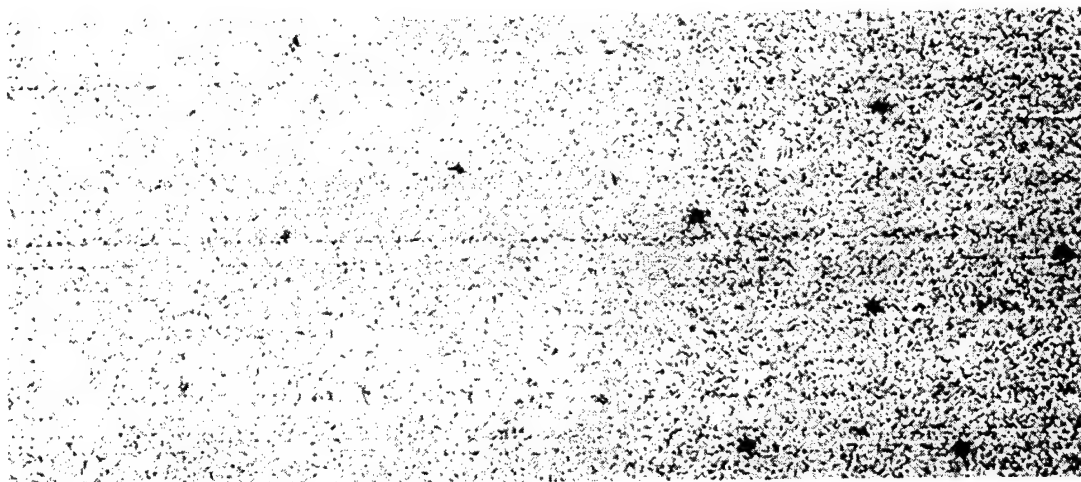
Figure 3.10 - Magnified view of the bottom right image in figure 3.9. This view shows the smallest microcalcification structures in the phantom. The structures on the right represent 200um structures and are clearly visible, however the 100um structures on the right are not all visible.
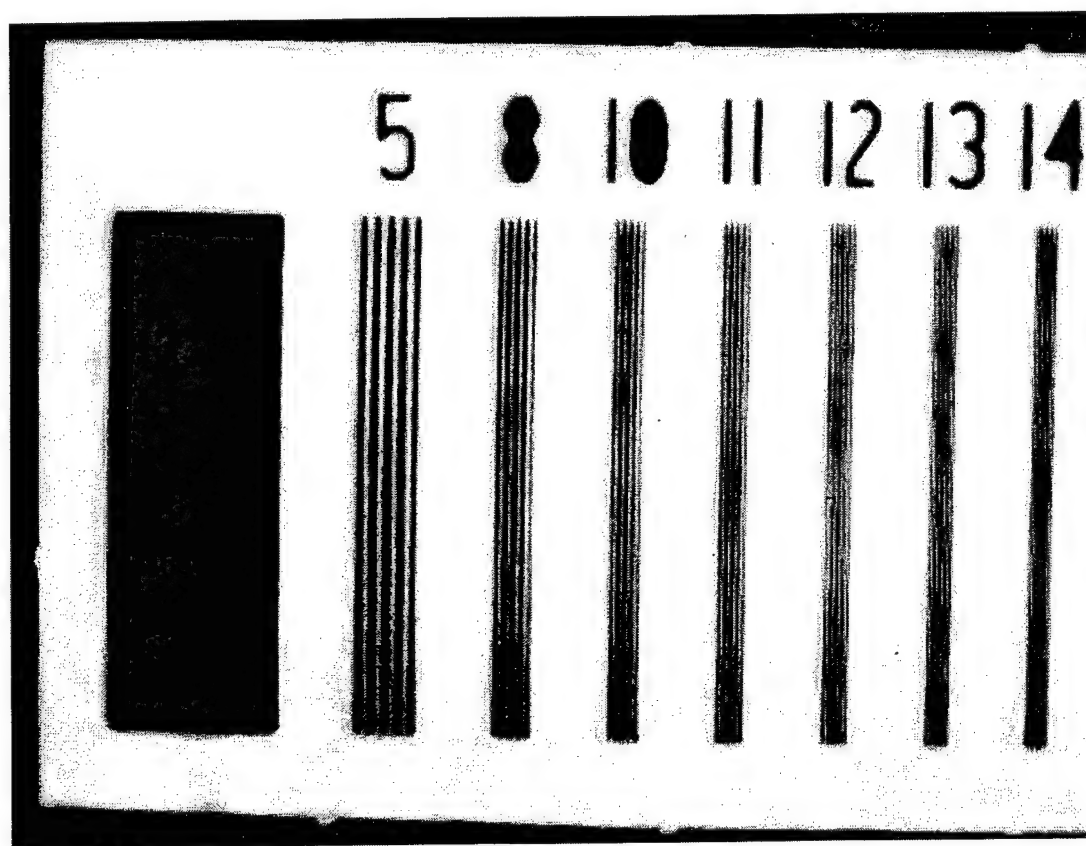

Figure 3.11 - This image shows the resolution obtained with a standard X-ray resolution bar pattern. The numbers at the top represent resolution in line-pairs per mm.

4. ESTIMATION OF POWER AND COST FOR MEDICAL APPICATIONS

The total power required for a CMOS based imager is inherently low due to the nature of CMOS semiconductor devices. The main sources of power consumption for the system includes the CMOS sensor, analog-to-digital (A/D) converter, and timing signal generator. The VV5850 sensor does not contain an on-chip A/D converter or timing signal generator so external devices were used. A 12-bit, 5MSPS (million samples per second) A/D converter was used for quantization and required 125 mW of power. The timing signal generator was a programmable logic device that required approximately 400mW of power while the VV5850 CMOS sensor drew approximately 125mW. Additional support circuitry consumed another 100mW for a total measured power consumption of approximately 750mW for the prototype imager. At this projected single sensor power consumption a CMOS imager based on a mosaic array of sensors (3x3) with an effective imaging area of 13 x 10 cm^2 would require power as shown below:

Device	Quantity	Power Consumption
Timing signal generator	1	0.4W
VV5850 CMOS image sensor	9	1.125W
12 bit, 5MSps A/D converter	9	1.125W
Other external support circuitry	9	0.9W
Total power consumption		~ 3.5W

The overall cost of the imager including electronics, lens, and phosphor screen was approximately $500. At this projected cost a CMOS imager based on a 3x3 mosaic would be less than $5000 US. The following list summarizes the projected cost and power consumption in comparison to a 3x3 mosaic CCD based imager[4]:

Cost and Power Consumption Comparison For 3x3 CMOS and CCD Based Sensor Mosaic Imagers (3000x2400 pixels)

	CMOS	CCD
Power	3.5Watts	30Watts
Cost	$5000	$25000

5. CONCLUSIONS

For digital radiography applications requiring low power and cost, CMOS image sensors show promising results in terms of feasibility. The resulting signal-to-noise ratio obtained for the particular CMOS detector used was approximately 60dB (10 bits) for longer exposures (2-3 seconds). The images acquired from a digital mammography phantom show that CMOS sensors may be used to obtain radiographic information. Future work should concentrate on increasing the light gathering capability of the system by optimizing the lens and phosphor screen. Also, the application of a micro-lens array at the CMOS sensor pixels would allow considerably more light to be gathered by each pixel since the pixel fill factor would be effectively increased.

Further reduction in cost and power consumption may be achieved by integrating all necessary support circuitry for the CMOS sensor on-chip. An A/D converter and specialized timing generator located on-chip would be a significant benefit for any portable applications not only in terms of low power and cost but minimization in terms of size and complexity of the imager.

ACKNOWLEDGMENTS

REFERENCES

1. Boyd Fowler, Abbas El Gamal, David Yang, and Hui Tian, "A Method for Estimating Quantum Efficiency for CMOS Image Sensors", Proceedings of SPIE, (San Jose, CA), January 1998.
2. Abbas El Gamal, Boyd Fowler, Hao Min, and Xinqiao Liu, "Modeling and Estimation of FPN Components in CMOS Image Sensors", *Proceedings of SPIE*, (San Jose, CA), January 1998.
3. A.D.A. Maidment and M. J. Yaffe, "Analysis of Signal Propagation In Optically-Coupled Detectors For Digital Mammography: II. Lens and Fibre Optics", *Physics in Medicine and Biology,* vol. 41, pp. 475-493, 1996.
4. Scott T. Smith, Hyunkeun Kim, Vivek Swarnakar, Myoungki Jeong, and Darold C. Wobschall, "Parallel Hardware Architecture for CCD-Mosaic Digital Mammography", *SPIE Medical Imaging*, vol. 3335, pp. 673-664, 1998.
5. G. C. Holst, "CCD Arrays, Cameras, and Displays", *JCD Publishing and SPIE Optical Engineering Press*, 1996.
6. VLSI Vision Lmtd., "VV5850 Monochrome High Resolution CMOS Image Sensor Datasheet", *VLSI Vision Lmtd*, 1998.
7. G. Yang, O. Yadid-Pecht, C. Wrigley, and B. Pain, "A Snap-Shot CMOS Active Pixel Imager for Low-Noise, High Speed Imaging", *Electron Devices Meeting 1998*, Session 2, Paper 7, Dec. 1998.
8. J. A. Seibert, J. M. Boone, and Karen K. Lindfors, "Flat-field Correction Technique for Digital Detectors", SPIE Medical Imaging 1998, vol. 3336, pp. 348-354, 1998.

[*] Author contact information at Sensor Plus [SS,DW] and SUNY at Buffalo [DB]:

Scott Smith:	E-Mail:	ssmith@sensorplus.com	X-ray Imaging Researcher	Tel: 1-716-831-0091 Fax: 1-716-831-0212
Darold Wobschall:		spadmin@sensorplus.com	Vice President of Technology	
Dan Bednarek:		bednarek@acsu.buffalo.edu	Medical Radiation Physicist	Tel: 1-716-898-4193 Fax: 1-716-898-5217

Effect of the reconstruction technique on the quality of digital mosaic mammograms

V. Swarnakar, M. Jeong, S. Smith and H. Kim D. Wobschall.

Sensor Plus, Amherst, NY, 14226

Digital mosaic imaging techniques provide a cost effective means to acquiring high resolution images. Constrained mosaic imaging techniques make use of special purpose fiducial patterns in order to define a-priori the relation between images on each tile. This "inter-tile" relation is applied to any images acquired subsequently. A simulation study was carried out where a model of the digital mosaic imager was used. By doing so, it was possible to compare the original data to that reconstructed using different techniques. The effects of these techniques on the quality of the final digital mosaic image were investigated. The techniques were applied towards reconstructing mammogram images. In order to evaluate performance of the approach, a set of features of interest were selected to measure image quality. Features that are important to visual perception include micro-calcifications and other fine details on the image, as per a radiologist's suggestion. Features important to the computerized diagnostic software include, edge maps and other common features used in existing computerized mammogram analysis approaches. Results of this experimental study provide a better understanding of how mosaic reconstruction approaches affect the quality of the final image. The study is also helpful in defining the role that features of interest, be it from a visual perception or computer software point of view, play towards selecting the image reconstruction scheme better suited for digital mosaic mammography. [Acknowledg]

Keywords: Digital Mammography, Image Quality, Mosaic Image Reconstruction

1. INTRODUCTION

Some of the desired features for digital mammography systems are cost, high resolution and large field of acquisition. Digital X-ray images to sever as successful replacement for film must be aimed at satisfying these requirements. Two basic approaches are currently under investigation for digital mammography. The most commonly employed of the two is the one in which conventional mammograms are digitized. The second approach is a digital imaging approach, wherein the mammogram is acquired digitally, via the use of CCD sensors[2][3]. In this approach CCD sensors are employed to observe an "imprint" of the x-ray mammogram on a surface such as Amorphous Selenium [1].

Existing approaches for digital mosaic imaging can be divided into two groups: (1) constrained mosaic imaging (2) un-constrained mosaic imaging. In constrained imaging approaches, a-priori information such as location of custom designed fiducial markers or precise knowledge of the imaging geometry is required. Un-constrained imaging approaches use only the information available within each imaging tile. Both approaches introduce artifacts in the final reconstructed image. Quality of the final mosaic image depends on the approach chosen. For mammography applications, it is imperative that the approach used introduces no artifacts that may hinder the diagnostic value of the final image. Artifacts can be perceived visually or detected by computerized diagnosis schemes. Images with no visually perceptible artifacts may contain distortions that deteriorate performance of a computerized diagnostic software. Conversely, images suitable for computerized analysis may not have good visual diagnostic quality. Therefore it is important to define

parameters and thresholds by which the quality of the final mosaic image can remain valuable to both visual assessment and computerized diagnosis.

In this work the constrained mosaic imaging approach is investigated. Custom designed calibration screens were used to achieve a high degree of accuracy in the reconstruction. The next section presents a brief overview of the digital mosaic imager. Section 3 contains a description of the mammogram selection process. Three types of reconstruction techniques were implemented. Each technique was applied towards mosaic image reconstruction and qualitative analysis results are presented in section 4. Results obtained by analyzing a set of mammograms using the different reconstruction techniques are presented.

2. MOSAIC IMAGING

An illustration of the mosaic imaging procedure is shown in Figure 1. In this example four CCD sensors are placed in a matrix type architecture where adjacent sensors 'observe' an overlapping field of the image plane. The digital mosaic image is reconstructed by correcting any geometric distortions introduced by the optical components and subsequently stitching the corrected images. It should be noted that as there is overlap between the fields of view of each CCD sensor, the stitching step is required to eliminate redundancy. As this work is based upon using constrained mosaic imaging approach, a calibration screen is employed to aid the correction of distortions. Subsequent stitching of images is also facilitated due the use of the calibration screen. It can be noticed, as the results section will illustrate, that the correction scheme plays a critical role in the final quality of the mosaic image.
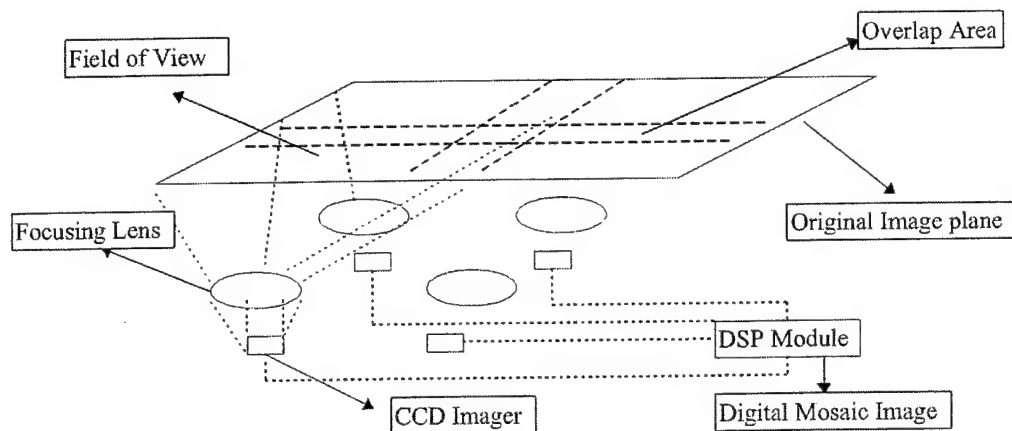

Figure 1. Model for the mosaic imager.

2.1 Distortion Correction

Several approaches have been proposed to correct distortions introduced by optical components of an imaging system[4]. One family of such approaches is based upon the use of a calibration pattern containing fiducial markers. The geometric relationship between the fiducial markers is known a-priori. Therefore an inverse transformation can be computed to relate pixel coordinates of the fiducials in the acquired image to the original pattern. Another approach is to develop a mathematical model of the optical components and use this model to recover the original pattern. This later approach has limitations when the underlying optical components can undergo changes as a function of time. Furthermore in the case of mosaic imaging, several such components are used and modeling each component individually can be an expensive task. In this work the former approach is used.

Throughout the following, I represents an image, the subscript index k represents the kth CCD and the superscript letters are r : for reference image (in the image plane), d : for digitized image and c: for corrected image. Let I_k^r be defined as a part of the original image, corresponding to the image area within the field of view of the kth CCD in the image plane. Also let I_k^d represent I_k^r once it is digitized by the CCD imager. In earlier work an approach based upon using piece-wise linear approximation was described in detail[2]. In this work two additional approaches are used. A new calibration patern has been developed to aid in improving the accuracy of the distortion correction stage. Let (x_i^d, y_i^d) be the coordinates of a fiducial marker in the digitized image. These markers can be mapped on the reference pattern I_k^r using the a-priori known geometric relation between the fiducials. Let (x_i^r, y_i^r) be the coordinates of the associated fiducial in the reference pattern I_k^r. Given a set of such fiducials with their coordinates in the digitzed image and their associated fiducials with coordinate values as mapped onto the reference image, a pair of transformations T_x and T_y can be defined such that

$$x_i^r = T_x(x_i^d) \quad and \quad y_i^r = T_y(y_i^d). \tag{1}$$

Where the functions T_x and T_y model the distortion introduced by the imager. In this work *Bilinear* interpolation and *Spline* interpolation are used to model the distortion functions T_x and T_y. Using the interpolating functions the coordinates of any pixel in the digitized image I_k^d can be associated to a point on the reference pattern. The images I_k^c obtained by applying the functions T_x and T_y are an approximation to the original calibration pattern I_k^r. In Figure 2. the acquired images of the calibration pattern used in this work are shown. The intersection points of each line and the lines themselves are considered fiducials. The geometry of the pattern is well defined so that it is fairly straight forward to identify those sections that are overlapping in each image. Figure 3. shows the reconstructed image after each of the small images of Figure 2 have been corrected using spline interpolation approach and subsequently stitched as described below.
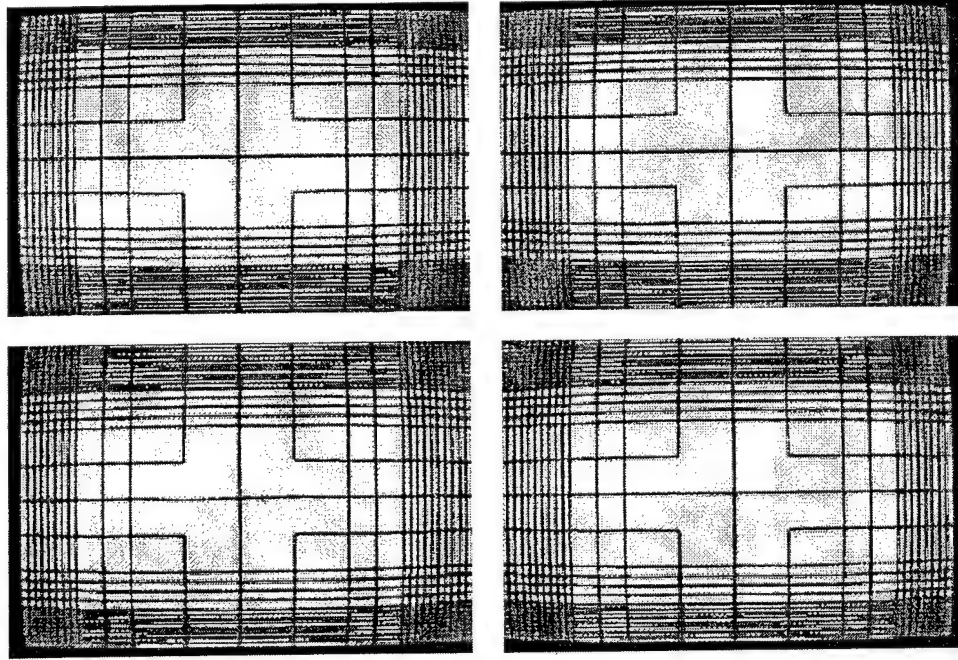

Figure 2. Images of the calibration pattern as acquire by each CCD sensor.
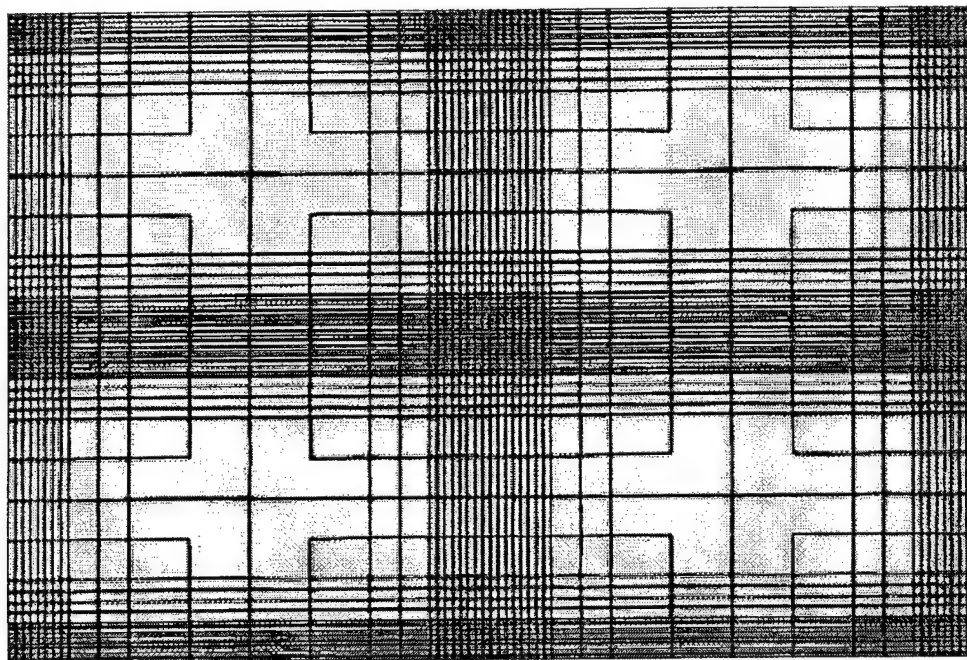
Figure 3. Mosaic image reconstructed using the spline interpolation algorithm.

It should be noted that the piece-wise linear approach uses only four fiducials during a step, while the bilinear and spline approaches are applicable to any number of fiducials. Thereby the piece-wise linear approach is a localized correction scheme while the bilinear and spline approaches are global correction schemes.

2.2 Stitching

Once the digitized images have been corrected the next step is to stitch these to form a mosaic. One way of stitching is to use an energy minimization approach to find the best matching coordinates of two images. This approach requires additional interpolation of the pixel values. This methodology is difficult to be used effectively when the underlying image has undergone a non-linear distortion. An alternative is to use the geometry of the calibration pattern. It is fairly simple to identify that section of an image that belongs to the overlap area. Therefore by extracting the part of the corrected image that does not fall in the overlap area and placing these in adjacent tiles a stitched image can be obtained. This approach avoids additional interpolation of the corrected image. However if adjacent tile images include effects of large angle rotation, this simplified stitching cannot be carried out accurately. In this work this later approach is chosen under the assumption that there are no large angle rotations in the digitized images. Then an approximation to the original image I^0 on the image plane is given by:

$$I^o = \mathbf{U}(I_k^c) \tag{2}$$

3. MAMMOGRAM SELECTION

Once a reconstructed image is available the next step is to evaluate the quality of the reconstruction. This issue is directly related to the case when acquiring images of mammograms. In practice though, the original image is unknown and only the reconstructed image is available. In order to properly study the effects of the reconstruction technique, the original image is also required. In this work a series of mammograms were digitally distorted and then stitched in order to carry out qualitative analysis. This process is described in the Section 4.

Quality of the reconstructed images can evaluated numerically and visually. Furthermore this evaluation can be carried out by observing the entire image, or some selected features of interest from the image. A variety of features of interest can be chosen from a mammogram. After consulting with the radiological experts involved it was decided that for this work three types of features would be investigated:

- Circumscribed mass
- Spiculated mass
- Micro-calcification.

A set of mammograms were selected from the Mammographic Image Analysis Society database. This is a publicly available database[7]. The images chosen here were all of size 1024x1024 and with a 200 micrometers pixel size resolution. The types of masses investigated are listed in the table below.

Feature	Tissue Type	Radius
Circumscribed Mass	Fatty.	29 pixels
Spiculated Mass	Fatty Glandular	53 pixels
Microcalcification-A.	Dense	25 pixels
Microcalcification-B.	Dense	8 pixels.

Table I. Types of features of interest from the mammograms.

Next section contains analysis results for three mammograms. The radius of the area surrounding each feature of interest in these mammograms is also listed in the table above. Areas with micro-calcification were from the same image.

4. RESULTS

Results presented here simulate a system where four CCD sensors are used to create the digital mosaic. By simulation it is understood that a mathematical model of the individual imaging components was employed instead of building the system.

The overlap area of four tiles is where the most severe distortions are expected to occur. In order to evaluate the quality of the reconstructed features, each mammogram was translated and placed in a larger image such that the feature of interest falls on the overlap region of all four tiles. So the mammograms are centered in a larger image using the center coordinates of the feature of interest as the center point of the larger image. The size of the large image is 1497x969 pixels and it is the same as that of the calibration pattern. Next four overlapping subsections of size 768x512 are extracted from the large image. Note that the resolution of the CCD's used in the imager is also 768x512 pixels. This will enable the application of the imagers distortion function to the mammogram images. It should be note that each sub-image undergoes a slightly different transformation. The distortion function used was based upon a Barrel Distortion model. As it can be observed from the images in Figure 2 and 3 this function is suitable to approximate the imager optics. Once each sub-image is distorted using the distortion function the three correction schemes, Piece-wise linear approximation, Bilinear interpolation and Spline interpolation were applied to correct each sub-image. Sections from the corrected sub-images that do not belong to the overlap area are extracted and then placed

together to form the reconstructed mosaic. The sections that do not fall in the overlap area were of size 729x485 pixels. Consequently the reconstructed image is the same size as the initial large mammogram image.

4.1 Quantitative analysis

One way of examining the reconstruction quality is to compute numerical measures of disparity between the original image and the reconstructed image. In this work, three measures, namely the Mean Absolute Error (MAE), the Mean Squared Error (MSE) and the Cross Correlation coefficient were used[5]. Given two images I_1 and I_2 of some size NxM the above quantities can be defined below.

Mean Absolue Error (MAE) :

$$MAE(I_1, I_2) = 1/N * M \sum_{i,j} |I_1(i,j) - I_2(i,j)| \qquad (3)$$

Mean Square Error (MSE):

$$MSE(I_1, I_2) = 1/N * M \sum_{i,j} (I_1(i,j) - I_2(i,j)|)^2 \qquad (4)$$

Cross Correlation Coefficient:

$$\rho = \frac{\sigma_{12}}{\sigma_1 \sigma_2} \qquad (5)$$

Where in equation (5) above, σ_1, σ_2 are the variances of the images I_1 and I_2 and σ_{12} is the joint variance of these images. The correlation coefficient measures the disparity in between the two images globally. Whereas the MAE and MSE estimators provide an average estimate of the local behavior of the two images. Initially all these measures were computed using the entire large mammogram image. The results are shown in Table II. below. In general it was observed that the Bilinear interpolation based method performed better than the other two.

Mean Absolute Error			
Feature	Piece-wise Linear	Bilinear	Spline
Circumscribed Mass	1.19	0.78	1.09
Spiculated Mass	0.72	0.49	0.70
Microcalcification-A.	0.67	0.43	0.55

Mean Squared Error			
Feature	Piece-wise Linear	Bilinear	Spline
Circumscribed Mass	31.72	27.76	17.15
Spiculated Mass	35.09	26.88	29.13
Microcalcification-A.	26.25	19.22	15.01

Cross Correlation Coefficient			
Feature	Piece-wise Linear	Bilinear	Spline
Circumscribed Mass	0.9969	0.9973	0.9974
Spiculated Mass	0.9945	0.9958	0.9954
Microcalcification-A.	0.9956	0.9968	0.9975

Table II. Quantitative results computed on the entire reconstructed image.

Next these disparity measures were applied to sub-sections of the reconstructed image where the features of interest were located. Sections of size 128x128 were extracted from the central part of the reconstructed image. This is the region where the four tiles overlap and where the maximum distortion is expected to occur. Results obtained for these images are shown in the table below. From these tables it can be observed that again bilinear interpolation provided the best and most consistent results.

Mean Absolute Error			
Feature	Piece-wise Linear	Bilinear	Spline
Circumscribed Mass	1.48	1.08	1.16
Spiculated Mass	1.44	1.09	1.55
Microcalcification-A.	1.33	1.05	1.11
Microcalcification-B.	1.36	1.19	1.97

Mean Squared Error			
Feature	Piece-wise Linear	Bilinear	Spline
Circumscribed Mass	4.70	2.58	2.97
Spiculated Mass	3.96	2.37	2.66
Microcalcification-A.	3.55	2.26	2.53
Microcalcification-B.	3.79	2.99	8.85

Cross Correlation Coefficient			
Feature	Piece-wise Linear	Bilinear	Spline
Circumscribed Mass	0.9989	0.9994	0.9993
Spiculated Mass	0.9957	0.9974	0.9971
Microcalcification-A.	0.9952	0.9969	0.9965
Microcalcification-B.	0.9923	0.9939	0.9821

Table III. Quantitative results computed regions with features of interest.

4.2 Visual Analysis

Visual assessment of the image quality is a subjective task. Nevertheless an experienced observer can successfully identify any anomalies introduced by the reconstruction procedure. Visual evaluation of the large images revealed that when observing these images with zoom factors of up-to four times, no significant distortions were noticed. In general, the Spline based approach provided the most "visually pleasing" results. Similar observation was made when visually observing the regions with features. In Figures 3-A,B,C,D a series of images of the areas with features of interest are shown. These images were enhanced using the *un-sharp* filtering operation [6].
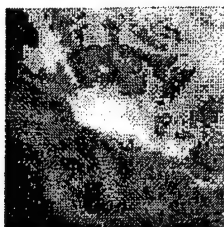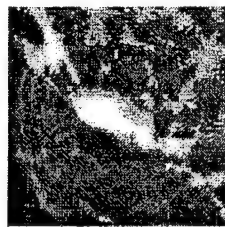
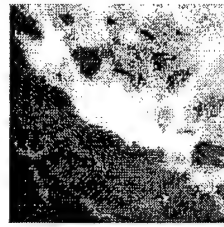*Original*   *Piece-wise Linear*   *Bilinear*   *Spline*
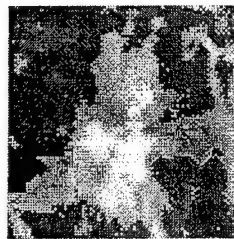

Figure 3-A. Circumscribed Mass.

Original   *Piece-wise Linear*   *Bilinear*   *Spline*
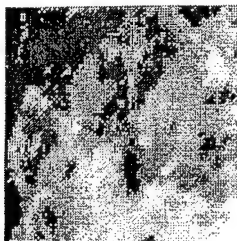

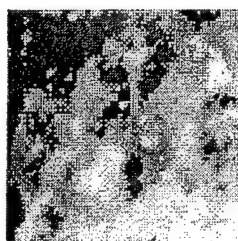**Figure 3-B.** Spiculated mass

Original   *Piece-wise Linear*   *Bilinear*   *Spline*
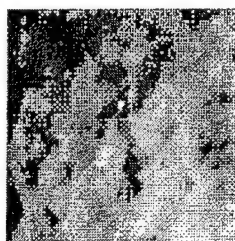

Figure 3-C. Micro-calcification A.

Original   *Piece-wise Linear*   *Bilinear*   *Spline*

Figure 3-D. Micro-calcification B.

As it can be observed the differences between each reconstruction scheme are better viewed under such a transformation. However, this operation is usually applied to images prior to using a computerized analysis algorithm. Therefore the effects of these differences will reflect in the performance of the computer algorithm. A simple edge enhancement and detection routine is applied to the filtered images. Results from this operation are shown in Figures 4-A,B,C and D.
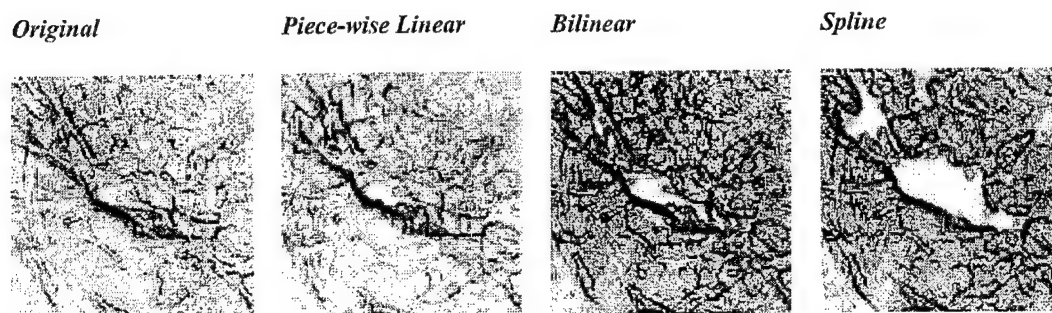
Original *Piece-wise Linear* *Bilinear* *Spline*

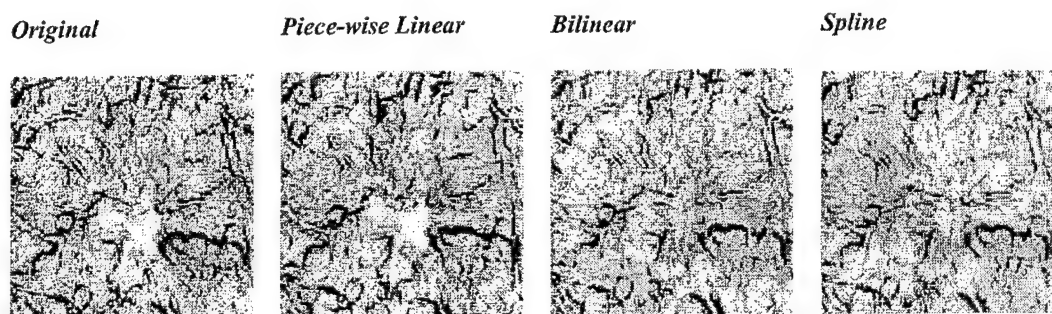**Figure 4-A.** Circumscribed Mass.

Original *Piece-wise Linear* *Bilinear* *Spline*

Figure 4-B. Spiculated mass

Original *Piece-wise Linear* *Bilinear* *Spline*

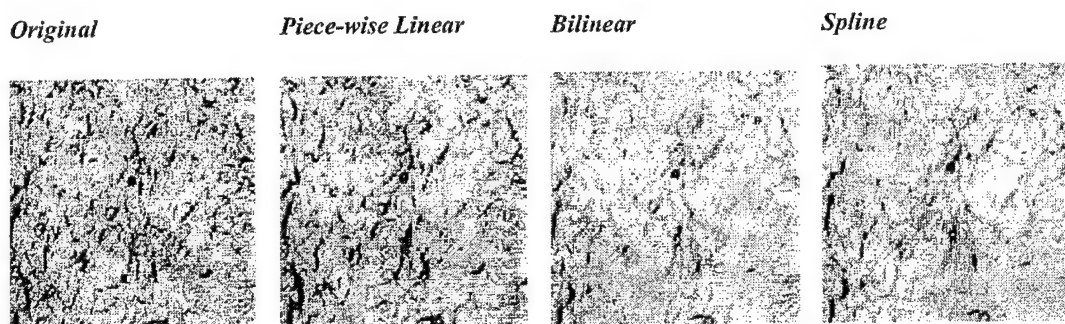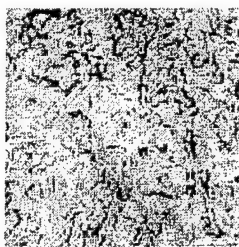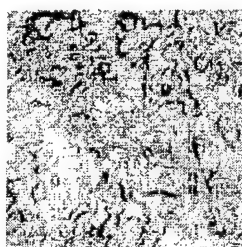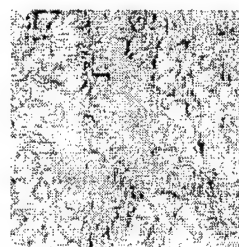**Figure 4-C.** Micro-calcification A.

Original   *Piece-wise Linear*   *Bilinear*   *Spline*

Figure 4-D. Micro-calcification B.

As it is clear the computer algorithm's performance is significantly different for each of the images analyzed. When observing the smaller feature images, visually it can be argued that the spline interpolation approach provided the most accurate results. However, the edge enhancement algorithm was least influenced when the images were reconstructed using the piece-wise linear scheme. Some artifacts can be noticed in the piece-wise linear approach. It can also be assumed that the artifacts introduced are related to the calibration pattern employed. A different calibration pattern will introduce different types of artifacts. Regardless of the technique used to reconstruct the images, it should be noted that small details such as micro-calcifications were still visible in the mosaic reconstructed image. The overall ability to

CONCLUSIONS

The primary objective of this work was to present the effect different reconstruction schemes have on the quality of the digital mosaic mammograms. Using the constrained mosaic imaging approach three different reconstruction schemes were investigated. Numerical and visual evaluation of the effects of these approaches were presented. Numerical evaluation results can support that the bilinear interpolation scheme provides the most consistent results regardless of the type of features present in the mammogram. Visual evaluation on the other hand indicated that spline reconstruction provides the most accurate reconstruction. Lastly, when using a simple computer algorithm on regions with features of interest it was observed that the piece-wise linear approximation method influenced the performance. Based upon these observation it can be stated that as long as visual or numerical quality evaluation is the criteria, bilinear interpolation will provide the most consistent results. However, when considering application of computer algorithm to these images further investigation must be carried out.

REFERENCES

1. J. A. Rowlands, D. M. Hunter, and N. Araj, "X-Ray Imaging Using Amorphous Selenium: A photoinduced discharge readout method for digital mammography", Med. Phys., Vol. 18, pp. 421-431, 1991.
2. V. Swarnakar, M. Jeong, R. Wassermann, E. Andres and D. Wobschall, "Integrated An Integrated Distortion Correction and Reconstruction Technique for Digital Mosaic Mammography", *V. Swarnakar, M. Jeong, R. Wasserman, E. Andres, D. Wobschall,* Proceedings Medical Imaging 97.
3. A. Jalink, J. McAdoo, G. Halama and H. Liu, "CCD Mosaic Technique for Large-Field Digital Mammography", IEEE Trans. on Medical Imaging, Vol. 15, No. 3, June 1996.
4. D. A. Butler and P. K. Person, "A Distortion-Correction Scheme for Industrial Machine-Vision Applications", IEEE Trans. on Robotics and Automation, Vol. 7, No. 4, Aug. 1991 pp. 546-551.
5. R. Salvi, "Introduction to Applied Statistical Signal Analysis", IRWIN 1991.
6. A. K. Jain, "Fundamentals of Digital Image Processing", Prentice Hall 1989.
7. MIAS Database: http://skye.icr.ac.uk/miasdb/miasdb.html.

Parallel hardware architecture for CCD-mosaic digital mammography

Scott T. Smith, Hyunkeun Kim, Vivek Swarnakar, Myoungki Jeong,
and Darold C. Wobschall

Sensor Plus Inc., 4250 Ridge Lea Rd., Amherst, NY 14226

ABSTRACT

The development of an efficient parallel hardware architecture suitable for CCD-mosaic digital mammography has been accomplished. This paper presents this architecture including both the analog and digital portions of the imaging hardware. A two dimensional array of CCD sensors are used to capture the mammographic image synchronously and simultaneously. Each CCD's analog signal is converted to a 12 bits/pixel digital value through an array of high speed analog-to-digital converters. A parallel array of mesh connected TMS320C40 DSP processors then takes in the digital image data simultaneously. The DSP's are used to precisely register the mosaic of individual images to form the final large format digital mammogram. Also, they are used to control CCD characteristics and parallel data transport to the viewing workstation. One master DSP is located on the workstation's PCI bus which controls the parallel DSP array and collects compressed image data through a 60MB/s port. Since all computations are performed in parallel using local memory on each DSP, the overall acquisition, image registration, and transmission to display of the final mammogram is performed in less than 30 seconds. This allows the physician to perform a preliminary observation of the patient's mammogram.

Keywords: CCD-mosaic, parallel processing, digital mammography, DSP processors, digital imaging, image processing hardware, image registration, medical imaging

1. INTRODUCTION

Current research in the area of digital mammography addresses feasibility and reliability compared to standard film-based approaches. Specific areas of concern for digital mammography research include the following[1,2]:

- Physics of new detectors and X-ray conversion devices
- Resolution and precision issues associated with the sensors and acquisition of X-ray images
- Automated and assisted microcalcification detection methods based on digital processing techniques
- Electronic imaging methodologies for the capture of large format images
- Transmission and storage of digital mammograms for telemammography and medical archive databases

The realization of efficient digital mammography depends on the integration of all these areas into real systems. The discussion of actual hardware systems for efficient acquisition and manipulation of digital mammograms brings closer this realization. The research presented in this paper defines a mosaic imaging hardware architecture in an attempt to create a platform for efficient testing of each aspect involved with the development of digital mammography.

Previous research for large format imaging methods for mammography include the following[1]:

- Slot-scanned
- Area-scanned
- Scanning Laser Stimulated Luminescence
- Large flat panel X-ray detectors (Silicon and Selenium)
- Fiber-coupled CCD arrays

The imaging methodology developed for this research is based on a two-dimensional array of charge-coupled devices (CCD's) and lenses to achieve large format acquisition[3]. This technique is similar to the area-scan method however no mechanical scanning is required since the CCD-mosaic area employed covers the entire image plane[4]. The following diagram demonstrates this method:
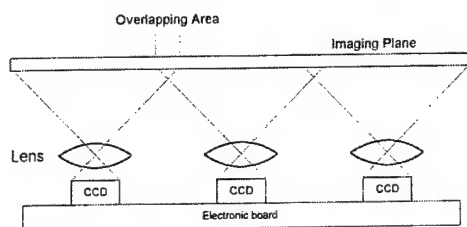

Figure 1: Lens coupling of image plane and CCD devices

This imaging method requires lens distortion correction and image reconstruction to form the final continuous image [2]. The hardware presented here is based on the computational needs of this imaging method however alternative reconstruction techniques may be implemented simply using high level programming languages.

2. SCALEABLE CCD-MOSAIC HARDWARE METHODOLOGY

The effectiveness of mosaic imaging using multiple CCD's, in terms of a general architecture that may be applied to any large format digital imaging application, depends on the ability to independently scale the size of the CCD mosaic and the size of the parallel digital processing electronics. Thus, a mosaic imaging system should allow general scaleability regardless of the imaging speed, resolution, and image registration needs. To achieve such a generality, a connection methodology based on three electronic layers will be proposed which effectively de-couples the CCD electronic mosaic from the parallel processing architecture[10].

The three layers for this hardware architecture as shown in figure 2 below. Two separate interconnection networks (IN) are needed to connect each hardware layer. Layer 1 is defined as the CCD layer, 2 is the analog processor (AP) layer, and 3 is the digital processor element (PE) layer. Since the CCD layer output and AP layer input are analog, an analog IN is required for their connection. The output of the AP layer 1 and the input of the PE layer are digital requiring a digital switching network for connection. Both analog and digital IN's may be combined to connect independent hardware layers to form an efficient hardware architecture. To ensure the correct operation of the connected layers, the bandwidth of each layer must satisfy equation 1.
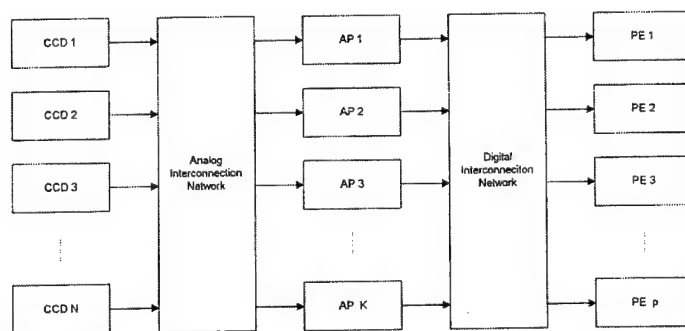

Figure 2: Modular mosaic system: Layer 1-CCD electronics, Layer 2-Analog processing electronics, Layer 3-digital processing electronics

$$N = \text{number of CCD's (hardware layer 1)}$$
$$K = \text{number of analog processors (hardware layer 2)}$$
$$p = \text{number of PE's (hardware layer 3)}$$
$$B_{ccd} = \text{Bandwidth of CCD's}$$
$$B_{AP} = \text{bandwidth of analog processors}$$
$$B_{PE} = \text{bandwidth of PE inputs}$$

$$N \cdot B_{ccd} \leq K \cdot B_{ap} \leq p \cdot B_{pe} \tag{1}$$

Following this methodology allows minimization of the number of AP's and PE's needed for the imager based on a given number of CCD's and the CCDs' pixel rate. This minimization is important for cost efficiency as well as physical size reduction. The interconnected layers allow any configuration of N CCD's with p PE's while keeping both N and p independent as long as the constraint equation 1 is satisfied.

Overall, this method of de-coupling the electronics of the imager allows the designer to easily form application specific mosaics by independently choosing the individual CCD's, the analog processing components, and digital processing elements. For example, the image reconstruction algorithms may need to be developed and tested on various types of programmable digital processors to achieve desired performance levels. The designer would be free to attach the CCD and AP layers to any parallel PE structure through the digital IN without redesigning layers 1 and 2.

3. PARALLEL HARDWARE ARCHITECTURE

3.1 Discussion of Noise

To achieve the desired dynamic range of 12 bits/pixel for the analog electronic layers, a noise model must be analyzed. A brief representation of the RMS equivalent noise floor of the CCD and AP electronics is shown below[5]:

CCD Dynamic Range

$$DR_{CCD} = \frac{V_{max}}{\langle V_{rms} \rangle} \tag{2}$$

DR_{CCD} is the maximum dynamic range of the CCD, V_{max} is the maximum voltage a pixel may have and occurs when a charge well becomes saturated, and $<V_{rms}>$ is the RMS noise floor of the CCD. The dynamic range of the CCD chosen limits the overall capability of the imaging system.

Analog Processor and Overall System Noise

Noise sources in the analog processing electronic system also contribute to the overall system noise. The system noise components are as follows:

1. Pre-Amplifier Noise, V_{pre}
2. Analog Multiplexer, V_{mux}
3. Correlated Double Sampler, V_{cds}
4. A/D Converter Noise, $V_{A/D}$
5. EMI (electromagnetic interference) from internal and external sources, V_{EMI}

Not all digital imagers will contain each of these noise sources, however all should be included for completeness. With these added, the overall system noise model becomes:

$$\langle V_{sys} \rangle = \sqrt{\langle V_{ccd}{}^2 \rangle + \langle V_{pre}{}^2 \rangle + \langle V_{cds}{}^2 \rangle + \langle V_{mux}{}^2 \rangle + \langle V_{A/D}{}^2 \rangle + \langle V_{EMI}{}^2 \rangle} \tag{3}$$

The most difficult noise source to characterize and eliminate is V_{EMI} which is dependent on the physical layout of the analog circuitry and the circuit's susceptibility to external and internal interference. Thus, when calculating the noise parameters of the analog front end, the V_{EMI} source is an unknown quantity that must be estimated to ensure that a specific SNR will be accomplished.

Overall, this method of noise analysis allows a particular SNR to be reached for any digital imager. This method was used for the determination of the dynamic range capability of the digital mammography system.

3.2 CCD Sensors

To achieve scientific quality imaging, the CCD sensor chosen is of primary concern. Characteristics of CCD's include noise parameters, pixel density or resolution, maximum pixel readout frequency, number of analog output buffers, spectral response, pixel size, and of course cost. The CCD chosen for the digital mammography device is the Kodak KAF-0400 full frame image sensor. A brief list of specifications is shown in the table below:

Table 1: Kodak KAF-0400 CCD Image Sensor

Parameter	Value	Units
Resolution	768 x 512	Pixels
Dynamic Range	8300	
Horizontal Transport Frequency (each output)	20	MHz
Vertical Transport Frequency (each output)	500	kHz
Output Buffers	1	
Pixel Dimensions	9 x 9	um^2
Quantum Efficiency (600-900nm)	30-40	%
Full-well Linear Capacity	85000	electrons
Cost (US)(Grade 0)	400	$

The spectral response of the KAF-0400 given in terms of quantum efficiency over a range of wavelengths is shown below [6]:

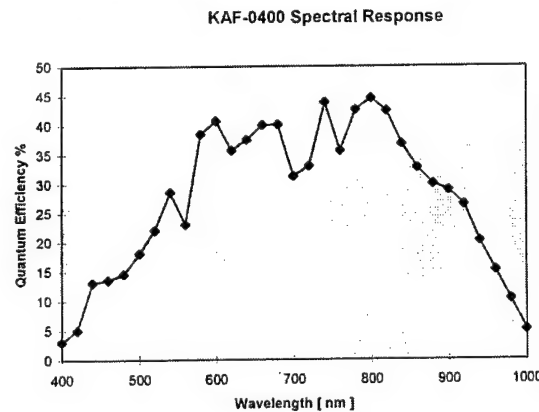**KAF-0400 Spectral Response**

Figure 3: Graph of quantum efficiency vs. wavelength of the Kodak KAF-0400 CCD

An overview of the advantages of this CCD may be summarized as follows:

- Capable dynamic range is 13 bits/pixel
- Quantum efficiency is high, particularly in 800nm infrared range
- Pixel size is 9um^2 which allows near field focusing of the X-ray conversion layer
- Pixel density is medium format, 768x512, which allows efficient lens coupling
- High speed full frame readout
- Cost is relatively inexpensive

A total of 72 CCD's are used in a 8x9 array for the full digital mammography device which forms a maximum image size of 6144x4608 pixels. The lens demagnification factor used is 5.5:1 such that each CCD pixel represents approximately 50um at the image plane. Thus, the total effective imaging area of the imager is 30.7cm x 23.0cm, this sufficiently covers the full field imaging area of standard mammography devices[1].

3.3 Analog Processing Hardware

The analog processor electronics consist of an array of correlated double samplers (CDS's) and 12 bit A/D converters. Currently each CCD channel contains one CDS and A/D converter operating at 2.5MHz pixel rate for testing purposes. However, the CDS is capable of operating at a maximum of 50MHz with 12 bit precision which will allow up to 20 CCD signals to be processed through a single CDS by multiplexing the signals. This multiplexing scheme will considerably increase efficiency in cost, power, and physical space for a production digital mammography device.

The CDS circuit effectively removes pixel reset noise from the CCD's analog signal and is of integral importance in the analog processing chain. Also, low frequency noise sources are suppressed with this hardware. The block diagram below demonstrates the CDS design:
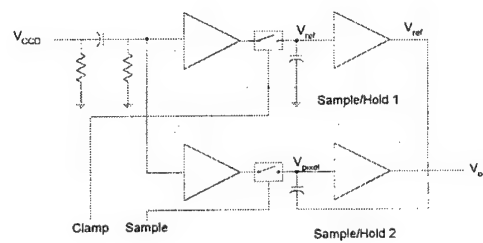

Figure 4: Circuit diagram of a typical correlated double sampler designed with sample and hold amplifiers

$$V_{out}\left(t_{sample}\right) = V_{CCD}\left(t_{sample}\right) - V_{CCD}\left(t_{clamp}\right) \tag{4}$$

Two separate high speed sample and hold (S/H) amplifiers are used to form the CDS [7]. The first S/H device samples the reset level of the current pixel and the second S/H samples the pixel voltage level while subtracting the reset level. Equation 4 above defines the output of the CDS circuit. The pixel rate of the mosaic imager is 2.5MHz and the A/D converter chosen has a maximum sample rate of 5MSPS [8]. Currently each CCD channel contains the following circuitry:
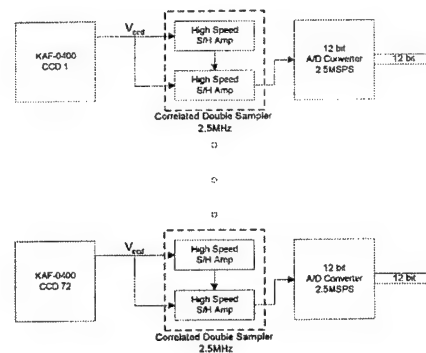

Figure 5: Analog Processor For Each CCD Channel

---

[1] Standard mammography format is 24cm x 18cm. The CCD-mosaic is larger than this format since overlap of image data of adjacent CCD's must be removed which will decrease the effective imaging area of the device to approximately match 24cm x 18cm.

The calculated system noise floor referred to the analog processor input is shown below [6,7,8]:

$$\left\langle V_{sys}\right\rangle = \sqrt{\left\langle V_{ccd}^{2}\right\rangle + \left\langle V_{cds}^{2}\right\rangle + \left\langle V_{A/D}^{2}\right\rangle} \qquad (5)$$

$$\left\langle V_{sys}\right\rangle = \sqrt{\left\langle V_{ccd}^{2}\right\rangle + 2\left(\left\langle V_{IR}^{2}\right\rangle + \left\langle V_{HM}^{2}\right\rangle\right) + \left\langle V_{A/D}^{2}\right\rangle} \qquad (6)$$

For An Ideal System

$$\left\langle V_{sys}\right\rangle \approx \sqrt{\left(130\mu V\right)^{2} + 2\left[\left(5.2\mu V\right)^{2} + \left(3.8\mu V\right)^{2}\right] + \left(20.7\mu V\right)^{2}} = 132\mu Vrms \qquad (7)$$

Maximum dynamic range @ 2.5MHz is:

$$DR_{sys} = \frac{V_{max}}{\left\langle V_{sys}\right\rangle} = \frac{0.850V}{132\times10^{-6}V} \approx 6439 \qquad (8)$$

$$DR_{sys}(bits) = \log_{2}\left(DR_{sys}\right) \approx 12.6bits \qquad (9)$$

Of course the 12 bit A/D converter limits the dynamic range to 12 bits in this ideal case. The ideal noise floor is not easily obtained due to external and internal noise sources plus noise caused by temperature variation in the CCD. Thus, the actual intensity resolution will be approximately 11-12 bits in the real system with this specified hardware.

3.4 Parallel DSP Hardware

The topology of the processing elements (PE's) determines the overall efficiency of the parallel machine in terms of its ability to carry out the computation of specific parallel tasks. Many parallel machines designed for image processing tasks employ varieties of mesh topologies since they resemble matrices whereby images are more naturally segmented among the PE's. The mesh topology was chosen to provide versatility for general parallel image processing. To maximize efficiency on standard image processing calculations, DSP processors are incorporated in the design as the basic PE module. The specific DSP employed is the Texas Instruments TMS320C40 parallel DSP [9]. The block diagram below shows the general architecture used to allow generic scaleability irrespective of the number of CCD's and DSP's in the mosaic:
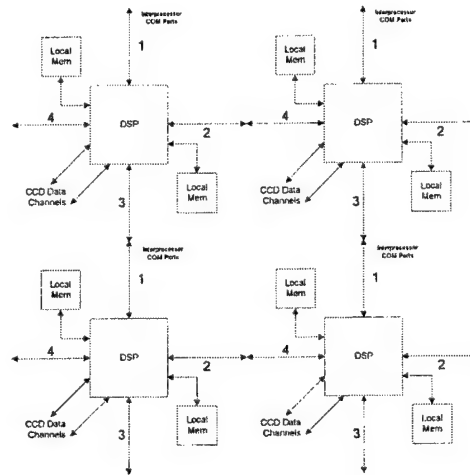

Figure 6: Example of multiple processor architecture using DSP's.

TMS320C40 DSP	
Instruction Cycle	33ns
32 Bit Floating Point Performance	60 MFLOPS
I/O Performance	384 MB/s
6 Bi-directional Communication Ports	20 MB/s each

Table 2: Characteristics of TMS320C40 DSP [9]

Note that the C40 contains 6 bi-directional communications ports which allow for interprocessor communications and digital I/O channels for CCD data inputs. Also, this DSP has a 6 channel DMA coprocessor directly linked to the COM ports to allow data I/O without CPU intervention. Four CCD's are connected to one DSP processor such that the total 8x9 CCD-mosaic requires a total of 18 DSP processors plus one master DSP. The following diagram shows the digital interconnection network and CCD mosaic interface designed for the digital mammography device:
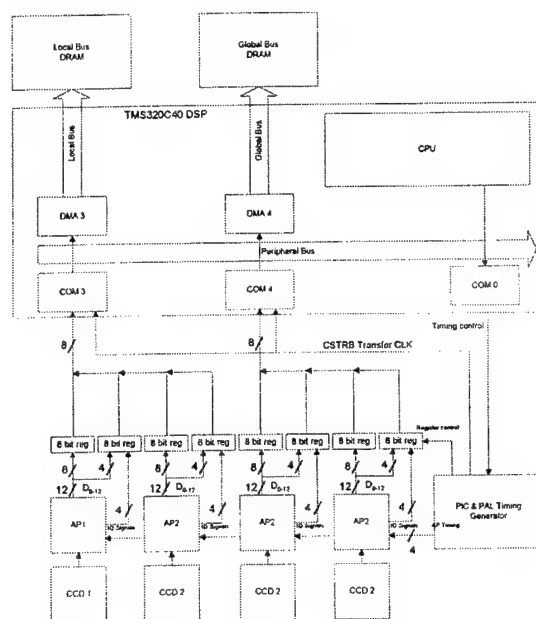
Figure 7 - Details of digital interconnection network between AP's and the DSP processor
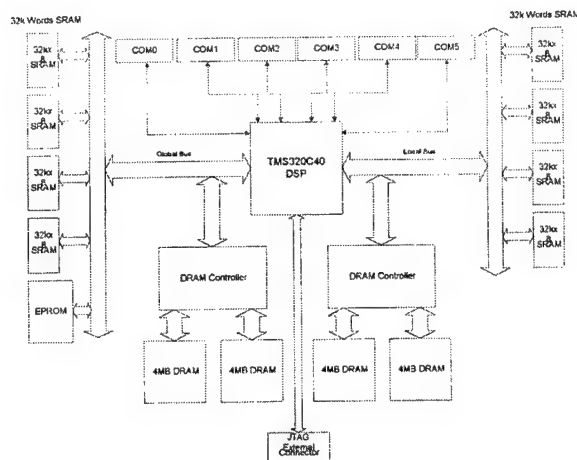

Figure 8 - Details of hardware architecture for DSP PE.

To test the performance of the parallel C40 architecture, a dual processor configuration was used. The memory architecture for each processor is a dual local structure. That is, each DSP contains two memory banks connected via two independent 32 bit data and address buses. The C40 is designed to perform two instructions per clock cycle on data arriving from both of its data buses, hence performance is significantly increased with dual memory banks. The decision to avoid a global memory bank accessible by each processor resulted from the looming bandwidth bottleneck problem associated with N processors connected to one memory. This design also uses single cycle accessible SRAM for program instruction storage and highly used data sections. This adds to performance since wait states are avoided for many data operations.

To test the overall time required to register the final image from the segmented image data, a method for geometrical lens distortion correction and segment stitching was ported to the C40 architecture [2]. The distortion correction algorithm operates sequentially on each of the four images acquired per DSP. The stitching of image segments is performed by transferring image data from each local DSP memory to a host workstation memory via the master DSP. We assume that every mosaic image has the same valid area that excludes overlapping areas (i.e., after distortion correction each image contains the same set of reference points used for stitching) otherwise a more complicated stitching method is necessary. The following results demonstrate the total time needed to acquire and fully register the 6000x4500 pixel mammogram.

4. SIMULATED RESULTS OF A 2x2 CCD-MOSAIC IMAGER

Digital mammography requires the following imaging constraints to ensure feasibility:

- 12 bits/pixel dynamic range and high light sensitivity CCD's
- 18cm x 24cm image plane
- 50um resolution at the image plane
- Very low geometric distortion and image registration errors
- Acquisition-to-display time less than film X-ray imagers (less than 1-5minutes)
- Simultaneous and synchronous CCD acquisition to avoid varying individual exposure

Based on these expectations and the methodologies presented previously in this work, a prototype imager and dual DSP system was developed to simulate the mosaic imaging technique. Since a full mammographic imager (6000x4500 pixels) would be expensive to prototype, a smaller imager and simulations are a much more cost effective method for proof of operation.

The system design was created following the modular system method. The exposure time was set to 160ms and a strobed lighting scheme was employed for illumination. Most X-ray-to-light conversion techniques require the illumination to be in the red or infrared spectrum (600-800nm); thus a uniform light source at 650nm was used. Segmented images were acquired by shifting the image plane to simulate the mosaic technique. A total of 2x2 images totaling an area of 1536x1024 pixels were acquired and used to test the overall performance of the parallel hardware architecture. The multiple DSP circuitry used is a PCI bus based development board for a PC compatible computer.

Input/Output Capabilities

The maximum CCD acquisition time was recorded with a pixel clock of 2.5MHz and a CCD exposure time of 160ms. The input clock for the maximum COM port transfer through the DMA to memory was 12MHz. The bad pixel removal algorithm was written in C and not optimized in assembly for the C40. Finally, the total DMA sustainable bandwidth for the C40 was measured using 4 COM ports as inputs each operating and 8MHz each. The measured values are as follows:

Maximum acquisition time, t_{acq}	0.7s
Max sustainable C40 COM port speed using DMA transfer	12MB/s
Dead pixel removal time (DSP calculated), t_{bad}	0.9s
Total DMA sustainable bandwidth per C40	32MB/s

Table 3: I/O Capabilities and dead pixel removal execution time

Intensity Correction For Optical Non-uniform Illumination of CCD

As with most optical lens systems, the intensity of the focused image is not uniform due to less light acquired near the edges of the lens. This non-uniformity is considered a low frequency noise component and considerably alters the RMS noise value of the imager. A correction routine must be applied to remove this noise component from the system. The following calculations show the method devised for this system:

$$\overline{X_c} = \frac{1}{n \cdot m} \sum_{i=1}^{n} \sum_{j=1}^{m} X_c(i,j) \tag{10}$$

$$Y_c(i,j) = \frac{\overline{X_c}}{X_c(i,j)} \qquad \begin{cases} i = 1,2,\ldots,n \\ j = 1,2,\ldots,m \end{cases} \tag{11}$$

$$X'(i,j) = X(i,j) \cdot Y_c(i,j) \qquad \begin{cases} i = 1,2,\ldots,n \\ j = 1,2,\ldots,m \end{cases} \tag{12}$$

The image, X_c, used to find the correction coefficients is an average of 100 acquired images of the same uniform intensity field. Once the coefficients, Y_c, are calculated, they are stored in the system for future application. Each image that is individually acquired is corrected for non-uniform intensity with these coefficients. The total DSP computation time for the application of the correction coefficients on a single image was measured as:

$$t_{int} = 0.12s$$

Distortion Correction of Optical Aberrations

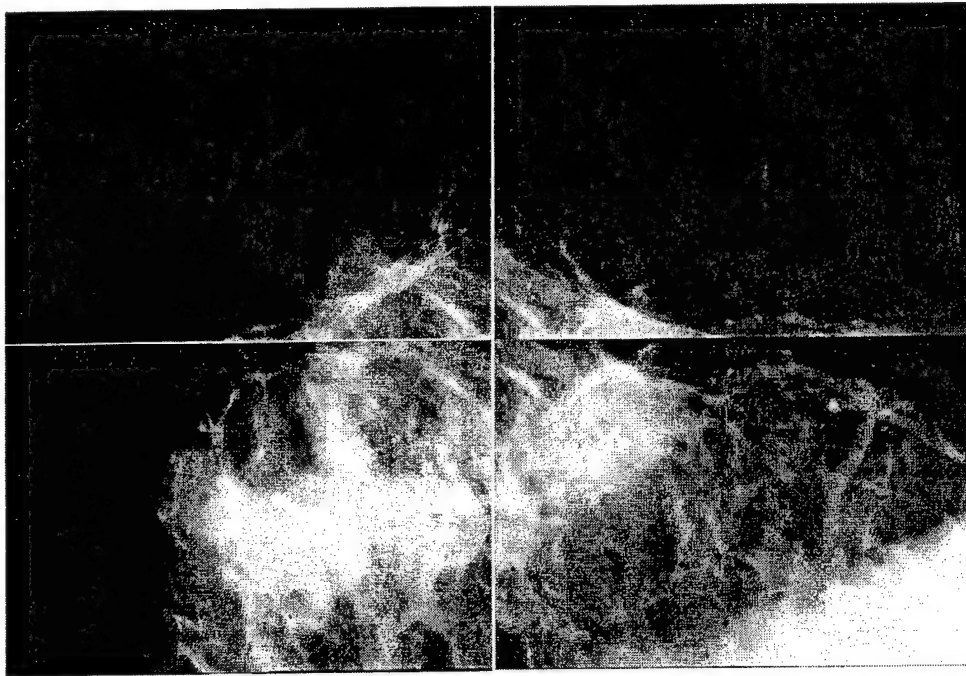Figure 9 below shows 4 breast images[2] taken with the imager each 768x512 pixels:

Figure 9: Four Images Acquired With Single CCD - Film Was Repositioned To Simulate Mosaic

---

[2] The original mammograms were taken using conventional film and these films were imaged with the CCD imager to simulate the acquisition of actual mammograms.

Note the overlapped areas, these are required to precisely register the final image. After applying the distortion correction routine, the following 4 corrected images were obtained. The total processing time required for this correction step on one image is:
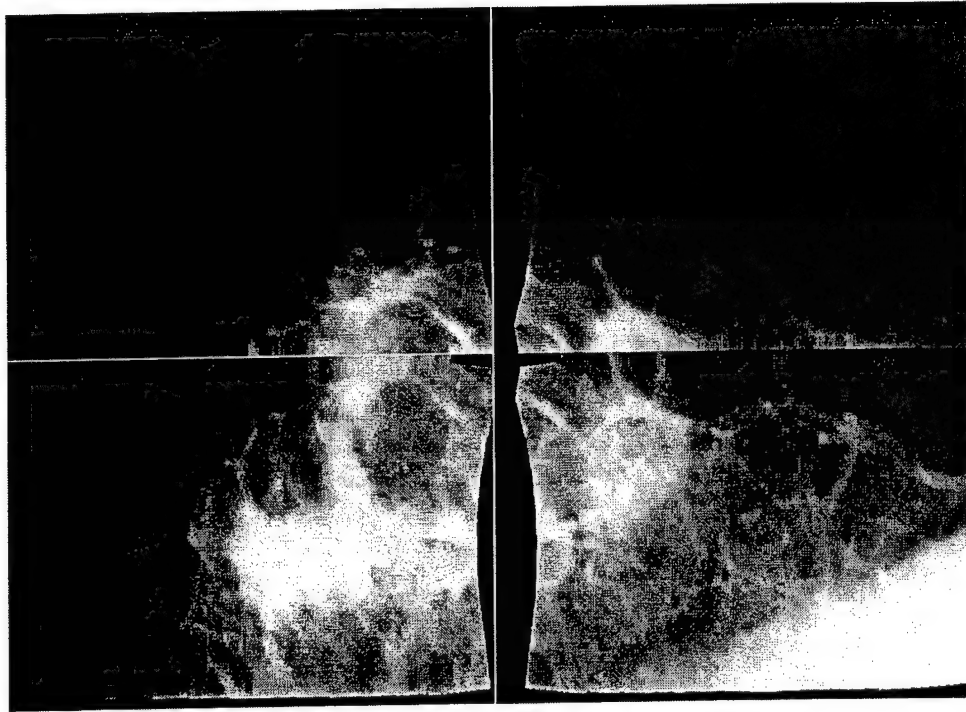
$$t_{dist} = 2s$$

Figure 10: Four images after lens distortion correction

Total Acquisition and Registration Time For 2x2 CCD Module

The following calculation presents the imager's acquisition-to-registration time. Note that the factors of 4 correspond to computations repeated on each of the 4 CCD images.

$$t_{mod} \approx t_{acq} + 4\left(t_{bad} + t_{int} + t_{dist}\right) \tag{13}$$
$$t_{mod} \approx 0.7 + 4(0.9 + 0.12 + 2)$$
$$t_{mod} \approx 12.8s$$

Where t_{mod} is the total image acquisition and registration time for 4 CCD images using one C40 DSP; the total image size after reconstruction is 1410x956 pixels. The fully registered image is shown below:
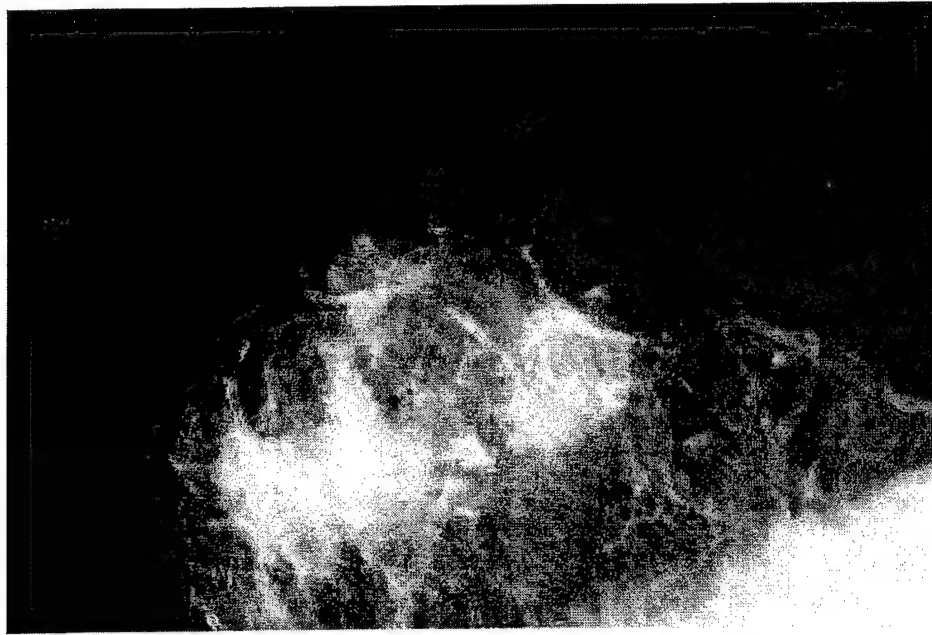
Figure 11: Fully reconstructed image from four segments, 1410x956 pixels

DSP Intercommunication Speed

The following table reports the data transfer speed between two C40 DSP's via one intercommunication port:

Data Transfer: 1 CCD Image	Elapsed Time For Data Transfer, t_{trans}	Average Bandwidth
800kB	0.1258 s	6.25MB/s

Table 3: DSP Intercommunication transfer speed

The communication speed reported above gives a measure of the bandwidth available for carrying out the final registration. The method used for stitching the overall image across multiple mosaic modules only requires the passing of image data to a final memory located on a host workstation. Below shows the image transfer scheme for the full size imager:
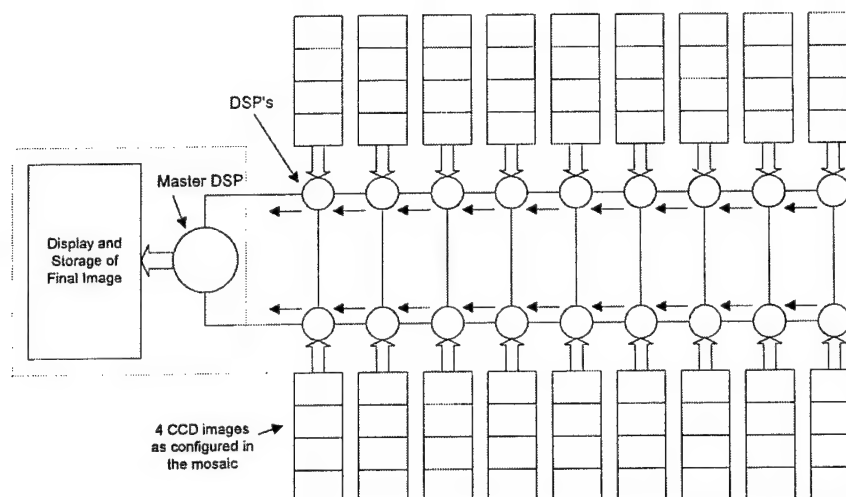
Figure 12: Final Image Readout To Master DSP on Host Workstation

A total of 9 transfer steps are required to collect all the image data to the workstation. The overall estimated time from acquisition-to-display for the mammography device is calculated as:

$$t_{tot} \approx 36t_{trans} + t_{mod}$$
$$t_{tot} \approx 36 \times 0.1258s + 12.8s \tag{14}$$
$$t_{tot} \approx 17.3s$$

5. CONCLUSIONS

A complete parallel hardware architecture for CCD-mosaic digital mammography was presented. The three layer method for designing the mosaic hardware allows various configurations of CCD's, analog processors, and digital processing elements to maximize efficiency for the development of digital mammography systems. The architecture presented also allows various image registration techniques to be implemented using high level programming languages. The particular registration method used shows very promising results in terms of accuracy and the speed in which each routine is executed on the hardware. The total time is approximately 17 seconds for full registration of the final mammogram and requires only one exposure. These results are very promising specifically for the following aspects:

- Close to real-time preliminary inspection of the mammograms by physicians
- Accelerated telemammography due to digital image availability
- Accelerated image archiving
- Parallel DSP processing availability to perform detection algorithms, loss-less compression, or other computationally intensive image processing tasks directly following acquisition

6. ACKNOWLEDGMENTS

7. REFERENCES

1. A. Jalink, J. McAdoo, G. Halama, and H. Liu, "CCD Mosiac Technique for Large-Field Digital Mammography", *IEEE Transactions on Medical Imaging*, vol. 15, no. 3, pp. 260-267, June 1996.
2. V. Swarnakar, M. Jeong, R. Wasserman, E. Andres, and D. Wobschall, "An Integrated Distortion Correction and Reconstruction Technique For Digital Mosaic Mammography", *SPIE Medical Imaging*, vol. 3031, pp. 673, 1997.
3. A.D.A. Maidment and M. J. Yaffe, "Analysis of Signal Propagation In Optically-Coupled Detectors For Digital Mammography: II. Lens and Fibre Optics", *Physics in Medicine and Biology*, vol. 41, pp. 475-493, 1996.
4. I. Naday, S. Ross, E. M. Westbrook, and G. Zentai, "Charge-coupled-device/fiberoptic Taper Array X-ray Detector for Protein Crystallography", *SPIE Solid State Sensor Arrays: Development and Applications*, vol. 3019, pp. 17-34, 1997.
5. G. C. Holst, "CCD Arrays, Cameras, and Displays", *JCD Publishing and SPIE Optical Engineering Press*, 1996.
6. Eastman Kodak Company Microelectronics Technology Division, "KAF-0400 768x512 Full-Frame CCD Image Sensor Performance Specification", *Kodak Image Sensors*, 1992.
7. Analog Devices Inc., "AD9101 - 125MSPS Sample/Hold Amplifier Data Sheet", *Analog Devices Inc.*, 1997.
8. Analog Devices Inc., "AD871 - 5MSPS 12bit A/D Converter Data Sheet", *Analog Devices Inc.*, 1996.
9. Texas Instruments Inc.,"TMS320C40, Parallel Digital Signal Processor Data Sheet", *Texas Instruments Inc.*, SPRS038, January 1996.
10. S. T. Smith, "Parallel Hardware Architecture For High Resolution CCD-Mosaic Digital Imaging", *MS Thesis: State University of New York at Buffalo*, 1998.

---

[3] Author contact information at Sensor Plus:
Scott Smith: E-Mail: ssmith@sensorplus.com   Web Info: www.sensorplus.com/image.html   Tel: 716-831-0091 Fax: 716-831-0212
Darold Wobschall: spadmin@sensorplus.com   Vice President of Technology

EVALUATION OF A DIGITAL MOSAIC MAMMOGRAPHIC IMAGER

VIVEK SWARNAKAR, SCOTT T. SMITH, MYOUNGKI JEONG,
HYUNKEUN KIM AND DAROLD WOBSCHALL
Sensor Plus Inc.
USA

1. Introduction

Mosaic architecture based digital mammography is attractive since it offers an affordable and scaleable solution towards obtaining high resolution digital mammograms. Limitations on the clinical usability of the architecture can be associated to the x-ray conversion screen utilized and to the methods employed to reconstruct the final digital mammogram. The x-ray conversion screen imposes limits on the efficiency of the optical conversion and the resolution of the finest resolvable detail. This can be addressed to an extent via use of specialized materials [1]. Reconstruction techniques on the other hand are likely to introduce artifacts in the final image. This can be addressed by employing complex reconstruction algorithms, which consequently may increase the time required to generate the final image.

The following section presents an overview of the mosaic architecture. The primary objective of this paper is to illustrate the applicability of the mosaic imaging architecture to generate digital mammograms. In section 3 a simulation study used to evaluate the effect of technique on the quality of the reconstructed image is described. Section 4 contains the results of the simulation study. Finally some discussions and future areas of work are identified in section 5.

2. Parallel architecture

The imaging hardware methodology developed for this device is based on a two-dimensional array of charge-coupled devices (CCD's) and lenses to acquire large format mammograms as shown in figure 1 below [2]. The analog and digital electronics required to process this parallel array of CCD's is based on a three layer approach shown in figure 2. By effectively separating the CCD's, the analog processors (AP's), and the digital processors (PE's), the parallel architecture may be optimized for performance, cost, and size.
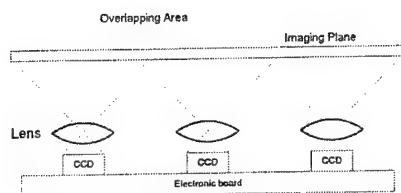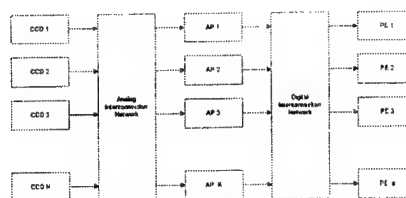
Figure 1 : CCD mosaic array

Figure 2 : Three layer modular mosaic electronics
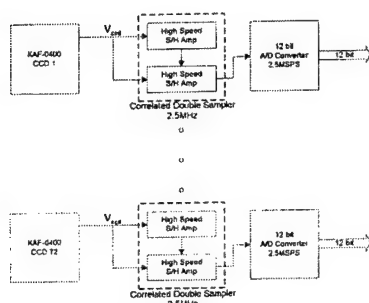

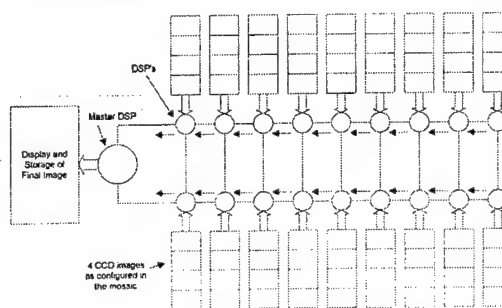**Figure 3 : Analog processor for each CCD channel**

Figure 4 : Parallel processing array and image readout sequence

The CCD chosen for this digital mammography device is the Kodak KAF-0400 768x512 pixel image sensor. A total of 72 CCD's are used in a 8x9 array for the full digital mammography device which forms a maximum image size of 6144x4608 pixels. The analog processing electronics consist of an array of correlated double samplers (CDS's) and 12 bit A/D converters. The CDS circuit effectively removes pixel reset noise from the CCD's analog signal and is of integral importance in the analog processing chain (figure 3). The overall pixel rate of the mosaic imager is 2.5MHz.

The digital processing array consists of 18 TMS320C40 DSP processors in a ladder configuration as shown in figure 4 above. Each DSP module acquires 4 CCD images and performs reconstruction to form a 4x1 segment image. The control points derived from a calibration procedure set the stitching points for each of the image segments. Thus, each image segment is directly read out through a master DSP to a main memory to form the final mammogram.

The total acquisition-to-display time was determined by measuring the total time required for the 4x1 mosaic module in combination with the overall readout time from the parallel DSP architecture. A single 4x1 segment module required **12.8 sec.** to acquire and process. The average transfer speed between DSP's is 6.25MB/s and a total of 36 transfer steps are required to collect all the image data to the workstation. Thus, the overall estimated time from acquisition-to-display for the mammography device is estimated to be approximately **18 sec.**

This complete parallel hardware architecture for CCD-mosaic digital mammography shows promising results in terms of the following:

- Close to real-time preliminary inspection of the mammograms by physicians

- Accelerated telemammography due to digital image availability
- Accelerated image archiving
- Parallel DSP processing availability to perform detection algorithms, loss-less compression, or other computationally intensive image processing tasks directly following acquisition

3. Quality of the reconstruction.

The quality of reconstructed images can be subjectively evaluated by expert observers. However, in order to numerically quantify the quality of the image, an expected ideal image is required. In this study, an original mammogram was segmented into several overlapping sub-images to simulate image acquisition by several CCDs. Subsequently a distortion function, similar to that introduced by the imager optics, is applied to each tile. The mosaic image is reconstructed by stitching all the sub-images together. Details of the reconstruction techniques used in this study can be found in earlier publications [3]. Note that if a given set of distorted sub-images are generated, the remaining stages in the reconstruction are just as they would be for any image acquired directly through the CCDs. The reconstructed and original mammograms may be compared using similarity measures. Computing similarity measures on entire mammograms can provide a global estimate of the image reconstruction quality. However, in mammography local features such as microcalcifications or masses are of major relevance. Therefore in this simulation study the emphasis is given on the fidelity with which such features can be reconstructed. By doing so, the types of artifacts introduced by the reconstruction techniques can also be better observed.

4. Experimental results

A set of mammograms were selected from the publicly available MIAS database [4]. Each image was of size 1024 x 1024 pixels, sampled at 200 micrometer pixel size resolution. Consultation with expert radiologists prompted the selection of images with the types of features within a circular area of radius (in pixels) as follows:

- Circumscribed Mass - 29 pixels
- Spiculated Mass   - 53 pixels
- Microcalcification   - 8 pixels

The most severe distortions or artifacts can be expected in the region where four (4) neighboring CCDs observe the same overlapping area. In order to study the artifacts introduced in this region the features of interest in the original mammogram were located within the overlap region of four sub-images. The original mammogram was cropped into four sub-images and a distortion function was applied to each of the cropped regions. These four images were then supplied to the mosaic imager. Distortion correction schemes using Piece-wise linear approximation (PL), Bilinear interpolation (BI) and

Spline interpolation (SP) were applied to correct each cropped image. Sections from the corrected sub-images that do not belong to the overlap area of the four CCDs were extracted and placed together to form the reconstructed image.

Mean squared error, mean absolute error and cross correlation were the similarity measures employed in this work[5]. In Table I the results of comparing the original image and the reconstructed image are shown. It should be noted that overall the Spline based reconstruction provided the better result.

	MAE			MSE			CC		
Feature	PL	BI	SP	PL	BI	SP	PL	BI	SP
Circum. Mass	1.48	1.08	1.16	4.70	2.58	2.97	0.99	0.99	0.99
Spic. Mass	1.44	1.09	1.55	3.96	2.37	2.66	0.99	0.99	0.99
Microcal.	1.36	1.19	1.97	3.79	2.99	8.85	0.99	0.99	0.98

Table I. Quantitative results computed on regions with features of interest.

Visual assessment of the images was carried out by presenting the reconstructed images to expert radiologists. There were no significant differences observed by the radiologists. However, when observing the features in the unsharp mask enhanced images, the piece-wise linear reconstruction technique provided the most accurate visual results. The images in Figure 4.1 below show two of the features investigated as they appear in the unsharp mask enhanced images [6].
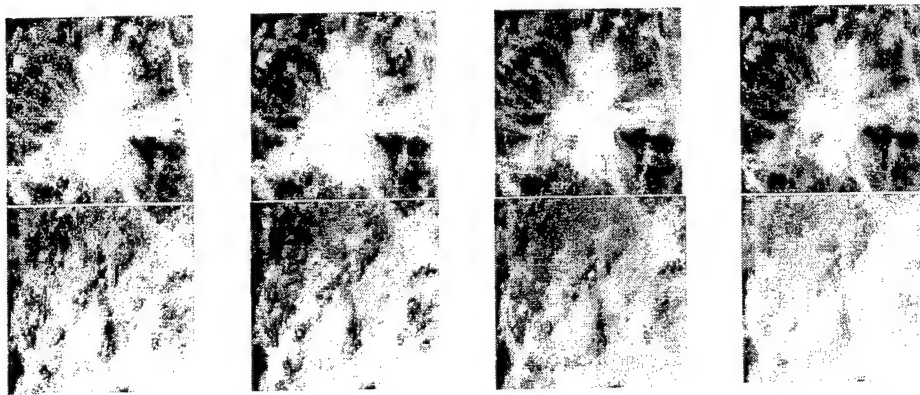

Figure 5: Images of the areas with features of interest. Left-right: Original, piece-wise linear, bilinear, spline. Top row: spiculated mass. Bottom Row: Microcalcification.

5. Discussion

The architecture presented in this work is a generalized solution towards mosaic imaging and promising results in terms of affordability and scalability. During evaluation it was

observed that spline based reconstruction was the most complex and time consuming technique. Nevertheless, even for this technique full reconstruction was achieved in under 1 minute. The scaleable nature of the architecture guarantees that even if several CCDs are used in the mosaic imager, the reconstruction time will not be significantly affected. Visual assessment and numerical quantification resulted in significantly distinct findings. Numerical quantification provides a statistical mechanism to choose the better technique. Meanwhile the visual assessment is a subjective task and can vary from case to case. A good compromise between the two extremes can be obtained by using the bilinear reconstruction approach. Clinical usability of this approach will be dependent on the X-ray conversion screen employed. Further work needs to be done to investigate the effect of the X-ray conversion screen. Additional work is also needed to improve the stitching and reconstruction techniques.

6. References

1. J. A. Rowlands, D. M. Hunter and N. Araj, "X-Ray Imaging Using Amorphous Selenium: A photoinduced discharge readout method for digital mammography", Med. Phys., Vol. 18, pp. 421-431, 1991.
2. Scott T. Smith, Hyunkeun Kim, Vivek Swarnakar, Myoungki Jeong and Darold C. Wobschall, "Parallel hardware architecture for CCD-mosaic digital mammography", SPIE Medical Imaging – 98.
3. V. Swarnakar, M. Jeong, S. Smith, H. Kim and D. Wobshall, "An Integrated Distortion Correction Reconstruction Technique For Digital Mosaic Mammography", SPIE Medical Imaging, vol. 3031, pp. 673, 1997.
4. MIAS Database: http://skye.icr.ac.uk/miasdb/miasdb.html
5. R. Salvi, "Introduction to Applied Statistical Signal Analysis", IRWIN 1991.
6. A. K. Jain, "Fundamentals of Digital Image Processing", Prentice Hall 1989.

Evaluation of A Digital Mosaic Mammographic Imager

Vivek Swarnakar, Scott T. Smith, Myoungki Jeong, Hyunkeun Kim, Darold Wobschall

Objectives

- Apply the reconstruction technique to different types of mammographic image data.
- Numerically and visually evaluate quality of images generated using each reconstruction technique.
- Evaluate the effect each technique has on the quality of individually reconstructed features of interest.
- Determine parameters that most influence each technique
- Demonstrate an efficient parallel hardware architecture to accomplish all imaging and processing needs

Distortion Correction

- A custom designed calibration-screen with fiducial markers is employed to achieve high accuracy of distortion correction.
- Inter-fiducial distance relation is known a priori.
- Three types of correction schemes are investigated:
  - *Piece-wise linear (local operator)*
  - *Bilinear interpolation (global operator)*
  - *Spline interpolation (global operator)*
- The images shown below were corrected using spline interpolation after acquisition from the single CCD prototype imager

Reconstruction Simulation Results

- The images used are sections of actual mammograms
- The distortion introduced is modeled numerically using a "barrel distortion" approximation
- Mammograms with three types of anomalies were analyzed

  - *Circumscribed Mass (G): radius 29 pixels.*
  - *Spiculated Mass (F): radius 53 pixels.*
  - *Calcification-A (D): radius 25 pixels.*
  - *Calcification-B (D): radius 8 pixels.*

Visual Evaluation (edge enhancement)

Circumscribed Mass

Digital Mosaic Imaging

- Mosaic imaging requires correction of the distortion introduced by each individual optical component and stitching of the individual sub-images to obtain a digital mosaic mammogram reconstruction.
- Digital mosaic imaging provides a scaleable, high resolution/cost means for mammography.
- The correction scheme plays a pivotal role in the quality of the final reconstructed mammogram.
- High accuracy in the distortion correction step allows the use of a simplified stitching scheme.

Digitized Calibration Pattern

Quantitative Analysis(MAE)

Image Mean Absolute Error

	Piece-Linear	Bilinear	Spline
Circ. Mass.	1.19	0.78	1.09
Spic. Mass.	0.72	0.49	0.7
Micro. Calc.	0.67	0.43	0.55

Feature Mean Absolute Error

	Piece-Linear	Bilinear	Spline
Circ. Mass.	1.48	1.06	1.16
Spic. Mass.	1.44	1.09	1.15
Micro. Calc.-A.	1.33	1.05	1.11
Micro. Calc.-B.	1.36	1.19	1.97

Visual Evaluation (edge enhancement)

Spiculated Mass

Lens Based CCD Mosaic Array

Reconstructed Calibration Pattern

Quantitative Analysis (MSE)

Image Mean Squared Error

	Piece-Linear	Bilinear	Spline
Circ. Mass.	31.72	27.76	27.15
Spic. Mass.	35.09	26.88	29.31
Micro. Calc.	26.26	19.22	15.01

Feature Mean Squared Error

	Piece-Linear	Bilinear	Spline
Circ. Mass.	4.7	2.58	2.98
Spic. Mass.	3.96	2.37	2.66
Micro. Calc.-A.	3.55	2.26	2.53
Micro. Calc.-B.	3.78	2.99	8.85

Visual Evaluation (edge enhancement)

Micro Calcification - A

Advantages of A Parallel Architecture For CCD Mosaic Digital Mammography

- Close to real-time preliminary inspection of the mammograms by physicians
- Accelerated telemammography due to digital image availability
- Accelerated image archiving
- Parallel DSP processing availability to perform detection algorithms, loss-less compression, or other computationally intensive image processing tasks directly following acquisition

Analog Processing For 8x9 CCD Imager

Visual Evaluation

Circumscribed Mass

Conclusions

- Quantitative Analysis/Visual Analysis
  - Image restoration from a global perspective is best using the Cubic Spline approach.
  - The Bilinear interpolation provides best results in quantitative analysis.
  - When individual features and image processing algorithms(such as unsharp filtering and edge enhancement) are considered in visual analysis, the Piece-wise linear approach provides better results.

- Global correction approaches(Bilinear/Spline) are less sensitive to errors in the detected fiducial markers.

Three Layer Hardware Approach For Efficient Mosaic Imaging

- CCD's - Image Sensor Layer
- AP's - Analog Processing Layer
- PE's - Digital Processing Element Layer

Parallel Array of Processing Elements

Visual Evaluation

Spiculated Mass

- When considering detailed features such as microcalcifications, a localized correction approach should be employed.

- CCD Mosaic Hardware Architecture
  - The three layer modular hardware approach allowed evaluation of overall performance of an 8x9 CCD imager by only constructing a single CCD imager.
  - The estimated acquisition-to-display time demonstrates the speed at which mammograms would be available for inspection and processing, ~ 18 seconds.
  - The single CCD imager also provided the platform to sufficiently test the reconstruction software capabilities with 4 actual calibration pattern images

Single CCD Prototype Imager

- This single channel prototype was used to measure the feasibility of the larger CCD mosaic required for the complete mammography imager.
- A test pattern was repositioned in the X-Y plane to simulate a 2x2 mosaic.

Estimation of Acquisition and Registration Time Required For A 8x9 CCD Mosaic

$$t_{mod} \approx t_{acq} + 4\left(t_{bnd} + t_{rst} + t_{dist}\right)$$

$$t_{mod} \approx 12.8s$$

$$t_{tot} \approx 36t_{trans} + t_{mod}$$

$$t_{tot} \approx 17.5s$$

Visual Evaluation

Micro-Calcification - A

Acknowledgments

Appendix B Circuit Diagrams

COMPANY:				
TITLE:				
W126 DSP Camera				
CODE:	SIZE:	DRAWING NO:		REV:
	B	W126KDSP1.sch		1
SCALE:			SHEET: 7 OF 7	

A/D Converter and Support

PROGRAM NOTE:

A/D_CLK has to be inverted

CMOS Analog References

W126 DSP Camera

DRAWN: A. Palczewski	DATED: 7-01-99	
CHECKED: S. Smith	DATED: xx-xx-99	
QUALITY CONTROL:	DATED:	
RELEASED:	DATED:	

COMPANY:				REV:
TITLE:				1
	CODE:	SIZE: B	DRAWING NO: W126KDSP1.sch	
	SCALE:			SHEET: 3 of 7

REVISION RECORD

LTR	ECO NO:	APPROVED:	DATE:

W126 DSP Camera

Analog Power Supply

C24 0.1uF
C35 33uF 10V
MICREL-MIC2920A U5
OUT 3
IN 1
GND 2
C34 33uF 10V
FB2 2 +7VA 1

Digital Power Supply

C25 0.1uF
C37 33uF 10V
MICREL-MIC2920A U6
OUT 3
IN 1
GND 2
C36 33uF 10V
FB3 2 +7VD 1

C38 33uF 10V

+5VA
+5V

FB1 1 2

X_STRB
R_TEMP
+7V

J1-1
J1-2
J1-3
J1-4

COMPANY:

TITLE: W126 DSP Camera

DRAWN: A. Palczewski	DATED: 7-01-99	CODE:
CHECKED: S. Smith	DATED: xx-xx-99	SIZE: B
QUALITY CONTROL:	DATED:	DRAWING NO: W126KDSP1.sch
RELEASED:	DATED:	REV: 1
		SCALE:

SHEET: 5 OF 7

Data Latch

PORT_DATA[00:07]

PORT_DATA00
PORT_DATA01
PORT_DATA02
PORT_DATA03
PORT_DATA04
PORT_DATA05
PORT_DATA06
PORT_DATA07

R16A 100
R16B 100
R16C 100
R16D 100
R16E 100
R16F 100
R16G 100
R16H 100

B_DATA[00:07]

B_DATA00
B_DATA01
B_DATA02
B_DATA03
B_DATA04
B_DATA05
B_DATA06
B_DATA07

C30 0.1uF
+5V

+5V
R18 10.0K

+5V
R17 10.0K

B_DATA[00:07]
B_DATA00
B_DATA01
B_DATA02
B_DATA03
B_DATA04
B_DATA05
B_DATA06
B_DATA07

U8A
74ACTQ16374
OE1
CLK1
D0
D1
D2
D3
D4
D5
D6
D7
Q0
Q1
Q2
Q3
Q4
Q5
Q6
Q7

U8B
74ACTQ16374
OE2
CLK2
D0
D1
D2
D3
D4
D5
D6
D7
Q0
Q1
Q2
Q3
Q4
Q5
Q6
Q7

B_DATA[00:07]
B_DATA00
B_DATA01
B_DATA02
B_DATA03
B_DATA04
B_DATA05
B_DATA06
B_DATA07

PCK_OE1
OE1
CP

DATA[00:11]
DATA00
DATA01
DATA02
DATA03
DATA04
DATA05
DATA06

PCK_OE2
OE2
CP

DATA[00:11]
DATA07
DATA08
DATA09
DATA10
DATA11

OVR

+5V

Transceiver / Arbiter

U1
TS041LV03

AVDD1 34
AVDD2 35
AVDD3 37
AVDD4 40
AVDD5 42
AVDD6 43

CTL0 5
CTL1 4

D0 7
D1 9
D2 10
D3 11
D4 13
D5 14
D6 15

SYSCLK 2
CLKON 22

R0 66
R1 67

CNA 17

TPBIAS0 46
TPBIAS1 53
TPBIAS2 59

TPA0+ 45
TPA0- 44
TPB0+ 43
TPB0- 42
TPA1+ 52
TPA1- 51
TPB1+ 50
TPB1- 49
TPA2+ 58
TPA2- 57
TPB2+ 56
TPB2- 55

DVDD1 6
DVDD2 16
DVDD3 30
DVDD4 38
DVDD5 68
DVDD6 73

VDD-5V 9

CPS

PLLVDD

CPS 27
ISO 28
LPS
LREQ

XI 77
XO 76

FILTER0 71
FILTER1 72

PD 18
RESET 28

PC0 23
PC1 24
PC2 25

TESTM 31
SE 32
SM 33

PLLGND1 74
PLLGND2 75

DGND1
DGND2
DGND4
DGND5
DGND7

AGND1 36
AGND2 37
AGND3 48
AGND5 60
AGND7 61
AGND8 64
AGND10 65

+3.3V

DATA[00:07]
DATAO0
DATAO1
DATAO2
DATAO3
DATAO4
DATAO5
DATAO6
DATAO7

SCLK[3]

R[0:1]

CNA

TPBIAS0[2]
TPBIAS1[2]
TPBIAS2[2]

TPA0+[2]
TPA0-[2]
TPB0+[2]
TPB0-[2]
TPA1+[2]
TPA1-[2]
TPB1+[2]
TPB1-[2]
TPA2+[2]
TPA2-[2]
TPB2+[2]
TPB2-[2]

CLKON_CTRL

J1-1
J1-2
J1-3

R2 5.34K
R1 1M
R20 10K

CPS 27
400K R19
ISO 28
[3]LPS
[3]LREQ

X1 77
XO 76
Fn 71
F1 72
C9 0.1uF
Pn 18

[3,4]RESET
R22 1.8K

PC0 23
PC1 24
PC2 25
TESTM 31
R31 1.8K
SE 32
SM 33

R30 1.8K
R29 1.8K

R21 4.7K
+3.3V
0.1uF +12V

Y1 24.576 MHz
12pF
12pF
C27
C28

R26 10K
R27 10K
R28 10K
R23 1.8K
R24 1.8K
R25 1.8K

D1 Red LED
R32 200
2 CNA_DR

C31 1.0uF
C30 1.0uF
C29 1.0uF

C28 0.01uF
C18 0.01uF
C8 0.1uF
C17 0.01uF
C21 0.01uF
C4 0.1uF
C20 0.01uF
C16 0.01uF
C5 0.1uF
C15 0.01uF
C19 0.01uF

C1 0.1uF
C2 0.1uF
C22 0.01uF
C12 0.01uF
C23 0.01uF
C13 0.01uF
C7 0.1uF
C14 0.01uF
C24 0.01uF
C3 0.1uF
C8 0.1uF
C25 0.01uF
C11 0.1uF

IEEE-1394 Connectors

Title block:

DRAWN: K. Swindell	DATED: 11-16-98
CHECKED: H. Kim	DATED: 11-17-98
QUALITY CONTROL:	DATED:
RELEASED:	DATED:

COMPANY:
TITLE: **W126 Fire Wire**
CODE: SIZE: **B** DRAWING NO: **w126fire2.sch** REV: **2**
SCALE: SHEET: 2 OF 4

Connector pins: J7-1…J7-8, J6-1…J6-8, J9-1…J9-8 (CHGND)

Fuses: F1 1A, F2 1A, F3 1A — +12V, CHGND

Connector pairs: J10-1/J10-2, J11-1/J11-2, J14-1/J14-2, J15-1/J15-2, J17-1/J17-2, J19-1/J19-2
J5-1/J5-2, J8-1/J8-2, J12-1/J12-2, J13-1/J13-2, J16-1/J16-2, J18-1/J18-2

Components:
R3 1M, C33 0.001uF, C35 0.01uF, C34 0.01uF, C32 0.001uF
R16 54.9, R18 54.9, R6 5.11K, R15 54.9, R17 54.9, C38 270pF
R12 54.9, R14 54.9, R5 5.11K, R11 54.9, R13 54.9, C37 270pF
R8 54.9, R10 54.9, R4 5.11K, R7 54.9, R9 54.9, C36 270pF, C38 270pF

Signal labels:
(1)TPBIAS0, (1)TPA0+, (1)TPA0-, (1)TPB0+, (1)TPB0-
(1)TPBIAS1, (1)TPA1+, (1)TPA1-, (1)TPB1+, (1)TPB1-
(1)TPBIAS2, (1)TPA2+, (1)TPA2-, (1)TPB2+, (1)TPB2-

Link-Layer Controller

+3.3V Transceiver Power Supply

+12V Cable Power Supply

50 Pin Connector to DSP Board

COMPANY:	
TITLE:	W126 Fire Wire
CODE:	SIZE: B	DRAWING NO: w126fire2.sch	REV: 2
SCALE:	SHEET: 4 OF 4

DRAWN: K. Swindell	DATED: 11-16-98
CHECKED: H. Kim	DATED: 11-17-98
QUALITY CONTROL:	DATED:
RELEASED:	DATED:

UNUSED

TO FIREWIRE

CAS RAS W SEL

JROMEN

SENSOR PLUS

GLOBAL MEMORY CONTROL & DSP

COMPANY:		
TITLE:		
	GLOBAL MEMORY CONTROL & DSP	
CODE:	SIZE: C	DRAWING NO: W126DIG6.SCH	REV: 3.0
SCALE:		SHEET: 4 OF 4

		DATED:	
DRAWN:	AJP	1/8/99	
CHECKED:	HK	11/06/98	
QUALITY CONTROL:	BC	1/7/98	
RELEASED:			

TO TEC
0-1.5A

TE1+ J1-1 | TE1+

TE1- J1-2 | TE1-

R_TEMP

+7V

GND